

NATIONAL & INTERNATIONAL SCIENTIFIC EVENTS

International Design Engineering Technical Conferences & Computers & Information in Engineering Conference (IDETC/CIE 2018)

Venue: Hilton Québec
Location: Québec, Canada

Begins: August 26, 2018
Ends: August 29, 2018

7th EuCheMS Chemistry Congress, Molecular frontiers and global challenges

Venue: ACC Liverpool
Location: Liverpool, UK

Begins: August 26, 2018
Ends: August 30, 2018

XXV EFMC International Symposium on Medicinal Chemistry (EFMC-ISMC 2018)

Venue: Ljubljana Exhibition and Conv. Centre
Location: Ljubljana, Slovenia

Begins: September 2, 2018
Ends: September 6, 2018

2018 International Conference on Solid State Devices and Materials (SSDM2018)

Venue: Hongo Campus, The University of Tokyo
Location: Tokyo, Japan

Begins: September 9, 2018
Ends: September 13, 2018

5th Nuclear Materials Conference (NuMat 2018)

Venue: Motif Seattle
Location: Seattle, WA, USA

Begins: Oct 14, 2018
Ends: Oct 18, 2018

13th International Conference of Food Physicists

Venue: Porto Bello Hotel Resort & Spa
Location: Antalya, Turkey

Begins: Oct 23, 2018
Ends: Oct 25, 2018

19th International Metallurgy and Materials Congress

Venue: TUYAP Fair, Conv. and Congress Center
Location: İstanbul, Turkey

Begins: Oct 25, 2018
Ends: Oct 27, 2018

32nd EFFoST International Conference

Venue: La Cité Nantes Events Center
Location: Nantes, France

Begins: Nov 6, 2018
Ends: Nov 8, 2018

14th International Conference on Molecular Epidemiology and Evolutionary Genetics of Infectious Diseases

Venue: Hotel Melia
Location: Sitges, Spain

Begins: Nov 6, 2018
Ends: Nov 9, 2018

International Conference on Hydraulics and Pneumatics
HERVEX – 24th edition

Venue: Hotel Palace, Baile Govora
Location: Valcea County, Romania

Begins: Nov 7, 2018
Ends: Nov 9, 2018

The 23rd Asian Technology Conference in Mathematics

Venue: Yogyakarta State University (YSU)
Location: Yogyakarta State University, Indonesia

Begins: Nov 20, 2018
Ends: Nov 24, 2018

International Conference on Drug Discovery and Translational Medicine 2018 (ICDDTM '18)

Venue: THE EVERLY HOTEL
Location: Putrajaya, Malaysia

Begins: Dec 3, 2018
Ends: Dec 5, 2018



Abstracted & Indexed in:

TR Dizin Mühendislik ve Temel Bilimler Veri Tabanı | CrossRef | Google Scholar | MIP Database | StuartxChange | ResearchBib | Scientific Indexing Services (SIS)

HITTIT

JOURNAL OF SCIENCE & ENGINEERING HITTITE

HJSE Official Journal of Hitit University Volume 5, Issue 2, 2018 www.hjse.hitit.edu.tr

HJSE Official Journal of Hitit University Volume 5, Issue 2, 2018 www.hjse.hitit.edu.tr

HJSE Official Journal of Hitit University Volume 5, Issue 2, 2018 www.hjse.hitit.edu.tr

Volume 5, Issue 2, 2018

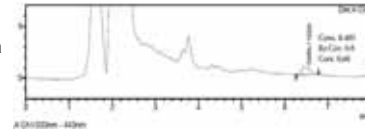
www.hjse.hitit.edu.tr

The Presence of Cronobacter Sakazakii, Enterobacteriaceae spp. and Ochratoxin-A in Infant Rice-Based Formula and Milled Rice Products

85-90

Sibel Özçakmak and Asya Çetinkaya

In this study, samples of three different commercial Infant Rice-based formulae with four samples (IRF), nine milled rice (MR) samples were searched for Cronobacter sakazakii, Enterobacteriaceae spp. and Ochratoxin-A (OTA).

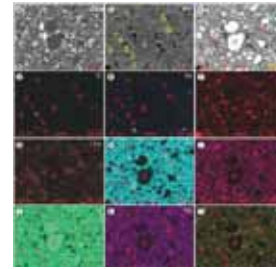


Mineralogical and Geochemical Characterization of Ancient Ceramic Sherds from Dipsizin Cave (Karaman, Turkey)

91-95

Mehmet Yavuz Hüseyinca and Osman Doğanay

Raw materials of two ancient ceramic sherds (ceramic-1 and ceramic-2) from Dipsizin cave were analysed by SEM-EDS in order to characterize ceramic fabrics.

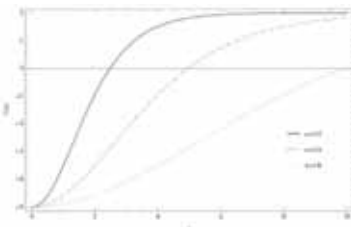


N-Dimensional Solutions of Klein-Gordon Particles for Scaled Molecular Potential via Higly Accurate Approximation

97-103

Hasan Fatih Kisoglu

The solutions of Klein-Gordon equation for equal vector and scalar symmetrical well potential is obtained in N-dimensional euclidean space.



A New Perspective On Soft Topology

105-113

Mustafa Burç Kandemir

In this article, it has been approached the concept of soft topological space with a new perspective. The soft topological space that is defined on a topological space as a parametrization of some subspaces of the space in Molodtsov's sense is defined.

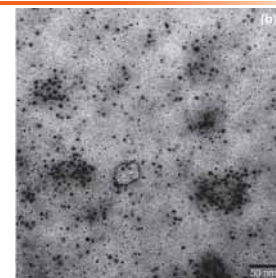
Consider the usual topological space of real numbers $(\mathbb{R}, \mathcal{U})$. Define the soft set (F, A) over \mathbb{R} such that $F: A \rightarrow \mathcal{P}(\mathbb{R}), F(p) = [p-1, p+1]$ where $p \in A = \{1, 2, 3, 4\} \subseteq \mathbb{N}$ and $\mathcal{F}_{(F, A)} = \{[p-1, p+1] \cap O \mid p \in A, O \in \mathcal{U}\}$

Enhanced Enzyme Activity with Ferritin Nanocages

115-118

Eylem Turan

In this study, a novel enzyme system based on ferritin nanocages was designed. α -Amylase was covalently crosslinked on surface of ferritin nanocages by EDC/NHS.



Explicit Solutions of a Three-dimensional System of Nonlinear Difference Equations

119-123

Bahriye Yilmazyildirim and Durhasan Turgut Tollu

In this paper, we show that the system of difference equations $x_{n+1} = \frac{x_n + y_n}{1 + x_n y_n}, y_{n+1} = \frac{y_n + z_n}{1 + y_n z_n}, z_{n+1} = \frac{z_n + x_n}{1 + z_n x_n}, n \in \mathbb{N}_0$, where the initial values x, y, z are real numbers, are solvable in explicit form via some changes of variables and tricks.

$$\lim_{n \rightarrow \infty} (|x_n|, |y_n|, |z_n|) = (1, 1, 1).$$

Impact of the cascade hydropower construction (HPC) on water quality of the Seyhan River, Turkey 125-135

Mehmet Ozcelik

This study summarizes the effect of cas-cade HPC on water quality in the Seyhan River basin during the 1995–2014 periods. Seyhan River basin has twenty two HPCs.



Preparation of Silicon-Antimony based Anode Materials for Lithium-Ion Batteries 137-140

Asuman Celik Kucuk, Samet Ozturk, Baris Cem Alpay and Mine Yorulmaz

In this study, SixSb immiscible blend anode materials have been synthesized using micron-sized silicone and antimony particles in different compositions through chemical reduction-mechanical alloying method (CR-MA)

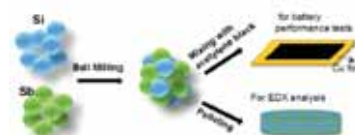


Figure 1. The concept and formation process of micron-sized Si/Sb blend systems

Design and Implementation of an Underwater Telemetric Glucose Monitoring System for Scuba Divers 141-146

S.Murat Egi, Corentin Altepe, Massimo Pieri, D. Ruzgar Sinoplu, Danilo Cia-loni, Tamer Özyiğit, Paola Pierleoni and Alessandro Marroni

This study communicates the details of a study to design, manufacture and test a prototype system that measures the blood glucose while diving and transmit the results in real time to the surface.



Geotechnical Characterization of a Pipe Stock Site for Its Suitability in Terms of Bearing Capacity and Liquefaction Considering the Economic Aspects 147-154

Mustafa Can Canoglu

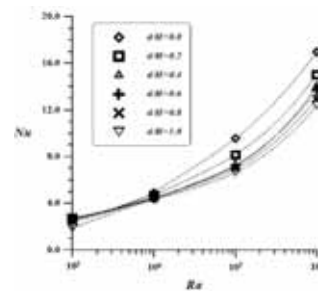
In this study, the suitability of an inert area to utilize a pipe stock site under a natural gas pipeline project was investigated, while considering the economic yield.



Thermal Behaviour of Residential Buildings with Cantilever Beams under Winter Boundary Conditions 155-164

Lütfü Namli

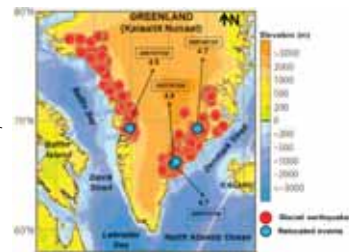
The thermal behaviour of residential buildings with cantilever beam under winter boundary conditions was numerically investigated by means of the open-ended structure approach in this study..



The Array Analyzing of The High Quality Glacial Seismic Events Active in Greenland Using Long-Period Surface (Rayleigh) Wave Detection by the German Regional Seismic Network 165-183

Mustafa Toker

In this study, the array processing technique was used with array parameters computed from the SHM to detect and analyze the slow glacial events using the array installation data from GRSN.



Journal Name : HITTITE JOURNAL OF SCIENCE AND ENGINEERING
Year : 2018
Managing Editor : Prof. Dr. Ali KILIÇARSLAN
Managing Office : Hitit University Faculty of Engineering
Managing Office Tel : +90 364 227 45 33 / 12 36
Publication Language : English
Publication Type : Peer Reviewed, Open Access, International Journal
Delivery Format : 4 times a year (quarterly)
Print ISSN : 2149-2123
Publisher : Hitit University
Publisher Address : Hitit Üniversitesi Kuzey Kampüsü Çevre Yolu Bulvarı
19030 Çorum / TÜRKİYE
Publisher Tel : +90 364 225 66 64



This new issue of Hittite Journal of Science and Engineering contains twelve manuscripts from the disciplines of chemistry, mathematics, chemical engineering, geological engineering, electrical and electronics engineering, food science and engineering, materials science and engineering, mechanical engineering. These manuscripts were first screened by Section Editors using plagiarism prevention software and then reviewed and corrected according to the reviewer's comments. I would like to express my gratitude to all our authors and contributing reviewers of this issue.

I would like to thank to the President of Hitit University, Dr. Reha Metin Alkan, for his constant interest in HJSE and also to the Associate Editors of HJSE, namely Dr. Dursun Ali Kose and Dr. Oncu Akyildiz, as well as our Production Team Dr. Kazim Kose, Dr. Hülya Çakmak, Mustafa Resit Haboglu, Erhan Çetin, Harun Emre Kıran, Ömer Faruk Tozlu for their invaluable efforts in making of the journal.

It's my pleasure to invite the researchers and scientists from all branches of science and engineering to join us by sending their best papers for publication in Hittite Journal of Science and Engineering.

Dr. Ali Kiliçarslan

Editor-in-Chief

The presence of *Cronobacter sakazakii*, Enterobacteriaceae spp. and Ochratoxin-A in Infant Rice-based formula and milled rice products

Sibel Özçakmak¹ and Asya Çetinkaya²

¹Provincial Directorate of Agriculture and Livestock, Samsun, Türkiye

²Kafkas University, Department of Food Engineering, Kars, Turkey

ABSTRACT

Rice based products could be have microbiological and toxicological hazards causing for unsuitable production and storage conditions. In this study, samples of three different commercial Infant Rice-based formulae with four samples (IRF), nine milled rice (MR) samples were searched for *Cronobacter sakazakii*, Enterobacteriaceae spp. and Ochratoxin-A (OTA). The presence of *C. sakazakii* and Enterobacteriaceae spp. was detected using ISO/TS 22964/IDF/RM 210 and and ISO 21528-2: 2004 method, respectively. A developed method using OCHRAPREP® (REFN: A9-P14.V4) in conjunction with HPLC described by AOAC 2000.003 was used with slight modifications of the purification and HPLC conditions and with another confirmation method for OTA. The limit of quantities measurement was 1.286 µg/kg. *C. sakazakii* was not found in any samples. Enterobacteriaceae spp. was determined above the legal limits (between 2.6x10² and 2.8x10⁴ kob/g, average 3.46x10⁴) in four samples (30.77%). OTA was detected by one IRF with milk product sample with 0.60 µg/kg (7.69%).

Keywords:

Infant Rice-based Formula, Milled rice, *C. sakazakii*, Enterobacteriaceae spp., Ochratoxin-A.

Article History:

Received: 2017/07/30

Accepted: 2017/10/18

Online: 2018/01/31

Correspondence to: Sibel Özçakmak,
Provincial Directorate of Agriculture and
Livestock, Samsun, Türkiye

Tel: +90 (362) 231-3700

Fax: +90 (362) 231-3700

E-Mail: damla-damla49@hotmail.com

INTRODUCTION

The significance and potential health risk of any contaminants in baby foods has been reported in the literature [1, 2]. A number of foodborne outbreaks associated with cereals based infant formula have been increased. Some mycotoxins [such as deoxynivalenol, zearalenone, ochratoxin A [OTA] and *Cronobacter sakazakii* have been reported to be prevalent at very low concentrations in infant cereal foods [3, 4, 5, 6, 7]. OTA has been reported to be prevalent at very low concentrations in infant cereal foods [8].

Mycotoxins are naturally occurring chemicals produced by moulds growing on foodstuffs, including rice. Among these rice mycotoxins, OTA is classified by the International Agency for Research on Cancer as a possible human carcinogen (Category 2B). OTA has been shown to have nephrotoxic, immunotoxic, genotoxic and teratogenic properties [9]. OTA was present semolina based baby foods, multicereal formulas, rice formulas [10]. If milled rice used for the production of infant formulas is subject to OTA contamination cau-

se of fungi contamination, the same is to be expected for the infant formula [11]. In particular, there is scarce information on the presence of OTA in rice based baby foods and/or ground rice products.

Enterobacter sakazakii is a member of the family Enterobacteriaceae, genus *Enterobacter*, and is a motile peritrichous, gram-negative bacillus [12]. *Cronobacter sakazakii*, formerly *E. sakazakii* [13] has been isolated commonly in contaminated powdered infant formula [6]. *C. sakazakii* was isolated from rice seed [dried product] [5], infant food [14], rice, rice starch and rice flour [6, 12]. *C. sakazakii* is considered an opportunistic pathogen that has been implicated in severe forms of necrotizing colitis and meningitis, especially in neonates [1].

Outbreaks of infections have implicated powdered milk substitute infant formulas as vehicles of *C. sakazakii* [14]. Many countries regulate specific mycotoxins and most countries try to limit exposure to the toxins. Community maximum levels for certain contaminants

in foodstuffs were established by Commission Regulation [EC] No 1881/2006 of 19 December 2006 [15]. Turkish Food Codex [TFC] Regulation on Contaminants [16] was prepared in parallel with the European Union Commission Regulation 1881/2006/EC. TFC Regulation on Contaminants in foods (Law of Authorization: 5996 and Official Gazette of Publication: 29.12.2011-28157) sets a limit of 5µg/g for OTA in unprocessed cereals, 3 µg/g for products (except those listed below) and 0.5 µg/g for food supplements for infants and young children and dietary foodstuffs for special medical purposes for infants.

TFC Regulation on Microbiological Criteria was parallel with the EC Regulation 2073/2005/EC on Microbiological Criteria for Foodstuffs. Accordingly, *C. sakazakii* as a Food Safety Criteria mustn't be in infant formulae and follow-up formulae. Enterobacteriaceae spp. for food supplements for infants and children [including dietary foodstuffs for special medical purposes] mustn't exceed 10³cfu g⁻¹.

The objective of this study was to investigate the prevalence of *C. sakazakii*, Enterobacteriaceae spp. and OTA in commercial Infant Rice-based formula (IRF) and milled rice (MR) products. A total of 10 samples were obtained from market, two samples were get flour mill manufacture area and one from storage/warehouse place.

MATERIALS AND METHODS

All of the analyses were performed using accreditation methods. Accreditation Number given by Turkish Accreditation Agency (TURKAK) is AB-0566-T and Revision Number is 07. All media materials used in the study were

obtained from Oxoid, UK.

Sample collection

In this study, a total of 4 different random commercial Infant Rice-based formula and 6 milled rice packaged products were purchased from retail stores. Two of milled rice products were provided by a mill manufacture area and one of storage/sales place. The samples between 125 and 250 g weights collected in November and December 2016 were manufactured in 4 different cities. Sample information is given in Table 1. Collected samples were taken to the laboratory without delay in accordance with Regulation on Turkish Food Codex Microbiological Criteria [17]. Each sample was labeled to identify the source, site and date of sampling. The other information were added Appendix 1.

Detection, isolation and identification of *C. sakazakii*

The presence of *C. sakazakii* was detected using ISO/TS 22964/IDF/RM 210 method [18] (Milk and milk products-Detection of *E. sakazakii*). Typical colonies on a chromogenic isolation agar, form yellow colonies on tryptone soya agar and display biochemical characteristics as described, when tests are carried out in accordance with this technical specification. In accordance with the interpretation of the test results of isolation of presumptive *C. sakazakii*, report the presence or absence of presumptive *C. sakazakii* in the test portion. In this case, no confirmation of the presumptive *C. sakazakii* found on the chromogenic plate has been carried out. After

Table 1. Information about investigated samples.

Sample_id	Sample	Country	Year	Brand	City
1	Fresh Milled rice flour	Turkey	2016	Medium scale	Samsun
2	Fresh Milled rice flour	Turkey	2016	Medium scale	Samsun
3	Milled rice flour in bag	Turkey	2016	Medium Scale	Samsun
4	Rice flour with milk and banana	Turkey	2016	Big scale	Ankara
5	Rice flour with milk, 12 vitamins and 6 minerals	Turkey	2016	Big scale	Istanbul
6	Supplementary food with milk and rice for baby and small children	Turkey	2016	Big scale	Ankara
7	Rice flour with milk and 7 cereals (for night)	Turkey	2016	Big scale	Istanbul
8	Rice flour	Turkey	2016	Big scale	Istanbul
9	Rice flour	Turkey	2016	Big scale	Istanbul
10	Rice flour	Turkey	2016	Big scale	Ankara
11	Rice flour	Turkey	2016	Big scale	Kocaeli
12	Rice flour	Turkey	2016	Big scale	Istanbul
13	Rice flour	Turkey	2016	Big scale	Istanbul

confirmation test, of one or more of the presumptive *C. sakazakii*, report the presence or absence of *C. sakazakii* in the test portion. Specify the final test result per mass [in grams] or per volume [in millilitres] of the analysed test sample.

Detection and Enumeration of *Enterobacteriaceae* spp.

Microorganisms that form characteristic colonies on violet red bile glucose agar and that ferment glucose and show a negative oxidase reaction when the tests are carried out in accordance with the methods specified in ISO 21528-2:2004 [19]. Number of *Enterobacteriaceae* counts in per gram of the test sample is calculated from the number of confirmed typical colonies per dish.

Determine OTA levels

The aim of the following work was to determine OTA levels in the samples from manufacture, sales and storage place in Turkey. A developed method using OCHRAPREP® (REFN: A9-P14.V4) in conjunction with HPLC described by AOAC 2000.003 [20] was used with slight modifications of the purification and HPLC conditions and with another confirmation method for OTA. The limit of quantitative measurement (LOQ) was 1.286 µg/kg. The method has been assessed and found to be suitable for the detection of OTA in cereal, offering average recoveries of 88%. The actual concentration of ochratoxin A is calculated using the following equation.

Calculate the concentration of the ochratoxin A standard using the following calculation:

$$\begin{aligned} [\text{Ochratoxin A}] \left(\frac{\mu\text{g}}{\text{ml}} \right) &= \frac{\text{Abs}(333\text{nm}) \times \text{Molecular Weight} \times 1000}{\text{Ochratoxin A Extinction coefficient}} \\ &= \frac{\text{Abs}(333\text{nm}) \times 403 \times 1000}{5550} \\ &= \text{Abs}(333\text{nm}) \times 72.6 \end{aligned}$$

RESULTS

Table 2 summarizes the result of *C. sakazakii*, *Enterobacteriaceae* spp. and OTA values in Infant rice-based formula (IRF) and milled rice (MR) samples. *C. sakazakii* was not determined in any IRF and MC products. While *C. sakazakii* wasn't detected from any samples, *Enterobacteriaceae* spp. was determined average 3.46×10^4 cfu/g in four samples (30.77%) that was above the legal limit value (max 10^1 cfu/g).

C. sakazakii was not isolated from any samples (n=13).

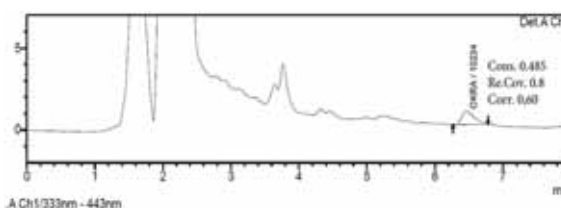


Figure 1. Chromatogram obtained from MR samples of 6 spiked with OTA.

The negative strains of *C. sakazakii* formed yellow colonies on TSA after 24–72 h of incubation at 25°C and blue-green colonies after 24 h of incubation at 37°C on DFI medium. The determination of high level of *Enterobacteriaceae* in IRF and MR has potential hazardous for pathogen foodborne enteric bacteria especially for *C. sakazakii*. The number of *Enterobacteriaceae* spp. was average 3.46×10^4 cfu/g. 4 of 13 samples (30.77%) was exceed EC limits (10^1 cfu/g). One of the samples (7.69%) taken from market had levels of mycotoxin (0.6 µg/kg) above maximum level for certain contaminants in foodstuffs (0.5 µg/kg) (Figure 1). OTA contamination in the other samples wasn't present.

DISCUSSION

A great deal of studies has focused on the infant formula as the main source of serious pathogens [3, 5, 11]. But, few researchers a little researcher focused on the infant formula including ground cereal such as rice, semolina etc. for the main source of pathogen [14, 19, 21]. Rice flour is commonly used as an infant formulae ingredient. If it is contaminated in any production stage, the microbiological hazard and risk could be transported to the last product. Nazarowec-White and Farber [22] stated that *E. sakazakii* can gain access to the powder from the environment or from the addition of the ingredients at the powder stage. Iversen and Forsythe [10] reported that the presence of *E. sakazakii* in powdered infant milk formula depends on the process conditions and nature of the product. The bacterium has been isolated from rice [5] but its survival characteristics in infant rice cereal are not known. Post processing contamination of rice cereal with *C. sakazakii*, followed by survival throughout the expected shelf-life of the product, would result in its presence.

The presence of *Enterobacteriaceae* spp. respects the poor hygienic conditions of the environment of factories and cross contamination [7]. The manufacture environments taken by MR samples and also personnel hygienic conditions weren't sufficient. The mill equipment used in rice flour was not suitable for good manufacturing practices. The contamination by *Enterobacteriaceae* means that it should be designated sampling plans and limits for the level of *Enterobacteriaceae* spp. in baby foods for food business operators as part of the process hygiene criteria. The initial *Enterobacteriaceae* contamination level in the raw materi-

Table 2. The results for *C. sakazakii*, *Enterobacteriaceae* spp. and OTA analysis

Sample id	Analyte	is less than (legal limit)	Determined Value	Units	Uncertainty
1	<i>C. sakazakii</i>	0	not detected	g mL ⁻¹	
	<i>Enterobacteriaceae</i> spp.	100	5.6x10 ⁸	cfu g ⁻¹	
	Ochratoxin-A	0.5	not detected	µg kg ⁻¹	±0.156%
2	<i>C. sakazakii</i>	0	not detected	g mL ⁻¹	
	<i>Enterobacteriaceae</i> spp.	100	7.5x10 ²	cfu g ⁻¹	
	Ochratoxin-A	0.5	not detected	µg kg ⁻¹	±0.156%
3	<i>C. sakazakii</i>	0	not detected	g mL ⁻¹	
	<i>Enterobacteriaceae</i> spp.	100	<10	cfu g ⁻¹	
	Ochratoxin-A	0.5	not detected	µg kg ⁻¹	±0.156%
4	<i>C. sakazakii</i>	0	not detected	g mL ⁻¹	
	<i>Enterobacteriaceae</i> spp.	100	<10	cfu g ⁻¹	
	Ochratoxin-A	0.5	not detected	µg kg ⁻¹	±0.156%
5	<i>C. sakazakii</i>	0	not detected	g mL ⁻¹	
	<i>Enterobacteriaceae</i> spp.	100	2.6x10 ²	cfu g ⁻¹	
	Ochratoxin-A	0.5	not detected	µg kg ⁻¹	±0.156%
6	<i>C. sakazakii</i>	0	not detected	g mL ⁻¹	
	<i>Enterobacteriaceae</i> spp.	100	<10	cfu g ⁻¹	
	Ochratoxin-A	0.5	0,6	µg kg ⁻¹	±0.156%
7	<i>C. sakazakii</i>	0	not detected	g mL ⁻¹	
	<i>Enterobacteriaceae</i> spp.	100	2.8x10 ⁴	cfu g ⁻¹	
	Ochratoxin-A	0.5	not detected	µg kg ⁻¹	±0.156%
8	<i>C. sakazakii</i>	0	not detected	g mL ⁻¹	
	<i>Enterobacteriaceae</i> spp.	100	<10	cfu g ⁻¹	
	Ochratoxin-A	0.5	not detected	µg kg ⁻¹	±0.156%
9	<i>C. sakazakii</i>	0	not detected	g mL ⁻¹	
	<i>Enterobacteriaceae</i> spp.	100	<10	cfu g ⁻¹	
	Ochratoxin-A	0.5	not detected	µg kg ⁻¹	±0.156%
10	<i>C. sakazakii</i>	0	not detected	g mL ⁻¹	
	<i>Enterobacteriaceae</i> spp.	100	<10	cfu g ⁻¹	
	Ochratoxin-A	0.5	not detected	µg kg ⁻¹	±0.258%
11	<i>C. sakazakii</i>	0	not detected	g mL ⁻¹	
	<i>Enterobacteriaceae</i> spp.	100	<10	cfu g ⁻¹	
	Ochratoxin-A	0.5	not detected	µg kg ⁻¹	±0.258%
12	<i>C. sakazakii</i>	0	not detected	g mL ⁻¹	
	<i>Enterobacteriaceae</i> spp.	100	<10	cfu g ⁻¹	
	Ochratoxin-A	0.5	not detected	µg kg ⁻¹	±0.258%
13	<i>C. sakazakii</i>	0	not detected	g mL ⁻¹	
	<i>Enterobacteriaceae</i> spp.	100	<10	cfu g ⁻¹	
	Ochratoxin-A	0.5	not detected	µg kg ⁻¹	±0.258%

als is predominantly governed by Good Hygiene Practices [23].

Cereal based infant products are potential sources for mycotoxins such as OTA [3, 24]. Although some researchers have found the contamination of OTA and the other mycotoxins in retailed rice [25, 26], a smaller survey of the actual incidence of mycotoxins in IRF has been reported. In a survey by Lombaert et al. [3] demonstrated the regular occurrence of multiple mycotoxins in cereal-based infant foods. In recent publications, OTA has been reported to be prevalent at very low concentrations in infant and baby cereal foods. Wolff [7] and Beretta et al. [8] have been established the maximum OTA levels as 2.13 and 0.7 ng/g, respectively. The OTA concentration in IRF sample found in this investigation (0.6 ng/g) was higher than these results. Rice-based infant formulae contained higher amount than legal limit of OTA as determined in this study. Although the production companies of the samples had a HACCP management system certification, microbiological hazard criteria was not acceptable according the TFC limits.

CONCLUSION

Microbiological risk in baby foods especially with grain mixed should be widely searched to exhibit potential risks. It should be followed up all of the processing steps in order to prevent contamination to the last product. The findings of this study suggest that the flour mill conditions have poor hygiene. The initial *Enterobacteriaceae* contamination level in the raw materials is predominantly governed by Good Hygiene Practices. Mycotoxin contamination should be more following up by food business operators. *C. sakazakii*, *Enterobacteriaceae* spp. and OTA analyses in infant foods must be involved in provincial annual control plan by Republic of Turkey Ministry of Food, Agriculture and Livestock.

Acknowledgements

The analysis used in this study was performed and supported by Accredited NanoLab Food and Feed Analysis and Control Laboratory in İstanbul.

REFERENCES

1. Heuvelink AE, Kodde FD, Zwartkruis-Nahuis JTM, de Boer E. 2001. *Enterobacter sakazakii* in melkpoeder. Keuringsdienst van Waren Oost. Project number OT 0110.
2. Himelright I, Harris E, Lorch V, Anderson M, Jones T, Craig A, Kuehnert M, Forster T, Arduino M, Jensen B, Jernigan D. *Enterobacter sakazakii* infections associated with the use of powdered infant formula-Tennessee. 2001. Morbidity Mortality Weekly Report 51 (2002) 298-300.
3. Lombaert GA, Pellaers P, Roscoe V, Mankotia M, Neil R, Scott PM. Mycotoxins in infant cereal foods from the Canadian retail market. *Food Additives and Contaminants* 20 (2003) 494-504.
4. Cottynne B, Regalado E, Lanoot B, De Cleene M, Mew TW, Swings J. Bacterial populations associated with rice seed in the tropical environment. *Phytopathology* 91 (2001) 282-292.
5. Iversen C, Lane M, Forsythe SJ. The growth profile, thermotolerance and biofilm formation of *Enterobacter sakazakii* grown in infant formula milk. *Letters in Applied Microbiology* 38 (2004) 378-382.
6. Gurtler JB, Kornacki JL, Beuchat LR. *Enterobacter sakazakii*: a coliform of increased concern to infant health. *International Journal of Food Microbiology* 104 (2005) 1-34.
7. Wolff J. Ochratoxin A in cereals and cereal products. *Archiv für Lebensmittelhygiene* 51 (2000) 85-88.
8. Beretta B, De Dominic R, Gaiaschi A, Ballabio C, Galli CL, Gigliotti C, Restani P. Ochratoxin A in cereal-based baby foods: occurrence and safety evaluation. *Food Additives and Contaminants* 19 (2002) 70-75.
9. Fowler M. Flour mill contamination. <http://www.worldgrain.com/Departments/Milling-Operations/2013/5/Flour-mill-contamination.aspx?cck=1> (2013).
10. Iversen C, Forsythe S. Risk profile of *Enterobacter sakazakii*, an emergent pathogen associated with infant milk formula. *Trends in Food Science and Technology* 14 (2003) 443-454.
11. Tanaka K, Sago Y, Zheng Y, Nakagawa H, Kushiro M. Mycotoxins in rice. *International Journal of Food Microbiology* 119 (2007) 59-66.
12. Richards GM, Gurtler JB, Beuchat LR. Survival and growth of *Enterobacter sakazakii* in infant rice cereal reconstituted with water, milk, liquid infant formula, or apple juice. *Journal of Applied Microbiology* 99 (2005) 844-850.
13. Iversen C, Forsythe SJ. Isolation of *Enterobacter sakazakii* and other *Enterobacteriaceae* from powdered infant milk and related products. *Journal of Food Microbiology* 21 (2004) 771-777.
14. Simmons BP, Gelfand MS, Haas M, Metts L, Ferguson J. 1989. *Enterobacter sakazakii* infections in neonates associated with intrinsic contamination of a powdered infant formula. *Infection Control and Hospital Epidemiology*. 10: 398-401.
15. FAO/WHO. Food and Agriculture Organization and World Health Organization of the United Nations. *Enterobacter sakazakii* and Salmonella in powdered infant formula: meeting report. [/ftp://ftp.fao.org/ag/agn/jemra/e_sakazakii_salmonella.pdf](ftp://ftp.fao.org/ag/agn/jemra/e_sakazakii_salmonella.pdf). (2006).
16. EC. Commission Regulation No 1881/2006 setting maximum levels for certain contaminants in foodstuffs (2006).
17. TFC. Turkish Food Codex Microbiological Criteria Regulation. <http://www.resmigazete.gov.tr/eskiler/2011/12/20111229M3-6.html> (2011).
18. ISO/TS 22964 IDF/RM 210. Technical specification: Milk and milk products-Detection of *Enterobacter sakazakii*. First Edition 2006-02-01.
19. BS ISO 21528-2: British Standard. Microbiology of food and animal feeding stuffs-Horizontal methods for the detection and enumeration of *Enterobacteriaceae* -Part 2: Colony-count method. 2004.
20. Anonymous. Application note for Cereal Ochratoxin A Extraction Method. R-Biopharm Rhone Ltd. Ref N:A-9 P14.

- V4, Date: May 2009.
21. Baylis C, Uyttendaele M, Joosten H, Davies A. The Enterobacteriaceae and their significance to the Food Industry. Printed in Belgium D/2011/10.996/30 ISBN 9789078637332 (2011).
 22. Nazarowec-White M, Farber JM. Incidence, survival and growth of *Enterobacter sakazakii* in infant formula. *Journal of Food Protection* 60 (1997) 226-230.
 23. FAO. Food and Agriculture Organization of the United States. Good hygiene practices and HACCP. <http://www.fao.org/food/food-safety-quality/capacity-development/haccp/en/> November, 2017.
 24. Larry R, Beuchat A, Hoikyung KB, Joshua B, Gurtler C, Li-Chun L, Jee-Hoon R, Glenner MR. *Cronobacter sakazakii* in foods and factors affecting its survival, growth, and inactivation. *International Journal of Food Microbiology* 2009 (136) 204-213.
 25. Scott PM. *Penicillium and Aspergillus toxins. Mycotoxins in Grain: Compounds Other than Aflatoxin*, edited by J. D. Miller and H. L. Trenholm (St Paul: Eagan), 1994 (261-285).
 26. Speijers GJA, Van Egmond HP. Worldwide ochratoxin A levels in food and feeds. *Human Ochratoxicosis and its Pathologies. Colloque INSERM*, edited by E. E. Creppy, M. Castegnaro and G. Dirheimer (Montrouge, France: John Libbey Eurotext Ltd). 1993 (231) 85-100.

Mineralogical and Geochemical Characterization of Ancient Ceramic Sherds from Dipsizin Cave (Karaman, Turkey)

M. Yavuz HÜSEYİNCA¹  Osman DOĞANAY²

¹Selçuk University, Department of Geological Engineering, Konya, TURKEY

²Aksaray University, Department of Archaeology, Aksaray, TURKEY

ABSTRACT

Raw materials of two ancient ceramic sherds (ceramic-1 and ceramic-2) from Dipsizin Cave were analyzed by SEM-EDS in order to characterize ceramic fabrics. Characterization includes separation of temper and clay paste sections, qualitative determination of mineralogical compositions and percentage calculations of raw materials by region sketching. In this perspective, ceramic-1 is characterized as % 41.83 temper (quartz, albite, rutile, lime, organic material) and % 58.17 clay paste. Then, ceramic-2 is characterized to be % 37.52 temper (quartz, anorthoclase, rutile, lime, organic material) and % 62.48 clay paste. Clay paste sections of both ceramics include mixture of clay minerals belonging to illite and smectite clay groups. In comparison, percentages of temper and clay paste sections of ceramic-1 and ceramic-2 differ % 4.31 from each other and variety of raw materials making up both ceramic bodies are nearly same except feldspars. But individually quartz and lime percentages between ceramics differ nearly two times. In this opinion we realize that raw materials are mixed by tracking two recipes. These recipes can be explained by different pottery making technologies and/or different archaeological provenances.

Keywords:

Ceramic Sherd; Characterization; Dipsizin Cave; Region Sketching, Sariveliler, SEM-EDS

Article History:

Received: 2017/05/05

Accepted: 2017/11/04

Online: 2018/04/06

Correspondence to: M. Yavuz Huseyinca,
Selcuk University, Department of Geological
Engineering, 42250, Konya, TURKEY
E-Mail: yhuseyinca@selcuk.edu.tr
Phone: +90 332 223 2115
Fax: +90 332 241 0635

INTRODUCTION

Dipsizin Cave is located in the vicinity of Sariveliler District of Karaman Province in Turkey (Figure 1). In ancient times the cave was located in Cilicia Region and to the south of Isauria Region (Figure 2) [1]. A strata of soil which contains remnants indicative of human usage is defined as cultural soil. The unique specification distinguishing Dipsizin Cave from its analogues in the Taurus Mountains is its cultural soil as it is found rarely in caves (Figure 3a, b). This soil includes numerous ceramic fragments and some of them giving date and form have been cataloged. Archaeological specifications of these ceramics indicate that they are brought from different regions into the cave and this cave was a temporary resting place or a shelter for caravans traveling between the ancient cities like Pharax, Zenonopolis, Lamos and Golgosos [2].

In this study raw materials of ceramic-1 (C-1) and ceramic-2 (C-2) (Figure 4a, b) from the catalog were investigated for characterization under the perspective of "provenance studies involve characterization of ancient ceramics" [3]. Raw materials used for pottery making can be categorized into three parts; clays, tempers and glazes. Clay, which is the dominant constituent plays most important role with two properties. First is the plasticity for taking shape before firing and the second is conservation of its shape while and after firing. Chemically, clays are hydrous aluminum silicates, usually containing minor amounts of impurities such as K, Na, Ca, Mg or Fe [4, 5]. There are three major clay mineral groups (kaolinite, illite and smectite) and they have chemically distinct compositions. However most ancient pottery was made from a mixture of these clay groups.



Figure 1. Geographic location of Dipsizin Cave

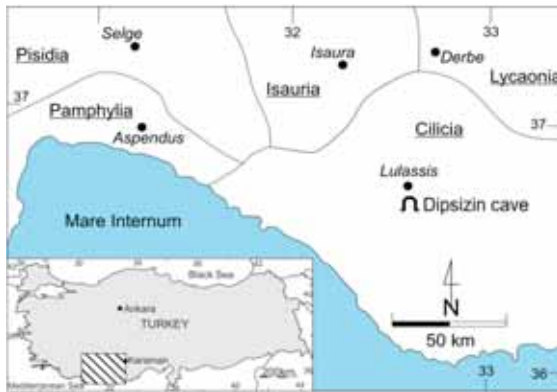


Figure 2. Settlement around Dipsizin Cave in ancient ages

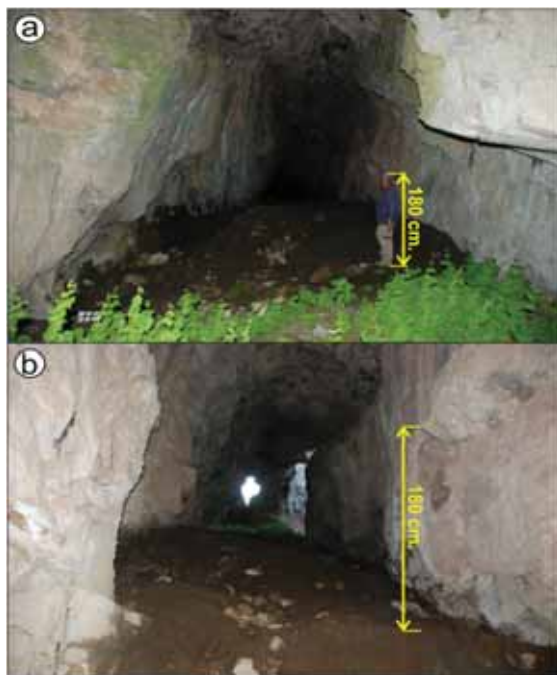


Figure 3. Photographs showing interior (a) and entrance (b) of Dipsizin cave

Some clays are suitable for potting and straightly dug from the deposit but some have to be mixed as they are not plastic enough or too plastic [6]. Tempers are additives mixed in order to reduce shrinkage of the final product and to improve workability of the clay paste. A wide variety of raw materials

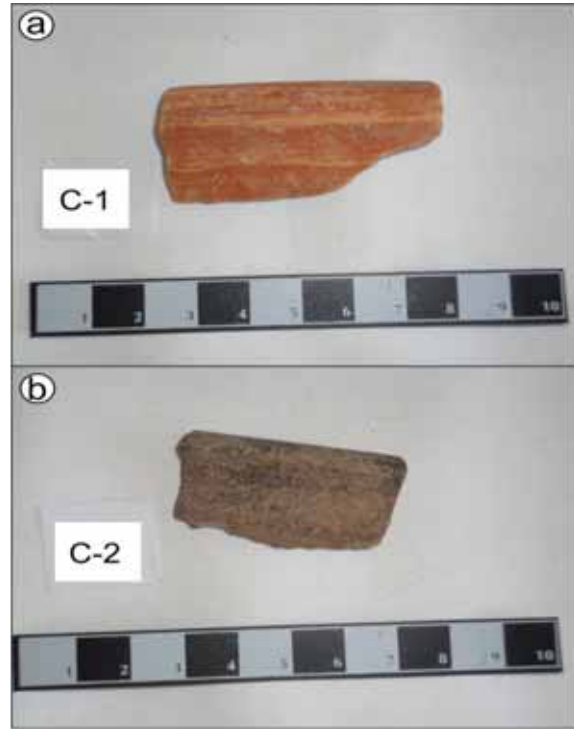


Figure 4. Catalog photographs of C-1 (a) and C-2 (b)

such as quartz sand, fossil shells, calcite, mica, crushed rock, and organic materials can be used as a temper [7, 8]. Glazes are glassy coatings melted on the surface of the pottery to make them waterproof and to give decorative features. All glazes consist of mainly silica and some flux agents. The color of the glaze directly depends on the type of the flux agent and the firing temperature of the pot [6].

This study aims to define above mentioned raw materials and their percentages used in obtained ceramics by applying non-destructive methods. This procedure will help to determine producing technologies and/or archaeological provenances of the ceramics which play important role in archaeology.

GEOLOGICAL FRAMEWORK

Dipsizin Cave is geographically located in the Central Taurus Mountains which is part of the Taurus orogenic belt. This belt is composed of several tectonic rock slices (namely Bolkardağı, Aladağ, Geyikdağı, Alanya, Bozkır and Antalya) so that they have long tectonic contacts with each other and reflect different basin conditions [9-12]. General lithology of these rocks deposited in the Cambrian - Eocene age interval include metamorphosed carbonates, clastics and ophiolitic rocks. In the central part of the Taurus Belt, basement rocks are unconformably overlaid by the post-Eocene aged Mut Basin deposits which include horizontally bedded clastics and carbonates [13, 14]. Formation of Dipsizin cave within the metacarbonates

nates of the basement rocks can be explained by karstic dissolution mechanism.

MATERIAL AND METHODS

This work is focused on the application of Scanning Electron Microscopy (SEM) and Energy Dispersive Spectroscopy (EDS) techniques to C-1 and C-2 obtained from Dipsizin cave. SEM is a high magnification microscope which the image is generated by the interaction of generated high energy electrons and sample atoms. With it, EDS is a micro-analytical technique conventionally used in SEM for the local determination of chemical elements in solid samples [15]. In this technique a special energy-sensitive detector adapted to SEM receives the generated X-rays and sorts them according to energy. A computer software analyzes the spectrum and looks for characteristic peaks indicative of certain elements. Besides determining elemental composition of individual points on the sample, EDS analysis can be used to map out the lateral distribution of elements from the imaged area. These maps can give accurate results of relative element proportions to understand the material properties [16]. On the overall the EDS microanalysis is regarded as a non-destructive technique and applied to many problems of archaeological ceramics [17-21].

In the study, the samples were bombarded with high energy electrons produced by tungsten filament emitter under accelerating voltage of 15 keV in SEM-EDS. Element distribution (ED) map images of silicon (Si), titanium (Ti), sodium (Na), carbon (C), calcium (Ca), aluminum (Al), potassium (K), oxygen (O), magnesium (Mg) and iron (Fe) are taken under the magnification level of 400X. Then each ceramic fabric is investigated under the sections of temper and clay paste. Sections are separated according to the grain size contrast between them. Noticeable contrast indicates manual addition of temper to clay [8]. After separation process, element distribution (ED) maps, EDS analysis and compositions of standard minerals are evaluated for mineralogical considerations. Region sketches and percentages are obtained from image analyzing software (Image-Pro).

RESULTS AND DISCUSSION

An ED map specifies a single element content and distribution in the defined area with a color code. Colors of ED maps are assigned automatically by the computer to a single chemical element. Accordingly, the total element content in the defined area is separated to numerous single element maps. On the contrary to this definition, starting from the induction method our theory is to arrive at the total element content in that area by the proper combination of each element map. To do this, element

maps are manually placed on top of each other to search for overlapping in colors. Then it is found out which elements constitute the areas where the overlaps occur. In the next step mineralogy is determined by comparing the found element association with the contents of proper EDS points and known minerals. Defining mineralogy is important step for calculating raw material percentages which is valuable for evaluating production technologies of ceramics. In this concept characterizations of C-1 and C-2 are explained under separate titles.

Characterization of C-1

SEM secondary electron image (SEI) and backscattered electron image (BEI) with EDS locations are shown in Figure 5a, b. SE and BE images help to understand surface topography and element distribution of the scanned area respectively [19]. Color coded ED maps of Si (white), Ti (blue), Na (turquoise), C (red), Ca (purple), Al (cyan), K (brown), O (green), Mg (violet) and Fe (olive) are also shown in Figure 5c- l. High brightness of a color indicates a high concentration of related element or vice versa. The black color means no concentration of related element in the map [15].

To find qualitative composition of white colored regions in ED map of Si (Figure 5c) we superpose other ED maps for overlapping colors. Then we conclude that there is only green colored regions in O map (Figure 5j) indicating Si and O are the main constituents of our white regions. For mineralogical determination, beside proper overlapping in ED maps we look for a mineral whose chemical composition is close to point 5a (Table 1) in terms of defined element variety. In this concept quartz mineral (% 46.74 Si) has very close composition to point 5a (% 45.72 Si) and suggest that our white colored regions are quartz. Distribution of Na concentration is represented by the turquoise colored regions in ED map (Figure 5e). When manually superposed, colors overlapped with the mentioned regions belong to Al, Si and O maps (Figure 5h, c, j). Therefore, our candidate mineral qualitatively includes Na, Al, Si and O elements. In order to identify this mineral, the similarity between the quantitative compositions of point 2a (% 6.82 Na, % 10.89 Al and % 32.92 Si) and a mineral with standard formula is compared in terms of defined elements. Here, albite (% 8.77 Na, % 10.29 Al and % 32.13 Si) is suggested which has closest content to 2a point (Table 1). Ti concentration is represented by blue colored regions in ED map (Figure 5d). When superposed, overlapping colors with related regions are only in O map (Figure 5j) indicating that our mineral contains Ti and O elements. Comparison between point 9a (% 58.80 Ti and % 0.86 Fe) in Table 1 and rutile content (% 58.43 Ti and % 1.83 Fe) verifies similarity of contents and suggest that our blue colored grains are rutile. We know that rutile is stable in

Table 1. Chemical compositions of points 1a to 10a (wt%) for C-1.

Element/ Point	C	O	Na	Mg	Al	Si	K	Ca	Ti	Fe	Sum
1a	3.20	43.91	7.35	0.00	10.89	32.92	0.44	0.19	0.31	0.78	99.99
2a	0.00	47.56	6.82	0.10	11.08	33.84	0.12	0.21	0.00	0.00	99.73
3a	9.70	41.15	0.00	4.79	10.39	20.82	1.89	1.45	1.02	8.79	100.00
4a	9.25	41.40	0.44	1.16	16.51	23.24	4.26	1.17	0.27	2.28	99.98
5a	6.56	46.32	0.21	0.04	0.65	45.72	0.00	0.11	0.11	0.25	99.97
6a	77.86	12.08	0.45	0.26	0.74	1.55	0.08	0.00	0.00	0.00	93.02
7a	12.05	37.00	0.60	0.23	10.11	28.00	8.87	0.78	0.41	1.79	99.84
8a	12.17	43.53	0.12	0.25	9.64	13.64	0.44	17.81	0.16	2.01	99.77
9a	4.35	31.79	0.27	0.18	1.26	1.83	0.34	0.29	58.80	0.86	99.97
10a	6.09	43.21	0.00	2.87	10.67	17.33	1.02	1.30	1.11	16.35	99.95

most weathering environments and generally can mix with clay [22-24]. Ca content is shown by purple colored regions in ED map (Figure 5g). When superposed, green color of O map overlaps with these regions. So, element variety includes Ca and O but not C. Therefore our purple colored and pellet shaped regions should be lime rather than grounded calcium carbonate (CaCO_3). C distribution is represented by red colored regions in ED map (Figure 5f). When superposed there is no other element color overlapping with these

regions. Mono elemental variety and high C (% 77.86) content in point 6a (Table-1) suggest that these regions should be organic material. Organic material can be found with clay naturally or can be added to mixture by pottery maker in order to improve plasticity and firing conditions [6].

Accordingly, temper section of C-1 is composed of quartz (SiO_2), albite ($\text{NaAlSi}_3\text{O}_8$), rutile (TiO_2), lime (CaO) and organic material. Percentages of these constituents are calculated as % 12.00, % 0.73, % 0.85, % 18.10 and % 10.15 respectively and summed to % 41.83 according to image analysis (Figure 6). Above mentioned raw materials are all included into the temper section as they are not clay in mineralogy. Finally, C-1 is characterized to be % 41.83 temper and remaining % 58.17 clay paste.

To determine clay paste section remained from the temper section we obtain proper overlapping of Al, Si and O elements as clays are hydrous aluminum silicates. After verifying this we see that overlapping of K, Mg and Fe occurs too (Figure 5i, k, l). These are probably impurities that can take place in clay minerals. Especially, K prefers mainly illite group [25], whilst Mg and Fe prefer smectite group clay minerals [5]. Therefore clay section of C-1 seems to be the mixture of clay minerals belonging to illite and smectite group.

Characterization of C-2

SEI, BEI including EDS locations and color coded ED maps of Si (white), Ti (turquoise), Na (blue), C (red), Ca (brown), Al (cyan), K (magenta), O (green), Mg (violet) and Fe (olive) belonging to C-2 are shown in Figure 7a, l. Chemical compositions of points 1b to 10b are also shown in Table 2. Separation of temper and clay paste sections, identification of minerals and percentage calculations within C-2 are performed as done in C-1.

White colored regions in Si map (Figure 7c) overlap only with green colors of O map (Figure 7j) indicating that these regions include Si and O elements. Consistency between quantitative compositions of point 5b (% 44.77 Si) in

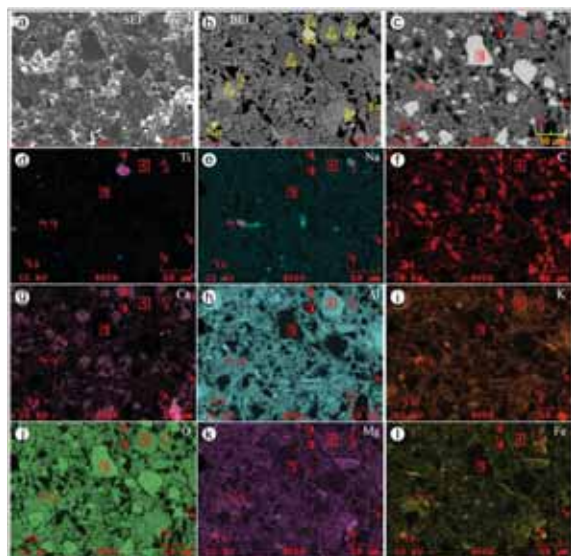


Figure 5. SEI (a), BEI adapted with EDS locations (b) and ED maps of Si (c), Ti (d), Na (e), C (f), Ca (g), Al (h), K (i), O (j), Mg (k) and Fe (l) for C-1

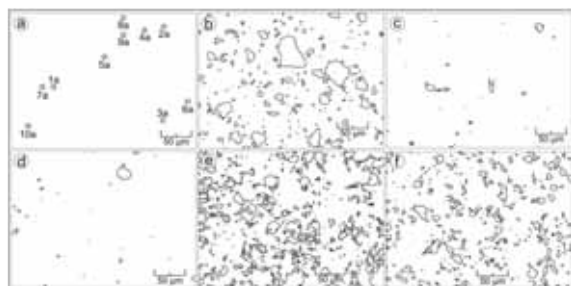


Figure 6. SEI (a), EDS locations of points 1a to 10a (a) and region sketches of quartz (b), albite (c), rutile (d), lime (e) and organic material (f) for C-1

Table 2. Chemical compositions of points 1b to 10b (wt%) for C-2.

Element/ Point	C	O	Na	Mg	Al	Si	K	Ca	Ti	Fe	Sum
1b	64.07	17.95	0.23	0.18	2.67	12.84	0.69	0.67	0.27	0.00	99.57
2b	9.45	41.77	5.49	0.13	9.88	28.66	2.72	0.33	0.25	0.99	99.67
3b	7.94	42.15	0.00	5.60	11.26	20.19	0.50	0.75	0.31	11.06	99.76
4b	9.24	39.63	0.54	0.25	20.48	23.71	3.55	0.41	0.15	1.69	99.65
5b	6.72	46.75	0.09	0.06	0.64	44.77	0.07	0.16	0.01	0.24	99.51
6b	0.00	41.27	0.72	1.32	3.10	27.59	2.62	3.01	0.00	0.00	79.63
7b	12.60	38.77	0.36	0.08	9.46	29.32	7.69	0.00	0.26	1.33	99.87
8b	3.62	44.26	0.45	0.88	12.02	20.42	1.65	14.23	1.23	0.00	98.76
9b	3.02	40.97	0.17	0.60	8.07	14.13	1.49	0.40	25.81	5.21	99.87
10b	6.69	41.45	0.13	3.93	13.12	16.54	1.36	0.80	1.17	14.37	99.56

Table 2 and quartz (% 46.74 Si) suggest that our regions are quartz grains. Blue colored regions in Na map overlaps with Al, Si and K elements when superposed (Figure 7e, h, c, i). So, Na, Al, Si and K elements are main constituents of blue colored regions. Consistency between chemical compositions of point 2b (% 5.49 Na, % 2.72 K, % 9.88 Al and % 28.66 Si) and anorthoclase (% 5.45 Na, % 2.47 K, % 11.71 Al and % 29.35 Si) suggest that these regions are anorthoclase grains. Turquoise colored regions in Ti map overlap only with O

(Figure 7d, j). So, chemical variety include Ti and O for the candidate mineral. Close chemical compositions of point 9b (Table 2) and rutile suggest that mentioned regions could be rutile. Brown colored regions in Ca map overlap with green color of O map (Figure 7g, j) but don't with C map indicating that these pellet shaped regions are lime rather than grounded limestone. C distribution is represented by red colored regions in ED map (Figure 7f). High C content of point 1b (% 64.07) in Table 2 and no overlapping of any element with these regions indicate organic material origin.

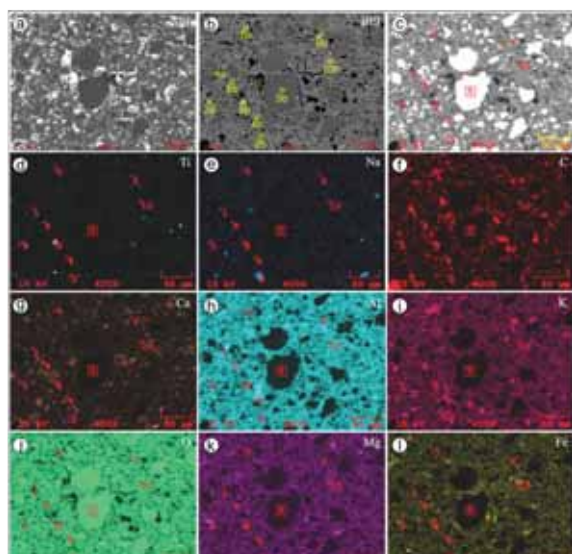


Figure 7. : SEI (a), BEI adapted with EDS locations (b) and ED maps of Si (c), Ti (d), Na (e), C (f), Ca (g), Al (h), K (i), O (j), Mg (k) and Fe (l) for C-2

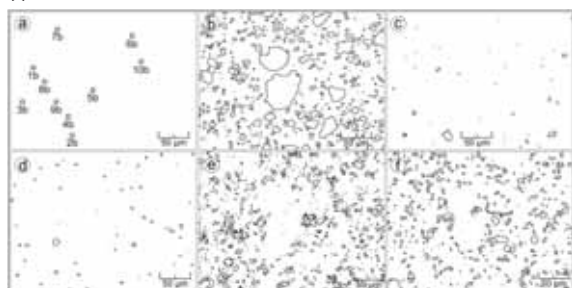


Figure 8. : EDS locations of points 1b to 10b (a) and region sketches of quartz (b), anorthoclase (c), rutile (d), lime (e) and organic material (f) for C-2

Accordingly, temper section of C-2 is composed of quartz (SiO_2), anorthoclase ($\text{K,NaAlSi}_3\text{O}_8$), rutile (TiO_2), lime (CaO) and organic material. Percentages of these constituents are calculated as % 20.10, % 0.55, % 0.62, % 8.25 and % 8.00 respectively and summed to % 37.52 according to region sketches (Figure 8). Then C-2 is characterized to be % 37.52 temper and remaining % 62.48 clay paste section.

In clay paste section of C-2 we see overlapping of Al, Si and O elements indicating clay mineral existence. We see also overlapping of K, Mg and Fe (Figure 7i, k, l) which could be evaluated as impurities in clay minerals. As a result we can suggest that clay paste section of C-2 is a mixture of clay minerals belonging to illite and smectite groups as in C-1.

CONCLUSION

As a result of the study, following items can be arranged:

1- C-1 is characterized as % 41.83 temper (quartz, albite, rutile, lime, organic material) and % 58.17 clay paste. Also, C-2 is characterized to be % 37.52 temper (quartz, anorthoclase, rutile, lime, organic material) and % 62.48 clay paste.

2- When compared, percentages of temper and clay paste sections in C-1 and in C-2 seem to be close in % 4.31 vicinity. But individually quartz and lime percentages of C-1 (% 12.00 quartz and % 18.10 lime) and C-2 (% 20.10 quartz and % 8.25 lime) differ nearly two times from each other. Noticeable diversity in percentages of quartz and lime sug-

gest that these raw materials are mixed following different recipes indicative of different production technologies and/or two distinct pottery makers within the meaning of different archaeological provenance.

3- In comparison, temper sections of both C-1 and C-2 have nearly same qualitative compositions except C-1 have albite and C-2 have anorthoclase.

4- Clay paste sections of ceramics both reflect mixture of clay minerals belonging to illite and smectite groups.

5- Similarity between the varieties of raw materials indicate common or close geological provenance.

6- Grain size contrast of quartz and pellet shaped structure of lime in both ceramic textures indicate manual addition of these.

7- Low percentages of feldspars and rutile indicate that they are not manually added.

8- High organic material content may indicate direct input of clay from a lake deposit or manual addition of it to improve plasticity of the mixture [6].

9- Percentage calculation of raw materials can give important data for characterization of ancient ceramics and behavior of pottery makers.

10- We suggest that characterization of ceramics could be done non-destructively by the procedure applied in this study.

ACKNOWLEDGMENTS

The authors thank the editor and anonymous reviewers for their constructive comments to the manuscript.

References

1. Heinrich, K, Asia citerior, in: David Rumsey historical map collection, Dietrich Reimer, Berlin, 1903.
2. Doğanay, O, Duman, B. Isauria bölgesi'nden bir grup seramik: Adiller Dipsizin mağarası, in: Ş. Dönmez (Ed.) Sümer Atasoy'a armağan yazılar, Hel Yayınları, Ankara, pp. 83-94, 2013.
3. Tite, MS. The impact of electron microscopy on ceramic studies. *Proceedings of the British Academy* 77 (1992) 111-131.
4. Guggenheim, S, Martin, RT. Definition of clay and clay mineral: Joint report of the AIPEA nomenclature and CMS nomenclature committees. *Clays and Clay Minerals* 43 (1995) 255-256.
5. Mukherjee, S. *The science of clays*, Springer Netherlands, India, 2013.
6. Rapp, G. *Archaeomineralogy*, second ed. Springer, Berlin Heidelberg, 2009.
7. Shepard, AO. *Ceramics for the archaeologist*, Carnegie institution, Washington, 1956.
8. Dickinson, WR. Petrographic temper provinces of prehistoric pottery in Oceania. *Records of the Australian Museum* 50 (1998) 263-276.
9. Özgül, N. Torosların bazı temel jeolojik özellikleri. *Türkiye Jeoloji Kurumu Bülteni* 19 (1976) 65-78.
10. Özgül, N. Bozkır-Hadım-Taşkent (Orta Toroslar'ın kuzey kesimi) dolayında yer alan tektono-stratigrafik birliklerin stratigrafisi. *Maden Tetkik ve Arama Dergisi* 119 (1997) 113-174.
11. Özgül, N, Arpat, E. Structural units of Taurus orogenic belt and their continuation in the neighbouring regions. *Geological Society of Greece Bulletin* 10 (1973) 156-164.
12. Gutnic, M, Monod, O, Poisson, A, Dumont, JF. *Geologie des Taurides occidentales (Turquie)*, Societe Geologique de France, Paris, 1979.
13. Gedik, A, Birgili, Ş, Yılmaz, H, Yoldaş, R. Mut-Ermenek-Silifke Yöresinin Jeolojisi ve Petrol Olanakları. *Türkiye Jeoloji Kurumu Bülteni* 22 (1979) 7-26.
14. Bassant, P, Van Buchem, FSP, Strasser, A, Görür, N. The stratigraphic architecture and evolution of the Burdigalian carbonate-siliciclastic sedimentary systems of the Mut Basin, Turkey. *Sedimentary Geology* 173 (2005) 187-232.
15. Reed, SJB. *Electron microprobe analysis and scanning electron microscopy in geology*, Cambridge University Press, U.K., 2005.
16. Goldstein, JI, Newbury, DE, Echlin, P, Joy, DC, Fiori, C, Lifshin, E. *Scanning electron microscopy and X-Ray microanalysis*, Plenum Publishing, New York, 1981.
17. Tite, MS, Freestone, IC. The use of scanning electron microscopy in the technological examination of ancient ceramics, in: J.S. Olin, A.D. Franklin (Eds.) *Archaeological Ceramics*, Smithsonian Institution Press, Washington, pp. 109-120, 1982.
18. Freestone, IC, Middletonand, AP. Mineralogical applications of the analytical SEM in archaeology. *Mineralogical Magazine* 51 (1987) 21-31.
19. Froh, J. Archaeological ceramics studied by scanning electron microscopy. *Hyperfine Interactions* 154 (2004) 159-176.
20. Laviano, R, Muntoni, IM. Provenance and technology of Apulian Neolithic pottery, in: M. Maggetti, B. Messiga (Eds.) *Geomaterials in Cultural Heritage Geological Society Special Publications*, London, pp. 49-62, 2006.
21. Wassilkowska, A, Czaplicka-Kotas, A, Zielina, M, Bielski, A. An analysis of the elemental composition of micro-samples using EDS technique. *Technical Transactions* 1 (2014) 133-148.
22. Morton, AC. Stability of detrital heavy tertiary sandstones from the north sea basin. *Clay minerals* 19 (1984) 287-308.
23. Pettijohn, FJ, Potter, PE, Siever, R. *Sand and Sandstone*, Springer New York, 1987.
24. Force, ER. *Geology of titanium-mineral deposits*, Geological Society of America, U.S.A, 1991.
25. Cox, R, Lowe, DR, Cullers, RL. The influence of sediment recycling and basement composition on evolution of mudrock chemistry in the southwestern United States. *Geochimica et Cosmochimica Acta* 59 (1995) 2919-2940.

N-Dimensional Solutions of Klein-Gordon Particles for Scaled Molecular Potential via Highly-Accurate Approximation

Hasan Fatih Kisoglu 

Mersin University, Department of Basic Sciences, Mersin, Turkey

ABSTRACT

The energy eigenvalues and eigenfunctions of relativistic scalar particles are obtained for an equal vector and scalar symmetrical molecular potential in N-dimensional euclidean space by using Asymptotic Iteration Method. For such a calculation, the potential in the eigenvalue equation is scaled regarding to fact that the potential is the same in non-relativistic limit. Furthermore, an highly-accurate approximation scheme is used to deal with the centrifugal term in the eigenvalue equation. The results obtained are compared with the ones that exist in literature.

Article History:

Received: 2017/07/19

Accepted: 2017/10/20

Online: 2018/04/06

Correspondence to: Hasan Fatih Kışoğlu
Mersin University, Faculty of Maritime,
Department of Basic Sciences, Mezitli,
Mersin Turkey

Tel: +90 324 482 5278/1162

Fax: +90 324 482 5496

E-Mail: hasanfatihk@mersin.edu.tr

Keywords: Klein-Gordon equation, Asymptotic Iteration Method, Symmetrical molecular potential, Centrifugal term

INTRODUCTION

Motion of scalar (i.e. spinless) particles in quantum mechanics is investigated by solving Klein-Gordon equation (relativistic case) or Schrödinger equation (non-relativistic case) for the interaction in system [1, 2]. This interaction is represented by a potential function which is crucial for solving the eigenvalue equation, since it acts a part to determine the solving technique.

The hyperbolic type molecular potential (or symmetrical well potential) [3] is one of the attractive potentials, and it represents some interactions in atomic and molecular levels. After Buyukkilic and friends introduced the potential and obtained one dimensional non-relativistic solutions in Ref.[3], many papers in which various solving methods are used, have been come out in the last decade. For instance, in Ref.[4], Yang has generalized the symmetrical well potential to the deformed one by way of the deformed hyperbolic functions [5]. In Ref.[6], exact solutions of relativistic cases have been obtained for $l=0$ states. Furthermore, Refs. [7, 8] can be adduced for using different solving methods to investigate the symmetrical well potential.

Recently, Candemir[9] has tackled Klein-Gordon equation in spherical-coordinates, for equal vector and scalar symmetrical well potential. She has obtained the solutions for $l=0$ states by using Nikiforov-Uvarov (NU) method[10]. She has also used Green-Aldrich

approximation[11] to cope with the centrifugal term in the eigenvalue equation.

In this paper, the solutions of Klein-Gordon equation for equal vector and scalar symmetrical well potential is obtained in N-dimensional euclidean space. For the calculations, Asymptotic Iteration Method (AIM)[12, 13, 14] is used. Furthermore, an approximation scheme, which is more precise than Green-Aldrich approximation, is also used to eliminate the centrifugal term[15, 16]. Besides these, the potential is scaled considering that it should be the same in non-relativistic limit.

Organization of the paper is as follows: stationary Klein-Gordon equation for any equal vector and scalar potential is summarized in Section 2. Section 3 outlines AIM while it is used for obtaining the energy eigenvalues and eigenfunctions of Klein-Gordon equation for the symmetrical well potential in Section 4. The results are sums up in Section 5.

KLEIN-GORDON EQUATION FOR EQUAL VECTOR AND SCALAR POTENTIAL

Stationary (i.e. time-independent) Klein-Gordon equation for a potential that consists of vector and scalar components is given as follows ($\hbar = c = 1$)

$$\left[\bar{\nabla}^2 + (V(\vec{r}) - \varepsilon)^2 - (S(\vec{r}) + m_0)^2 \right] \psi(\vec{r}) = 0 \quad (1)$$

where ε is relativistic energy, m_0 is rest mass, $S(\vec{r})$ and $V(\vec{r})$ are position-dependent scalar and vector potentials, respectively. In the case of $S(\vec{r}) = \pm V(\vec{r})$, Eq.(1) turns into

$$\left[\bar{\nabla}^2 - 2(\varepsilon \pm m_0)V(\vec{r}) + \varepsilon^2 - m_0^2 \right] \psi(\vec{r}) = 0 \quad (2)$$

This equation is written in relativistic limit and, in general, stands for scalar particles. So, it is Klein-Gordon equation for the potential $V(\vec{r})$. Besides, it should give Schrödinger equation for the same potential in non-relativistic limit as mentioned by Alhaidari et al. in Ref.[17]. In case of $S(\vec{r}) = +V(\vec{r})$, non-relativistic limit of Eq.(2), in which $\varepsilon - m_0 \approx E$ (E is non-relativistic energy and $|E| \ll m_0$), is yielded as

$$\left[\frac{\nabla^2}{2m_0} - 2V(\vec{r}) + E \right] \psi(\vec{r}) = 0 \quad (3)$$

This is Schrödinger equation for the potential $2V(\vec{r})$, not $V(\vec{r})$. Thus, one can scale the potentials in Eq.(1) as[17, 18]

$$\left[\bar{\nabla}^2 + \left(\frac{1}{2}V(\vec{r}) - \varepsilon \right)^2 - \left(\frac{1}{2}S(\vec{r}) + m_0 \right)^2 \right] \psi(\vec{r}) = 0 \quad (4)$$

As for the case of $S(\vec{r}) = +V(\vec{r})$, it can be written as

$$\left[\bar{\nabla}^2 - (\varepsilon + m_0)V(\vec{r}) + \varepsilon^2 - m_0^2 \right] \psi(\vec{r}) = 0 \quad (5)$$

and this gives Schrödinger equation for the potential $V(\vec{r})$, in non-relativistic limit.

A SUMMARY OF ASYMPTOTIC ITERATION METHOD (AIM)

Asymptotic Iteration Method (AIM)[12] has been studied out as an alternative solution technique for, in general, second order linear differential equations given as

$$f''(z) = \Lambda_0(z)f'(z) + \sigma_0(z)f(z) \quad (6)$$

where $\Lambda_0(z)$ and $\sigma_0(z)$ functions are in C^∞ . The general solution of (6) is as follows (S_1 and S_2 are invariants)

$$f(z) = \exp\left(-\int \mu(t) dt\right) \times \left[S_2 + S_1 \int \exp\left(\int (\Lambda_0(\tau) + 2\mu(\tau)) d\tau\right) dt \right] \quad (7)$$

in prospect of

$$\frac{\sigma_n}{\sigma_{n-1}} = \frac{\Lambda_n}{\Lambda_{n-1}} \equiv \mu \quad (8)$$

where $n > 0$ ($n \in \mathbb{Z}$) and

$$\Lambda_n = \Lambda'_{n-1} + \sigma_{n-1} + \Lambda_0 \Lambda_{n-1}, \quad \sigma_n = \sigma'_{n-1} + \sigma_0 \Lambda_{n-1} \quad (9)$$

The functions Λ_0 and σ_0 contain the, E_n , (unknown) energy eigenvalues when AIM is used in quantum mechanics in mathematical physics. These eigenvalues are obtained from the following equation

$$\begin{aligned} \Delta_n(z, E) &\equiv \sigma_n(z, E)\Lambda_{n-1}(z, E) \\ &- \Lambda_n(z, E)\sigma_{n-1}(z, E) = 0 \end{aligned} \quad (10)$$

reached by the medium of Eq.(8). The eigenvalue problem is said to be "exactly solvable", if Eq.(10) depends upon only (unknown) E eigenvalues. In this case, an E_n energy eigenvalue is achieved after n iterations[19, 20, 21]. If Eq. (10) is also dependent on the variable z , the energy eigenvalues are obtained approximately. Then, a suitable $z \approx z_0$ value should be determined for initiation of the AIM iterations[22, 23, 24].

As for obtaining the eigenfunctions of eigenvalue problem, following function generator is used in the view of AIM

$$f_n(z) = S_2 \exp\left(-\int \frac{\sigma_n(t)}{\Lambda_n(t)} dt\right) \quad (11)$$

THE SOLUTIONS OF KLEIN-GORDON EQUATION

In this section, the eigenvalues and eigenfunctions of Klein-Gordon equation for the symmetrical well potential is obtained in N -dimensional euclidean space. For the calculations, AIM is used.

The stationary Klein-Gordon equation for equal scalar ($S(\vec{r})$) and vector ($V(\vec{r})$) potentials is given as in Eq.(5)

$$\left[\bar{\nabla}^2 - (\varepsilon + m_0)V(\vec{r}) + \varepsilon^2 - m_0^2 \right] \psi(\vec{r}) = 0$$

For N-dimensional euclidean space, $\psi(\vec{r})$ is taken as

$$\psi(\vec{r}) = r^{-\frac{(N-1)}{2}} u(r) Y_{l_1, l_2, \dots, l_{N-1}}(\varphi_1, \varphi_2, \dots, \varphi_{N-1}) \quad (12)$$

where $Y_{l_1, l_2, \dots, l_{N-1}}(\varphi_1, \varphi_2, \dots, \varphi_{N-1})$ are hyperspherical harmonics and l_1, l_2, \dots, l_{N-1} are angular momentum quantum numbers [25, 26, 27, 28, 29]. For spherical coordinates ($N = 3$), e.g., $l_{N-2} \equiv m$ and $l_{N-1} \equiv l$, while φ_{N-2} and φ_{N-1} are azimuthal and polar angles, respectively. Thus, for simpleness, the quantum number l_{N-1} is abbreviated such as $l_{N-1} \equiv l$ from now on.

Being $r \in (0, \infty)$, the radial Klein-Gordon equation in N-dimensions can be written as

$$\frac{d^2 u(r)}{dr^2} + \left[(\varepsilon^2 - m_0^2) - (\varepsilon + m_0)V(r) - \frac{\gamma(\gamma+1)}{r^2} \right] u(r) = 0 \quad (13)$$

by using Eq.(12), where $\gamma = l + \frac{N-3}{2}$ and $V(r)$ is the central potential of system.

As an attractive potential function, equal vector and scalar symmetrical well potential is given as

$$S(r) = V(r) = V_1 \left(\frac{e^{\alpha r} - e^{-\alpha r}}{e^{\alpha r} + e^{-\alpha r}} \right)^2 + V_2 \left(\frac{2}{e^{\alpha r} + e^{-\alpha r}} \right)^2 \quad (14)$$

where V_1 , V_2 and α are arbitrary constants. The form of the symmetrical well potential for a few α values can be seen in Fig.1

For the potential in Eq.(14), Klein-Gordon equation which is given in Eq.(13) is written as

$$\frac{d^2 u(r)}{dr^2} + \left\{ \begin{array}{l} (\varepsilon^2 - m_0^2) - (\varepsilon + m_0) \times \\ V_1 \left(\frac{e^{\alpha r} - e^{-\alpha r}}{e^{\alpha r} + e^{-\alpha r}} \right)^2 + \\ V_2 \left(\frac{2}{e^{\alpha r} + e^{-\alpha r}} \right)^2 \\ - \frac{\gamma(\gamma+1)}{r^2} \end{array} \right\} u(r) = 0$$

In this equation an approximation scheme is used to deal with the, $\gamma(\gamma+1)/r^2$, centrifugal term. For this purpose, following approximation can be used [15]

$$\frac{1}{r^2} \approx 4\alpha^2 \left[C_0 + C_1 \left(\frac{e^{\alpha r}}{e^{2\alpha r} - 1} \right)^2 \right] \quad (16)$$

where the constants C_0 and C_1 are as follow

$$C_1 = \frac{(e^{2\alpha} - 1)^3}{4\alpha^3 e^{2\alpha} (e^{2\alpha} + 1)}, \quad C_0 = \frac{1}{4\alpha^2} - C_1 \frac{e^{2\alpha}}{(e^{2\alpha} - 1)^2} \quad (17)$$

As is seen in Fig. 2, the approximation in Eq.(16) is too close to the $1/r^2$ for either small or large values of the α [16].

Eq.(15) can be turned into the following equation by defining a new variable such as $x = \left(\frac{e^{\alpha r} - e^{-\alpha r}}{e^{\alpha r} + e^{-\alpha r}} \right)^2$ and using the approximation scheme given in Eq.(16)

$$\frac{d^2 u(x)}{dx^2} + \left(\frac{1}{2x} - \frac{1}{1-x} \right) \frac{du(x)}{dx} + \left(\frac{A}{x^2} + \frac{B}{(1-x)^2} + \frac{D}{x(1-x)} \right) u(x) = 0 \quad (18)$$

where $x \in (0,1)$ and

$$A = -\kappa_1, \quad B = -\kappa_1 + \kappa_2 - \kappa_3, \quad D = -2\kappa_1 + \kappa_2 \quad (19)$$

The constants κ_1 , κ_2 and κ_3 are as below

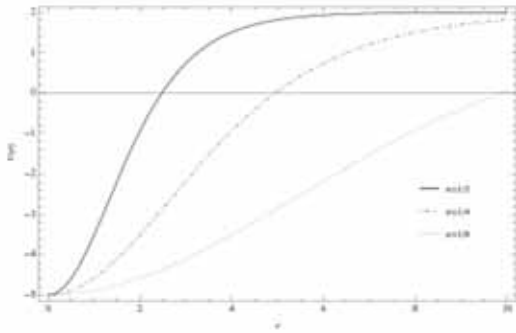


Figure 1. Shape of the symmetrical well potential for $V_1 = 2$, $V_2 = 5$, and $\alpha = 0.5, 0.25, 0.125$. The α determines the range of the potential well and V_1, V_2 specify the well depth

$$\begin{aligned} \kappa_1 &= C_1 \frac{\gamma(\gamma+1)}{4} \\ \kappa_2 &= -C_0 \gamma(\gamma+1) + C_1 \frac{\gamma(\gamma+1)}{4} + \frac{(\varepsilon + m_0)}{4\alpha^2} V_2 \\ &\quad + \frac{(\varepsilon^2 - m_0^2)}{4\alpha^2} \\ \kappa_3 &= \frac{(\varepsilon + m_0)}{4\alpha^2} (V_1 + V_2) \end{aligned} \quad (20)$$

Regarding to the boundary conditions of the system, one can assume (unnormalized) $u(x)$ in Eq.(18) as follows

$$u(x) = x^{\frac{1}{4} + \sqrt{\frac{1}{16} + \kappa_1}} (1-x)^{\sqrt{\kappa_1 + \kappa_3 - \kappa_2}} g(x) \quad (21)$$

where $g(x)$ is the function to be determined by AIM. If $u(x)$, given by Eq.(21), is substituted in Eq.(18) following equation is obtained

$$\begin{aligned} \frac{d^2 g(x)}{dx^2} + \left[\frac{\left(2\rho + \frac{5}{2}\right)}{x} - \frac{(2\beta + 3)}{1-x} \right] \frac{dg(x)}{dx} \\ - \left[\frac{\left(2\rho + \frac{5}{2}\right)(\beta + 1)}{x(1-x)} - \frac{D - (\rho + 1)}{x(1-x)} \right] g(x) = 0 \end{aligned} \quad (22)$$

where

$$\rho = -\frac{3}{4} + \sqrt{\frac{1}{16} + \kappa_1}, \quad \beta = -1 - \sqrt{\kappa_1 + \kappa_3 - \kappa_2}$$

Eq.(22) is in AIM form, and the iterations can be initiated using the following functions, in keeping with Eq.(6)

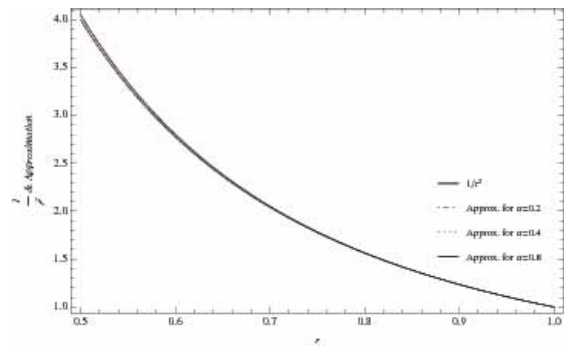


Figure 2. Comparison of the $1/r^2$ centrifugal term and the approximation scheme. The approximation is too close to (even overlapped) the centrifugal term for either small or large values of the α

$$\begin{aligned} \Lambda_0(x) &= - \left[\frac{\left(2\rho + \frac{5}{2}\right)}{x} - \frac{(2\beta + 3)}{1-x} \right], \\ \sigma_0(x) &= \left[\frac{\left(2\rho + \frac{5}{2}\right)(\beta + 1)}{x(1-x)} - \frac{D - (\rho + 1)}{x(1-x)} \right] \end{aligned} \quad (24)$$

The first-four iterations give the D as

$$D_0 = \frac{1}{2}(7 + 5\beta + 6\rho + 4\beta\rho),$$

$$D_1 = \frac{1}{2}(18 + 9\beta + 10\rho + 4\beta\rho)$$

$$D_2 = \frac{1}{2}(33 + 13\beta + 14\rho + 4\beta\rho),$$

$$D_3 = \frac{1}{2}(52 + 17\beta + 18\rho + 4\beta\rho)$$

So, one can generalize the D as below

$$D_n = \frac{1}{2} \left[\frac{(2n^2 + 9n + 7) + (4n + 5)\beta}{(4n + 6)\rho + 4\beta\rho} \right] \quad (25)$$

where $n = 0, 1, 2, 3, \dots$

Using Eqs.(25) and (??), the energy eigenvalues can be obtained analytically from the equation given below

$$\begin{aligned} n(n+1) + 2n \left(\sqrt{\frac{1}{16} + \kappa_1} - \sqrt{\kappa_1 + \kappa_3 - \kappa_2} \right) \\ - 2 \sqrt{\frac{1}{16} + \kappa_1} (\kappa_1 + \kappa_3 - \kappa_2) \\ + \sqrt{\frac{1}{16} + \kappa_1} - \sqrt{\kappa_1 + \kappa_3 - \kappa_2} + 2\kappa_1 - \kappa_2 + \frac{1}{4} = 0 \end{aligned} \quad (26)$$

Some numeric values of the energy eigenvalues for $V_1 = 3, V_2 = 10, m_0 = 1$ and $\alpha = 0.125$ is given in Table 1.

Besides, comparison of the energy eigenvalues which have been calculated from Ref.[9] with the ones obtained for $N = 3$ dimensions in present study is given in Table 2.

As mentioned in Section 3, eigenfunctions of the problem is achieved through the, $g_n(x) = \exp\left(-\int \frac{\sigma_n(t)}{\Lambda_n(t)} dt\right)$, function generator. For this purpose, and functions in Eq.(24) are used.

Regarding to the first-four AIM iterations, outcomes given below are obtained for the function generator

$$g_0(x) = 1$$

$$g_1(x) = -(4\rho + 5) \left\{ 1 - \frac{[4(\beta + \rho) + 11]x}{(4\rho + 5)} \right\}$$

$$g_2(x) = (4\rho + 5) \times \left\{ \begin{aligned} &1 - \frac{2[4(\beta + \rho) + 13]x}{(4\rho + 5)} \\ &+ \frac{2[4(\beta + \rho) + 13][4(\beta + \rho) + 15]x^2}{(4\rho + 5)(4\rho + 7)2!} \end{aligned} \right\}$$

$$g_3(x) = -(4\rho + 5)(4\rho + 7)(4\rho + 9)$$

$$\times \left\{ \begin{aligned} &1 - \frac{3[4(\beta + \rho) + 15]x}{(4\rho + 5)} \\ &+ \frac{6[4(\beta + \rho) + 15][4(\beta + \rho) + 17]x^2}{(4\rho + 5)(4\rho + 7)2!} \\ &- \frac{6[4(\beta + \rho) + 15][4(\beta + \rho) + 17][4(\beta + \rho) + 19]x^3}{(4\rho + 5)(4\rho + 7)(4\rho + 9)3!} \end{aligned} \right\}$$

Accordingly, the $g_n(x)$ function generator can be obtained as

$$g_{n,\beta,\rho}(x) = (-1)^n \left\{ \prod_{s=1}^n (4\rho + 2s + 3) \right\} \times \left\{ \sum_{\mu=0}^n \frac{(-n)_\mu [4(\beta + \rho) + 2n + 9]_{\mu,2} x^\mu}{(4\rho + 5)_{\mu,2} \mu!} \right\} \quad (27)$$

where $n = 0, 1, 2, 3, \dots$ and

$$(a)_{d,k} = a(a+k)(a+2k)(a+3k)\dots(a+(d-1)k) \quad (28)$$

is k-Pochhammer symbol ($k \in \mathbb{R}$ and $d \in \mathbb{N}^+$) [30, 31].

If the following relation between Pochhammer symbol and k-Pochhammer symbol is used

Table 1. Numeric values of the E_n energy eigenvalues for $V_1 = 3, V_2 = 10, m_0 = 1$ and $\alpha = 0.125$, and for $N = 3, 6, 9$ dimensions. E'_n represents the energy eigenvalues of antiparticle. The principle quantum number of an energy level is $(n + l + 1)$.

N	Energy level	E_n	E'_n
3	1s	-0.982158	-0.999150
	2s	-0.901930	-0.994573
	2p	-0.946310	-0.998056
	4p	-0.680055	-0.981598
	4d	-0.757918	-0.988561
	5d	-0.581474	-0.976690
6	6d	-0.375575	-0.961079
	6f	-0.473204	-0.971551
	1s	-0.921555	-0.997383
	2s	-0.799418	-0.990154
	2p	-0.859335	-0.995781
	4p	-0.528440	-0.974152
9	4d	-0.614897	-0.983350
	5d	-0.415974	-0.968884
	6d	-0.195785	-0.950587
	6f	-0.296301	-0.963340
	1s	-0.822311	-0.994852
	2s	-0.665414	-0.985163
9	2p	-0.737623	-0.992735
	4p	-0.356946	-0.966148
	4d	-0.449066	-0.977435
	5d	-0.234210	-0.960458
	6d	-0.004814	-0.939539
	6f	-0.106303	-0.954464

$$(a)_{d,k} = k^d \left(\frac{a}{k} \right)_d \quad (29)$$

one can write the $g_n(x)$ as

$$g_{n,\beta,\rho}(x) = (-1)^n \left\{ \prod_{s=1}^n (4\rho + 2s + 3) \right\}_2 \times {}_2F_1 \left(-n, \frac{4(\beta + \rho) + 2n + 9}{2}; \frac{4\rho + 5}{2}; x \right) \quad (30)$$

where ${}_2F_1(a, b; c; x)$ is the hypergeometric function.

So, the unnormalized $u_n(x)$, given in Eq.(21), is got as follows

$$u_n(x) = (-1)^n \xi_n x^{\frac{1}{4} + \sqrt{\frac{1}{16} + \kappa_1}} (1-x)^{\sqrt{\kappa_1 + \kappa_3 - \kappa_2}} \left\{ \prod_{s=1}^n (4\rho + 2s + 3) \right\} \quad (31)$$

$$\times {}_2F_1\left(-n, \frac{4(\beta + \rho) + 2n + 9}{2}; \frac{4\rho + 5}{2}; x\right)$$

where ξ_n is normalization constant, and ρ and β is given as Eq.(23).

Table 2. Comparison of the E_n energy eigenvalues calculated from Ref.[9] with the ones of present study in spherical coordinates ($N = 3$) for $V_1 = 3$, $V_2 = 10$, $m_0 = 1$ and $\alpha = 0.125$. E'_n represents the antiparticle's energy.

Energy level	E_n	E_n from Ref.[9]	E'_n	E'_n from Ref.[9]
1s	-0.982158	-0.993527	-0.999150	-0.999535
2s	-0.901930	-0.963422	-0.994573	-0.997050
2p	-0.946310	-0.981451	-0.998056	-0.998542
4p	-0.680055	-0.874758	-0.981598	-0.989587
4d	-0.757918	-0.909933	-0.988561	-0.992573
5d	-0.581474	-0.834196	-0.976690	-0.986102
6d	-0.375575	-0.737735	-0.961079	-0.977635
6f	-0.473204	-0.788449	-0.971551	-0.982119

CONCLUSION

In quantum mechanics, a physical system undergone a potential is investigated by obtaining the energy eigenvalues and eigenfunctions. This goal is achieved via several mathematical methods. Asymptotic Iteration Method (AIM)[12] is one of the methods widely used. It has some advantages such that it can be applied to both exactly and approximately (numerically) solvable problems. It is also used to obtain perturbative eigenvalues and eigenfunctions besides the non-perturbative usage[13, 32, 33].

In present study, a system which is under the influence of a hyperbolic type molecular potential (or symmetrical well potential)[3] is probed. By using this potential, one can obtain the reflectionless potential and a particular case of hyperbolic type molecular potential which has a relation with three-dimensional harmonic oscillator [9, 34, 35]. The eigenvalues and eigenfunctions of Klein-Gordon equation

have been obtained using AIM. Results have been obtained for n -dimensional euclidean space. An highly-accurate approximation scheme[15, 16] has been also used to deal with the centrifugal term. Furthermore, potential term in the Klein-Gordon equation has been scaled taking the consideration that the potential should be the same in non-relativistic limit, i.e. Schrödinger equation[17, 18]. For the calculations, the case of equal vector and scalar symmetrical well potential has been considered.

The results achieved have also been compared with the ones calculated from Ref.[9]. It has been seen that the energy eigenvalues are greater than those of Ref.[9] in which calculations have been made in spherical coordinates and Green-Aldrich approximation[11] has been used to eliminate the centrifugal term (see in Table 2). This difference becomes more clear especially for higher quantum levels. One reason for such a conclusion can be resulted from that the eigenvalues have been obtained for the symmetrical well potential, let's say $V(r)$, in present study whereas the eigenvalues have been resulted for $V(r)$ in Ref.[9]. So, in present study, it is more likely to be free-particle system.

Besides, accuracy of the approximation scheme used can be illuminated by Eq.(17) (also seen in Fig.2). According to this equation, C_0 and C_1 constants are also dependent upon the α arbitrary parameter. So, they correspondingly change in any variation of the α .

REFERENCES

- Greiner, W. Relativistic Quantum Mechanics, third ed. Springer, Berlin, 2000.
- Landau, L. D., Lifshitz, E. M. Quantum Mechanics Non-Relativistic Theory, second ed. Pergamon, London, 1965.
- Buyukkilic, F., Egrifis, H., Demirhan, D. Solution of the Schrödinger equation for two different molecular potentials by the Nikiforov-Uvarov method. Theor. Chem. Acc. 98 (1997) 192-196.
- Yang, Q. B. Deformed Symmetrical Double-well Potential. Acta. Photon. Sin. 32 (2003) 882-884.
- Arai, A. Exactly solvable supersymmetric quantum mechanics. J. Math. Anal. Appl. 158 (1991) 63-79.
- Zhao, X. Q., Jia, C. S., Yang, Q. B. Bound states of relativistic particles in the generalized symmetrical double-well potential. Phys. Lett. A 337 (2005) 189-196.
- Wei, G. F., Chen, W. L. Arbitrary l-wave bound states of the Schrödinger equation for the hyperbolic molecular potential. Int. J. Quantum Chem. 114 (2014), 1602-1606.
- Wei, G. F., Chen, W. L., Dong, S. H. The arbitrary l continuum states of the hyperbolic molecular potential. Phys. Lett. A 378 (2014) 2367-2370.
- Candemir, N. Klein-Gordon particles in symmetrical well potential. Appl. Math. Comput. 274 (2016) 531-538.
- Nikiforov, A.F., Uvarov, V.B. Special functions of mathematical physics: a unified introduction with applications, first ed.

- Birkhäuser, 1988.
11. Greene, R.L., Aldrich, C. Variational wave functions for a screened Coulomb potential. *Phys. Rev. A* 14 (1976) 2363-2366.
 12. Ciftci, H., Hall, R.L., Saad, N. Asymptotic iteration method for eigenvalue problems. *J. Phys. A: Math. Gen.* 36 (2003) 11807-11816.
 13. Ciftci, H., Hall, R.L., Saad, N. Perturbation theory in a framework of iteration methods. *Phys. Lett. A* 340 (2005) 388-396.
 14. Ciftci, H., Hall, R.L., Saad, N. Exact and approximate solutions of Schrödinger's equation for a class of trigonometric potentials. *Centr. Eur. J. Phys.* 11 (2013) 37-48.
 15. Ikhdair, S.M. An improved approximation scheme for the centrifugal term and the Hulthén potential. *Eur. Phys. J. A* 39 (2009) 307-314.
 16. Aydogdu, O., Yanar, H. Bound and scattering states for a hyperbolic-type potential in view of a new developed approximation. *Int. J. Quantum Chem.* 115 (2015) 529-534.
 17. Alhaidari, A.D., Bahlouli, H., Al-Hasan, A. Dirac and Klein-Gordon equations with equal scalar and vector potentials. *Phys. Lett. A* 349 (2006) 87-97.
 18. Yasuk, F., Durmus, A., Boztosun, I. Exact analytical solution to the relativistic Klein-Gordon equation with noncentral equal scalar and vector potentials. *J. Math. Phys.* 47 (2006) 082302.
 19. Ciftci, H., Hall, R.L., Saad, N. Construction of exact solutions to eigenvalue problems by the asymptotic iteration method. *J. Phys. A: Math. Gen.* 38 (2005) 1147-1156.
 20. Ol ar, E., Koç, R., Tütüncüler, H. The exact solution of the s-wave Klein-Gordon equation for the generalized Hulthén potential by the asymptotic iteration method. *Phys. Scr.* 78 (2008) 015011.
 21. Alsadi, K.S. Exact Solutions of Dirac-Rosen-Morse Problem via Asymptotic Iteration Method. *J. Nanoelectron. Optoe.* 10 (2015) 683-687.
 22. Hall, R.L., Saad, N. Schrödinger spectrum generated by the Cornell potential. *Open Phys.* 13 (2015) 83-89.
 23. Fernandez, F.M. On an iteration method for eigenvalue problems. *J. Phys. A: Math. Gen.* 37 (2004) 6173-6180.
 24. Barakat, T., Al-Dossary, O.M. The Asymptotic Iteration Method For The Eigenenergies Of The Asymmetrical Quantum Anharmonic Oscillator Potentials. *Int. J. Mod. Phys. A* 22 (2007) 203-212.
 25. Nieto, M. M. Hydrogen atom and relativistic pi-mesic atom in N-space dimensions. *Am. J. Phys.* 47 (1979) 1067-1072.
 26. Avery, J. *Hyperspherical Harmonics: Applications in Quantum Theory*, first ed. Kluwer Academic Publishers, 1989.
 27. Cavalli, S., Aquilanti, V., Grossi, G. Hyperspherical coordinates for molecular dynamics by the method of trees and the mapping of potential energy surfaces for triatomic systems. *J. Chem. Phys.* 85 (1986) 1362-1375.
 28. Nouri, S. Generalized coherent states for the d-dimensional Coulomb problem. *Phys. Rev. A* 60 (1999) 1702-1705.
 29. Avery, J. *Hyperspherical Harmonics and Generalized Sturmians*, first ed. Kluwer Academic Publishers, 2002.
 30. Diaz, R., Pariguan, E. On hypergeometric functions and Pochhammer k-symbol. *Divulg. Mat.* 15 (2007) 179-192.
 31. Mubeen, S., Rehman, A. A Note on k-Gamma Function and Pochhammer k-Symbol. *Journal of Informatics and Mathematical Sciences* 6 (2014) 93-107.
 32. Ciftci, H., Kisoglu, H.F. Application of asymptotic iteration method to a deformed well problem. *Chinese Phys. B* 25 (2016) 030201.
 33. Kisoglu, H.F., Ciftci, H. Accidental Degeneracies in N dimensions for Potential Class via Asymptotic Iteration Method (AIM). *Commun. Theor. Phys.* 67 (2017) 350-354.
 34. Kiriushcheva, N., Kuzmin, S. Scattering of a Gaussian wave packet by a reflectionless potential. *Am. J. Phys* 66 (1998) 867-872.
 35. Qiang, W.-C. Bound states of the Klein-Gordon and Dirac equations for potential . *Chin. Phys.* 13 (2004) 571.

A New Perspective On Soft Topology

Mustafa Burç KANDEMİR 

Muğla Sıtkı Koçman University, Department of Mathematics, Muğla, Turkey.

ABSTRACT

In this paper, we approach the concept of soft topology with a different perspective. We define a soft topological space over given initial topological universe as a parameterization of subspaces of a topological space. In addition to this, we define some basic topological concepts such as Hausdorffness, compactness, connectedness for soft topological spaces and study their some properties. We give some results for relations between a topological space and a soft topological space that is defined on it.

Keywords:

Soft set; Soft topological space; Hausdorffness; Compactness; Connectedness

INTRODUCTION AND PRELIMINARIES

Almost every branch of science has its own uncertainties and ambiguities. These uncertainties depend on the existence of many parameters. So it is not always easy to model a daily life problem mathematically using classical mathematical methods. In this sense, mankind has gone to find new mathematical models. In 1999, Molodtsov [1] established the soft set theory to model uncertainties in any phenomenon. He defined the concept of soft set as follows;

Definition 1.1.

[1] Let U be an initial universe, E be a parameters set. The pair (F, A) is called a soft set over U such that $F: A \rightarrow P(U)$ is a set-valued function where $A \subseteq E$ and $P(U)$ is the power set of U .

In fact a soft set on an initial universe is nothing more than the parameterization of some subsets of the universe.

The family of all soft sets over the initial universe U with respect to the parameters set E is denoted by $S(U, E)$.

Set-theoretic operations for soft sets given by Maji et al. and Ali et al. in [2, 3]. The operations between two soft sets such as soft union, soft intersection, soft complement etc. defined in [2, 3] as follows.

Definition 1.2.

[2, 3] Let (F, A) and (G, B) be soft sets over U where $A, B \subseteq E$. We say that (F, A) is a soft subset of (G, B) if $A \subseteq B$ and $F(p) \subseteq G(p)$ for each $p \in A$, and denoted by $(F, A) \widetilde{\subseteq} (G, B)$.

Definition 1.3.

[2, 3] Let (F, A) and (G, B) be soft sets over U where $A, B \subseteq E$. Soft union of (F, A) and (G, B) is a soft set (H, C) over U such that

$$H(p) = \begin{cases} F(p) & , \text{if } p \in A - B \\ G(p) & , \text{if } p \in B - A \\ F(p) \cup G(p) & , \text{if } p \in A \cap B \end{cases} \quad (1)$$

for each $p \in C$ where $C = A \cup B$. It is denoted by $(F, A) \widetilde{\cup} (G, B) = (H, C)$.

Soft intersection of (F, A) and (G, B) is a soft set (H, C) over U such that $H(p) = F(p) \cap G(p)$ for each $p \in C$ where $C = A \cap B$. It is denoted by $(F, A) \widetilde{\cap} (G, B) = (H, C)$.

Article History:

Received: 2017/07/19

Accepted: 2017/10/17

Online: 2018/04/06

Correspondence to: Mustafa Burç Kandemir, Muğla Sıtkı Koçman University, Department of Mathematics, 48000, Muğla, Turkey, E-Mail: hbkandemir@mu.edu.tr

Definition 1.4.

[2, 3] Let (F, A) be a soft set over U . If $F(p) = \emptyset$ for each $p \in A$, we call that (F, A) is a relative null soft set and denoted by $\tilde{\Phi}$. Besides, if $F(p) = U$ for each $p \in A$, then we call that (F, A) is a relative whole soft set and denoted by \tilde{U}_A . We note that (F, E) is called absolute soft set if $F(p) = U$ for all $p \in E$.

“And” and “Or” operations between soft sets are defined since an element in the universal set may have more than one property or an attribute. Hence, their definitions are given below.

Definition 1.5.

[2, 3] $(F, A) \text{Or} (G, B) = (H, A \times B)$ is defined by $H(p_1, p_2) = F(p_1) \cup G(p_2)$ for all $(p_1, p_2) \in A \times B$. In a similar manner, $(F, A) \text{And} (G, B) = (H, A \times B)$ is defined by $H(p_1, p_2) = F(p_1) \cap G(p_2)$ for all $(p_1, p_2) \in A \times B$.

Definition 1.6.

[2, 3] The complement of a soft set (F, A) is defined as $(F, A)^c = (F^c, A)$ where $F^c : A \rightarrow P(U)$ is a mapping given by $F^c(p) = U - F(p)$ for each $p \in A$.

The concept of Cartesian product introduced by Babit-ha et al. in [4].

Definition 1.7.

[4] The Cartesian product of the soft sets (F, A) and (G, B) is defined as $(F, A) \times (G, B) = (H, A \times B)$ where $H : A \times B \rightarrow P(U \times U)$ and $H(p_1, p_2) = F(p_1) \times G(p_2)$ for each $(p_1, p_2) \in A \times B$.

Kim and Min defined the concept of full soft set as follows;

Definition 1.8.

[5] Let (F, A) be a soft set over U . (F, A) is called full soft set over U if the condition $\bigcup_{p \in A} F(p) = U$ is provided for each parameters in the parameter set A .

The concept of similarity between soft sets given by Min in [6].

Definition 1.9.

[6] Let (F, A) and (G, B) be soft sets over U . We call that (F, A) is similar to (G, B) if there exists a bijective function $\phi : A \rightarrow B$ such that $F(p) = (G \circ \phi)(p)$ for each $p \in A$. If (F, A) is similar to (G, B) , we denote by $(F, A) \cong (G, B)$.

Topology is one of the most important areas of mathematics. Main object of topology is the study of the general abstract nature of continuity or closeness on spaces. We refer readers to [7] and [8] for the basic definitions and properties for topological spaces. We can give the formal definition of topology defined in terms of set operations. Let U be a set and \mathfrak{T} be a family of some subsets of U . It is called that \mathfrak{T} is a topology on U if it satisfies following properties;

- U and \emptyset are in \mathfrak{T} .
- Whenever sets X and Y are in \mathfrak{T} , then so is $X \cap Y$.
- Whenever two or more sets are in \mathfrak{T} , then so is their union.

The pair (U, \mathfrak{T}) is called topological space. All members of \mathfrak{T} are called open sets. The set whose complement is open is called closed set [7, 8].

We can obtain new topological spaces using a given topological space via subset of a underlying set, and such topological space are called subspace. We can give this achievement method as in the following theorem.

Theorem 1.10.

[7, 8] Let (U, \mathfrak{T}) be a topological space and $X \subseteq U$. The family

$$\mathfrak{T}_X = \{X \cap O \mid O \in \mathfrak{T}\}$$

is a topology on X .

The topology \mathfrak{T} obtained in the above theorem is called subspace topology for $X \subseteq U$, and the pair (X, \mathfrak{T}_X) is called subspace of (U, \mathfrak{T}) .

Thus we gain the following result according to the definition of subspace.

Corollary 1.11.

[8] Let (U, \mathfrak{T}) be a topological space and (X, \mathfrak{T}_X) be a subspace of it. Then, $O_X \in \mathfrak{T}_X$ if and only if there exists

$O \in \mathfrak{T}$ such that $O_X = X \cap O$.

We will now define a new intersection and union concepts for two families of sets consisting of subsets of a set that we will use later.

Definition 1.12.

Let \mathfrak{X} and \mathfrak{Y} be two families of some subsets of the set U . The family

$$\mathfrak{X} \widehat{\cap} \mathfrak{Y} = \{X \cap Y \mid X \in \mathfrak{X}, Y \in \mathfrak{Y}\}$$

is called Cartesian intersection of the families \mathfrak{X} and \mathfrak{Y} . The family

$$\mathfrak{X} \widehat{\cup} \mathfrak{Y} = \{X \cup Y \mid X \in \mathfrak{X}, Y \in \mathfrak{Y}\}$$

is called Cartesian union of the families \mathfrak{X} and \mathfrak{Y} .

Example 1.13.

Let $U = \{a, b, c, d, e\}$ be a set, $\mathfrak{X} = \{\{a, b, d\}, \{c, e\}, \{d\}\}$ and $\mathfrak{Y} = \{\{a, e\}, \{d, e\}\}$ be families of some subsets of U . Then we obtain that

$$\mathfrak{X} \widehat{\cap} \mathfrak{Y} = \{\{a\}, \{d\}, \{e\}, \emptyset\}$$

from Definition 1.12. Moreover,

$$\mathfrak{X} \widehat{\cup} \mathfrak{Y} = \{\{a, b, d, e\}, \{a, c, e\}, \{c, d, e\}, \{a, d, e\}, \{d, e\}\}$$

We can give the following theorem for subspaces of a topological space by using Definition 1.12.

Theorem 1.14.

Let (U, \mathfrak{T}) be a topological space, (X, \mathfrak{T}_X) and (Y, \mathfrak{T}_Y) be subspaces of U . Then $\mathfrak{T}_{X \cap Y} = \mathfrak{T}_X \widehat{\cap} \mathfrak{T}_Y$.

Proof. Suppose that $O \in \mathfrak{T}_{X \cap Y}$. Then there exists $O' \in \mathfrak{T}$ such that $O = O' \cap (X \cap Y)$. So, we have

$$O = (O' \cap X) \cap (O' \cap Y)$$

and $O' \cap X \in \mathfrak{T}_X$ and $O' \cap Y \in \mathfrak{T}_Y$ where $O' \in \mathfrak{T}$. Therefore, $O \in \mathfrak{T}_X \widehat{\cap} \mathfrak{T}_Y$.

Conversely, let $O \in \mathfrak{T}_X \widehat{\cap} \mathfrak{T}_Y$. Then there exist $M \in \mathfrak{T}_X$ and $N \in \mathfrak{T}_Y$ such that $O = M \cap N$. Therefore, there exist $O_1, O_2 \in \mathfrak{T}$ such that $M = O_1 \cap X$ and $N = O_2 \cap Y$. At that case, we have

$$\begin{aligned} O &= M \cap N = (O_1 \cap X) \cap (O_2 \cap Y) \\ &= (O_1 \cap O_2) \cap (X \cap Y) \end{aligned}$$

Since $O_1 \cap O_2 \in \mathfrak{T}$, we obtain that $O \in \mathfrak{T}_{X \cap Y}$.

Hence, $\mathfrak{T}_{X \cap Y} = \mathfrak{T}_X \widehat{\cap} \mathfrak{T}_Y$.

We can give some basic topological properties of topological spaces and subspaces.

Let (U, \mathfrak{T}) be a topological space and \mathfrak{B} is a subfamily of \mathfrak{T} . We call that \mathfrak{B} is a base for the topology \mathfrak{T} if every open set in U is a union of sets from \mathfrak{B} . Let (U, \mathfrak{T}_U) and (V, \mathfrak{T}_V) be topological spaces and $\mathfrak{B}_U \subseteq \mathfrak{T}_U$ and $\mathfrak{B}_V \subseteq \mathfrak{T}_V$ are bases, respectively. It is called that the topological space which generated by the family

$$\mathfrak{B} = \{B_1 \times B_2 \mid B_1 \in \mathfrak{B}_U, B_2 \in \mathfrak{B}_V\}$$

is product space of the topological spaces (U, \mathfrak{T}) and (V, \mathfrak{T}_V) , and denoted by $(U \times V, \mathfrak{T}_U \times \mathfrak{T}_V)$ [7, 8]. We can give the following lemma for subspaces of product spaces.

Lemma 1.15.

[7, 8] If $X \subseteq U$ and $Y \subseteq V$ are subsets of topological spaces U and V , respectively, then product topology of the subspace topology on X and Y coincides subspace topology of the product topology on $U \times V$.

Let (U, \mathfrak{T}) be a topological space. If any two distinct points of (U, \mathfrak{T}) are given and there are distinct open neighborhoods that separate these points, this space is called Hausdorff space. We can give the following lemma for subspaces of Hausdorff space.

Lemma 1.16.

[7, 8] Each subspace of a Hausdorff space is Hausdorff.

Lemma 1.17.

[7, 8] The product space of two topological spaces is Hausdorff if and only if each one of topological spaces is Hausdorff.

Compactness is an important concept of a topological space. We can regard the concept of compactness in topological spaces as a generalization of the concept of boundedness in the space of real numbers \mathbb{R} . The notion of

compactness defined by the concept of open cover of given topological space. For given topological space (U, \mathfrak{T}) , consider the family $\{X_i | i \in I, X_i \subseteq U\}$. If $\bigcup_{i \in I} X_i = U$, then the family $\{X_i | i \in I, X_i \subseteq U\}$ is called cover for U. If each element of the family $\{X_i | i \in I, X_i \subseteq U\}$ is in \mathfrak{T} and the family is a cover, then the family $\{X_i | i \in I, X_i \subseteq U\}$ is called open cover for U. If the index set $J \subset I$ is finite and the family $\{X_i | i \in J, X_i \subseteq U\}$ is a cover for U, then the family $\{X_i | i \in J, X_i \subseteq U\}$ is called finite cover for U. If any subfamily of $\{X_i | i \in I, X_i \subseteq U\}$ is a cover for U then the subfamily is called subcover for U. So, the topological space (U, \mathfrak{T}) is called compact if all open cover of U has a finite subcover. Moreover, given any topological space (U, \mathfrak{T}) and $X \subset U$, if the subspace (X, \mathfrak{T}_X) is compact then X is called compact subset of the topological space (U, \mathfrak{T}) [7, 8].

Lemma 1.18.

[7, 8] All closed subsets of a compact space is compact.

Lemma 1.19.

[7, 8] Let (U, \mathfrak{T}) be a compact and Hausdorff topological space and $X \subset U$. X is compact if and only if X is closed.

Lemma 1.20.

[7, 8] Each compact subset of a Hausdorff space is closed.

Lemma 1.21 (Tychonoff).

[7, 8] If (U_i, \mathfrak{T}_i) are compact topological spaces for each $i \in I$, then so is $U = \prod_{i \in I} U_i$ which is endowed with the product topology.

Another important concept for topological spaces is the concept of connectedness. The definition of connectedness for a topological space is related to the fact that the space is a whole. In fact, the definition of connectedness of a topological space comes from the notion of separation of space into two or more parts. Let (U, \mathfrak{T}) be a topological space. A separation of U is a pair X and Y of disjoint nonempty open subsets of U whose union is U. The space U is said to be connected if there does not exist a separation of U. In other words, a topological space (U, \mathfrak{T}) is connected if

and only if the only subsets of U that are both open and closed in U are empty set and U itself. For given any subset X of a topological space (U, \mathfrak{T}) , if the subspace (X, \mathfrak{T}_X) is connected, then it is called that the subset X is connected in (U, \mathfrak{T}) [7, 8].

Lemma 1.22.

[7, 8] The family of non-disjoint connected subspaces of a topological space (U, \mathfrak{T}) is connected.

Of course, the principle of the notion of topology based on set theory. We define the specific properties of sets such as openness, closedness, compactness, connectedness etc. We can regard the soft set theory as an unusual set theory. So, there is a necessity to define the concept of soft topology on given initial universe or on a soft set. In 2011, Shabir and Naz [9] introduced soft topological space over an initial universe with a fixed set of parameters. This article is first published about soft topology and many basic properties were examined in this article by Shabir and Naz.

Definition 1.23.

[9] A soft topology τ on U is a family of soft sets over U if

- 1) $\tilde{\Phi}$ and \tilde{U}_E belong to τ ,
- 2) the union of any number of soft sets in τ belongs to τ ,
- 3) the intersection of any two soft sets in τ belongs to τ .

The triplet (U, τ, E) is called a soft topological space over U.

They gave following theorem in [9];

Theorem 1.24.

[9] Let (U, τ, E) be a soft topological space over U. Then the family

$$\tau_p = \{F(p) \mid (F, E) \in \tau\}, \forall p \in E$$

defines a topology on U.

Together with this theorem, they showed that soft topology is a parameterization of topologies defined on U. With this approach, they tried to capture the Molodtsov's sense. But Molodtsov's sense is the process of parameterizing the substructure of any given structure.

In this paper, we deal with this situation. In the next section, we redefine the concept soft topological space with respect to Molodtsov's sense.

RESULTS AND DISCUSSION

Soft Topology: A New Perspective

In this section, we look at the concept of soft topology from a new perspective. Molodtsov [1] defined a soft set over an initial universe as parameterization of some subsets of given initial universe as we mentioned in this previous section. Moreover, Aktas, et al. [10] defined the concept of a soft group over a group as parametrization of some subgroups of given group which is similar to Molodtsov's sense. Acar et al. [11] defined the concept of a soft ring over a ring as a parametrization of some subrings of given any ring which is similar to Molodtsov's sense, too. We use this notion, i.e. Molodtsov's sense, to redefine soft topology. We can give the definition as below.

Definition 2.1.

Let (U, \mathfrak{T}) be a topological space, E be a parameters set and (F, A) be a soft set over U where $A \subseteq E$. It is called that (F, A) is a soft topology over U if $(F(p), \mathfrak{T}_{F(p)})$ is a subspace of (U, \mathfrak{T}) for each $p \in A$. (F, A, \mathfrak{T}) is called a soft topological space over U .

Example 2.2.

Let $U = \{a, b, c, d\}$ and $\mathfrak{T} = \{\emptyset, U, \{a, b\}\}$, $E = \{1, 2, 3, 4, 5, 6\}$ and $(F, A) = \{1 = \{a, b\}, 4 = \{a\}\}$ where $\mathfrak{T}_{\{a, b\}} = \{\emptyset, \{a, b\}\}$, and $\mathfrak{T}_{\{a\}} = \{\emptyset, \{a\}\}$. We obtain that $(F(p), \mathfrak{T}_{F(p)})$ is a subspace of (U, \mathfrak{T}) for each $p \in \{1, 4\}$. Thus (F, A, \mathfrak{T}) is a soft topological space over U .

As it can be understood from Definition 2.1, a soft topological space is a parametrization of some subspaces of a topological space.

Theorem 2.3.

If (F, A, \mathfrak{T}) and (G, B, \mathfrak{T}) are soft topological space over (U, \mathfrak{T}) , then their intersection $(F, A, \mathfrak{T}) \widetilde{\cap} (G, B, \mathfrak{T})$ is a soft topological space over U where the intersection of all subspaces according to each parameter is the Cartesian intersection subspace topology on the intersection of subsets according to each parameters.

Proof. Suppose that $(F, A, \mathfrak{T}) \widetilde{\cap} (G, B, \mathfrak{T}) = (H, C, \mathfrak{T})$. We need to show that $(H(p), \mathfrak{T}_{H(p)})$ is a subspace of U for each $p \in C = A \cap B$. From the definition of soft intersection, we have that $H(p) = F(p) \cap G(p)$ for each $p \in C$. Obviously, we obtain that $\mathfrak{T}_{H(p)} = \mathfrak{T}_{F(p)} \widehat{\cap} \mathfrak{T}_{G(p)}$ for each $p \in C$ from Theorem 1.14. Thus, $(H(p), \mathfrak{T}_{H(p)})$ is a subspace of U for all $p \in C$. Hence, (H, C, \mathfrak{T}) is a soft topology over U .

Theorem 2.4.

If (F, A, \mathfrak{T}) and (G, B, \mathfrak{T}) are soft topological space over (U, \mathfrak{T}) , and $A \cap B = \emptyset$, then their union $(F, A, \mathfrak{T}) \widetilde{\cup} (G, B, \mathfrak{T})$ is a soft topological space over U .

Proof. Say that $(F, A, \mathfrak{T}) \widetilde{\cup} (G, B, \mathfrak{T}) = (H, C, \mathfrak{T})$. From definition of soft union and Equation 1.1, we have

$$H(p) = \begin{cases} F(p) & , \text{if } p \in A - B \\ G(p) & , \text{if } p \in B - A \\ F(p) \cup G(p) & , \text{if } p \in A \cap B \end{cases}$$

and $C = A \cup B$. Since $A \cap B = \emptyset$, either $H(p) = F(p)$ where $p \in A$ or $H(p) = G(p)$ where $p \in B$ for each $p \in C$. Since $(F(p), \mathfrak{T}_{F(p)})$ and $(G(p), \mathfrak{T}_{G(p)})$ are subspace of U where $p \in A$ and $p \in B$, respectively, then we obtain that $(H(p), \mathfrak{T}_{H(p)})$ is a subspace of U for each $p \in C$. Thus (H, C, \mathfrak{T}) is a soft topological space over U .

We obtain the following theorem which proof is similar to the proof of Theorem 2.3.

Theorem 2.5.

If (F, A, \mathfrak{T}) and (G, B, \mathfrak{T}) are soft topological space over (U, \mathfrak{T}) then $(F, A, \mathfrak{T}) \mathbf{And} (G, B, \mathfrak{T})$ is a soft topological space over U where the intersection of all subspaces according to each parameter is the Cartesian intersection subspace topology on the intersection of subsets according to each parameters.

$(F, A, \mathfrak{T}) \mathbf{Or} (G, B, \mathfrak{T})$ may not be soft topological space where (F, A, \mathfrak{T}) and (G, B, \mathfrak{T}) are soft topological space over (U, \mathfrak{T}) . We can give the following example to see this.

Example 2.6.

Let $U = \{a, b, c, d\}$ be a set, $\mathfrak{T} = \{\emptyset, U, \{a, b, c\}, \{a, b\}, \{c\}\}$ be topology on U .

$(F, A) = \{1 = \{a, c\}, 2 = \{d\}\}$ soft topological space over U such that $\mathfrak{T}_{F(1)} = \{\emptyset, \{a, c\}, \{a\}, \{c\}\}$ and $\mathfrak{T}_{F(2)} = \{\emptyset, \{d\}\}$ and $(G, B) = \{2 = \{b, d\}\}$ soft topological space over U such that $\mathfrak{T}_{G(2)} = \{\emptyset, \{b, d\}, \{b\}\}$. Now, we have

$$(F, A) \text{Or} (G, B) = (H, A \times B) \\ = \{(1, 2) = \{a, b, c, d\}, (2, 2) = \{b, d\}\}$$

and we have that $\mathfrak{T}_{F(1)} \cup \mathfrak{T}_{G(2)} \neq \mathfrak{T}_{H(1,2)} = \mathfrak{T}_{F(1) \cup G(2)}$. Thus $(H(1,2), \mathfrak{T}_{H(1,2)})$ is not subspace of (U, \mathfrak{T}) . Hence, $(H, A \times B, \mathfrak{T})$ is not a soft topological space over U .

Note that, since every topological space is a subspace of itself, each relative whole soft set is a soft topological space over any given topological space. Such soft topological spaces are called overt soft topological space, i.e. if (U, \mathfrak{T}) is a topological space and \tilde{U}_A is a relative whole soft set over U then it is called that $(\tilde{U}_A, \mathfrak{T})$ is an overt soft topological space over U .

From Theorem 1.10, we obtain a soft topological space over given any topological space and soft set defined on it, obviously.

Remark 2.7.

Let (U, \mathfrak{T}) be a topological space and (F, A) be a soft set over U where $A \subseteq E$. For each $p \in A$, $\mathfrak{T}_{F(p)} = \{F(p) \cap O \mid O \in \mathfrak{T}\}$ is a topology on $F(p)$, and so (F, A, \mathfrak{T}) is a soft topological space.

Example 2.8.

Let $U = \{a, b, c, d\}$ and $\mathfrak{T} = \{\emptyset, U, \{a, b\}, \{a, b, c\}, \{c, d\}, \{c\}\}$ be a topology on U . Let $A = \{1, 3, 4\}$ with $E = \{1, 2, 3, 4, 5, 6\}$, and let $(F, A) = \{1 = \{a, c\}, 3 = \{b, d\}, 4 = U\}$. Then we have three topologies as

$$\mathfrak{T}_{F(1)} = \{\emptyset, \{a, c\}, \{a\}, \{c\}\} \\ \mathfrak{T}_{F(3)} = \{\emptyset, \{b, d\}, \{b\}, \{d\}\} \\ \mathfrak{T}_{F(4)} = \mathfrak{T}$$

Hence, we obtain the soft topological space (F, A, \mathfrak{T}) over U .

Theorem 2.9.

If (F, A, \mathfrak{T}) and (G, B, \mathfrak{T}) are soft topological space over (U, \mathfrak{T}) , then $(F, A, \mathfrak{T}) \times (G, B, \mathfrak{T})$ is a soft topological space over $U \times U$.

Proof. From the definition of Cartesian product of soft sets and Lemma 1.15, it is obvious.

Definition 2.10.

The soft topological space obtained in Theorem 2.9 is called product soft topological space over $U \times U$.

Theorem 2.11.

Let (U, \mathfrak{T}) be a topological space, (F, A, \mathfrak{T}) and (G, B, \mathfrak{T}) be soft topological spaces over U . If (F, A) is similar to (G, B) ($(F, A) \cong (G, B)$), then they are same soft topological spaces over U .

Proof. Since $(F, A) \cong (G, B)$, we have the bijection $\phi: A \rightarrow B$ such that $F(p) = (G \circ \phi)(p)$ for each $p \in A$ from definition of similarity of soft sets. So, there is one and only one parameter $p' \in B$ corresponding to each parameter $p \in A$. Therefore, we have $\mathfrak{T}_{F(p)} = \mathfrak{T}_{G(\phi(p))} = \mathfrak{T}_{G(p')}$ for each $p \in A$ and $p' \in B$. Hence, we obtain same subspaces for each parameters.

Some Topological Properties of Soft Topological Spaces

In this section, we mention about some basic topological properties such as Hausdorffness, compactness, connectedness of soft topological spaces.

Definition 3.1.

Let (F, A, \mathfrak{T}) be a soft topological spaces over (U, \mathfrak{T}) . It is called that (F, A, \mathfrak{T}) is a Hausdorff soft topological space if $(F(p), \mathfrak{T}_{F(p)})$ is Hausdorff for each $p \in A$.

Example 3.2.

Let $U = \{a, b, c, d\}$ be a universal set, $\mathfrak{T} = \{\emptyset, U, \{a, b\}, \{c, d\}\}$

be a topology on U and $E = \{1, 2, 3, 4, 5\}$ be a parameters set. Let (F, A, \mathfrak{T}) be a soft topological space over U such that

$$(F, A) = \{1 = \{a, c\}, 2 = \{b, d\}\} \text{ and}$$

$$\mathfrak{T}_{F(1)} = \{\emptyset, \{a, c\}, \{a\}, \{c\}\}$$

$$\mathfrak{T}_{F(2)} = \{\emptyset, \{b, d\}, \{b\}, \{d\}\}$$

Since $(F(1), \mathfrak{T}_{F(1)})$ and $(F(2), \mathfrak{T}_{F(2)})$ are Hausdorff,

then (F, A, \mathfrak{T}) is a Hausdorff soft topological space over U from Definition 3.1.

Note that, the topological space (U, \mathfrak{T}) does not need to be a Hausdorff space.

We obtain following theorem for Hausdorff soft topological spaces.

Theorem 3.3.

If (U, \mathfrak{T}) is a Hausdorff space and (F, A, \mathfrak{T}) is a soft topological space over it. Then (F, A, \mathfrak{T}) is Hausdorff.

Proof. It is obvious from Lemma 1.16 and Definition 3.1.

Theorem 3.4.

Let (F, A, \mathfrak{T}) and (G, B, \mathfrak{T}) be soft topological spaces over (U, \mathfrak{T}) . Their product space is Hausdorff if and only if they are Hausdorff.

Proof. Suppose that (F, A, \mathfrak{T}) and (G, B, \mathfrak{T}) are Hausdorff, then their product $(H, A \times B, \mathfrak{T} \times \mathfrak{T})$ is a soft topological space over $U \times U$ from Theorem 2.9. From Lemma 1.17, we gain $(H(p_1, p_2), \mathfrak{T}_{H(p_1, p_2)})$ is Hausdorff for each $(p_1, p_2) \in A \times B$. Thus, $(H, A \times B, \mathfrak{T} \times \mathfrak{T})$ is Hausdorff.

Conversely, suppose that

$$(F, A, \mathfrak{T}) \tilde{\times} (G, B, \mathfrak{T}) = (H, A \times B, \mathfrak{T} \times \mathfrak{T})$$

and $(H, A \times B, \mathfrak{T} \times \mathfrak{T})$ is Hausdorff. So, $(H(p_1, p_2), \mathfrak{T}_{H(p_1, p_2)})$ is Hausdorff for each $(p_1, p_2) \in A \times B$ from Definition 3.1 and the topological space $(H(p_1, p_2), \mathfrak{T}_{H(p_1, p_2)})$ is product of $(F(p_1), \mathfrak{T}_{F(p_1)})$ and $(G(p_2), \mathfrak{T}_{G(p_2)})$ for each $p_1 \in A$ and $p_2 \in B$ from Definition 2.10. We have that $(F(p_1), \mathfrak{T}_{F(p_1)})$

and $(G(p_2), \mathfrak{T}_{G(p_2)})$ are Hausdorff from Lemma 1.17 for each $p_1 \in A$ and $p_2 \in B$. Hence, (F, A, \mathfrak{T}) and (G, B, \mathfrak{T}) are Hausdorff.

Theorem 3.5.

If (U, \mathfrak{T}) is a Hausdorff space and (F, A, \mathfrak{T}) and (G, B, \mathfrak{T}) are soft topological space over U , then $(F, A, \mathfrak{T}) \tilde{\times} (G, B, \mathfrak{T})$ is Hausdorff.

Proof. The direct result of Theorem 3.3 and Theorem 3.4.

Definition 3.6.

Let (F, A, \mathfrak{T}) be a soft topological space over (U, \mathfrak{T}) . It is called that (F, A, \mathfrak{T}) is a compact soft topological space if $(F(p), \mathfrak{T}_{F(p)})$ is compact subspace of (U, \mathfrak{T}) for each $p \in A$.

Example 3.7.

Consider the usual topological space of real numbers $(\mathbb{R}, \mathcal{U})$. Define the soft set (F, A) over \mathbb{R} such that $F: A \rightarrow P(\mathbb{R}), F(p) = [p-1, p+1]$ where $p \in A = \{1, 2, 3, 4\} \subseteq \mathbb{N}$ and

$$\mathfrak{T}_{F(p)} = \{[p-1, p+1] \cap O \mid p \in A, O \in \mathcal{U}\}$$

By definition, (F, A, \mathcal{U}) is a soft topological space. Since each subspace is compact, then (F, A, \mathcal{U}) is a compact soft topological space from Definition 3.6.

Note that, if U is a finite set, it is compact according to each topology defined on it. For this reason;

Example 3.8.

Soft topological space given in Example 3.2 is a compact soft topological space.

Proof. It is obvious.

Similar to the above theorems, we can also give following;

Theorem 3.12.

Let (U, \mathfrak{T}) be a Hausdorff space, (F, A, \mathfrak{T}) and (G, B, \mathfrak{T}) be compact soft topological spaces over U . Then $(F, A, \mathfrak{T}) \mathbf{And} (G, B, \mathfrak{T})$ is a compact soft topological space.

Theorem 3.13.

Let (U, \mathfrak{T}) be a topological space, (F, A, \mathfrak{T}) and (G, B, \mathfrak{T}) be compact soft topological spaces over U . Then $(F, A, \mathfrak{T}) \tilde{\times} (G, B, \mathfrak{T})$ is a compact soft topological space over $U \times U$.

Proof. From the definition of cartesian product of soft sets and Lemma 1.21, it is straightforward.

Definition 3.14.

Let (U, \mathfrak{T}) be a topological space, and (F, A, \mathfrak{T}) be a soft topological space over U . It is called that (F, A, \mathfrak{T}) is a connected soft topological space if $(F(p), \mathfrak{T}_{F(p)})$ is connected subspace of U for each $p \in A$.

Example 3.15.

Let $U = \{a, b, c, d, e\}$ be a set and

$$\mathfrak{T} = \{\emptyset, U, \{a\}, \{c, d\}, \{a, c, d\}, \{b, c, d, e\}\}$$

be a topology on U . Let $E = \{1, 2, 3, 4, 5, 6\}$ and

$$(F, A) = \{2 = \{b, d, e\}, 4 = \{b, c, e\}\}$$

be a soft topological space over U such that

$$\mathfrak{T}_{F(2)} = \{\emptyset, \{b, d, e\}, \{d\}\}$$
 and

$$\mathfrak{T}_{F(4)} = \{\emptyset, \{b, c, e\}, \{c\}\}$$

Since $(F(p), \mathfrak{T}_{F(p)})$ is a connected subspace for each $p \in A$, (F, A, \mathfrak{T}) is a connected soft topological space over U .

Example 3.16.

Consider the usual topological space of the real numbers $(\mathbb{R}, \mathcal{U})$. Define the soft topological space (F, A, \mathcal{U}) such that $F(p) = (p-1, p+1)$ for each $p \in \mathbb{N}$, and $\mathcal{U}_{F(p)}$ is relative topology of $F(p)$ with respect to usual topology \mathcal{U} . Since each open interval $(p-1, p+1)$ is connected for each $p \in \mathbb{N}$ in $(\mathbb{R}, \mathcal{U})$, then (F, A, \mathcal{U}) is a connected soft topological space.

Theorem 3.17.

Let (U, \mathfrak{T}) be a topological space and (F, A, \mathfrak{T}) and (G, B, \mathfrak{T}) be connected soft topological spaces over U . If

$F(p_1) \cap G(p_2) \neq \emptyset$ for each $p_1 \in A$ and $p_2 \in B$, then $(F, A, \mathfrak{T}) \tilde{\cup} (G, B, \mathfrak{T})$ is a connected soft topological space over U .

Proof. Suppose that $(F, A, \mathfrak{T}) \tilde{\cup} (G, B, \mathfrak{T}) = (H, C, \mathfrak{T})$. So, from definition of union of soft sets we have $H(p) = F(p)$ if $p \in A - B$, $H(p) = G(p)$ if $p \in B - A$ and $H(p) = F(p) \cup G(p)$ if $p \in A \cap B$. The desired result is obvious for the first two cases. Let's examine the third case, i.e. $H(p) = F(p) \cup G(p)$ for $p \in A \cap B$. We know from the hypothesis that subspaces are not disjoint for each parameter and all of them connected, so we obtain that $H(p) = F(p) \cup G(p)$ is connected for each $p \in A \cap B$ from Lemma 1.22. Hence, (H, C, \mathfrak{T}) is a connected soft topological space over U .

Theorem 3.18.

Let (U, \mathfrak{T}) be a topological space, (F, A, \mathfrak{T}) be a connected soft topological space over U . If (F, A) is a full soft set over U and $\bigcap_{p \in A} F(p) \neq \emptyset$, then the topological space (U, \mathfrak{T}) is connected.

Proof. It is straightforward from the definition of full soft set and Lemma 1.22.

CONCLUSION

In this article, we have approached the concept of soft topological space with a new perspective. We define soft topological space that is defined on a topological space as a parametrization of some subspaces of the space in Molodtsov's sense [1]. Besides, some basic topological concepts such as Hausdorffness, compactness and connectedness are given for soft topological spaces over given any topological space, and we have given some results for these concepts. In addition to these, we have given the notion of Cartesian intersection and Cartesian union for set-families in general. Using these definitions we have given a result for the intersection of two subspaces of any topological space.

One of the most important topics of topology is undoubtedly the concept of continuity. In future work, someone can study the concept of continuity among soft topological spaces over given any topological space. Of course, it can be studied in detail in all other topological concepts.

The author hope that this article sheds light on a way of working scientists in this field.

References

1. Molodtsov, D. Soft set theory – first results. *Comput. Math. Appl.* 37 (1999) 19–31.
2. Maji, PK, Biswas, R, Roy, AR. Soft set theory. *Comput. Math. Appl.* 45 (2003) 555–562.
3. Ali, MI, Feng, F, Liu, X, Min, WK, Shabir, M. On some new operations in soft set theory. *Comput. Math. Appl.* 57 (2009) 1547–1553.
4. Babitha, KV, Sunil, JJ. Soft set relations and functions. *Comput. Math. Appl.* 60 (2010) 1840–1849.
5. Kim, YK, Min, WK. Full soft sets and full soft decision systems. *J. Intell. Fuzzy Systems* 26 (2) (2014) 925–933.
6. Min, WK. Similarity in soft set theory. *Appl. Math. Lett.* 25 (3) (2012) 310–314.
7. Munkres, JR. *Topology*. 2nd, edition. Prentice Hall, Inc. 2000.
8. Yuksel, Ş. *General topology*. 5th, extended edition. Eğitim Kitabevi Yayınları, 2006 (In Turkish).
9. Shabir, M, Naz, M. On soft topological spaces. *Comput. Math. Appl.* 61 (7) (2011) 1786–1799.
10. Aktaş, H, Çağman, N. Soft sets and soft groups. *Inform. Sci.* 177 (13) (2007) 2726–2735.
11. Acar, U., Koyuncu, F., Tanay, B. Soft sets and soft rings. *Comput. Math. Appl.* 59(11)(2010) 3458–3463.

Enhanced Enzyme Activity with Ferritin Nanocages

Eylem Turan 

Gazi University, Department of Chemistry, Besevler, Ankara, Turkey.

ABSTRACT

In this study, a novel enzyme system based on ferritin nanocages was designed. α -Amylase was covalently crosslinked on surface of ferritin nanocages by EDC/NHS. The activity of immobilized enzyme was monitored by using UV-vis spectrophotometer. The optimum temperature of immobilized enzyme shifted from 50 °C to 70 °C due to the ferritin nanocages. In addition, The K_m and V_{max} values of immobilized enzymes were 5.19 mg mL⁻¹ and 3.3x10⁻⁵ U mg⁻¹, respectively. This novel enzyme system displayed higher catalytic activity and enhanced stability.

Keywords:

Ferritin nanocages; α -amylase; Enzyme immobilization; EDC/NHS; Covalently crosslinked

INTRODUCTION

In recent years, the combined use of chemistry, biology and nanotechnology has made significant contributions to the field of medical diagnosis and treatment. For example, quantum dots or fluorochrome-linked macromolecules have been developed as cell and tissue imaging materials. Iron oxide nanoparticles have also been developed for use as biomedical applications, such as hyperthermia, cancer diagnosis and therapy, and as a contrast agent in magnetic resonance imaging (MRI). However, these nanostructures, which have been subjected so much research on them, they have toxic effects. For this reason, the search for biocompatible nanomaterials in diagnosis and treatment of diseases has become intense. Protein lattices such as ferritin and virus capsules (protein layer outside the virus) are versatile nanoscale perfect architectures that allow both genetic and chemical modification. Nanoscale protein architects with multiple functionalities have a good potential, especially in medical imaging and treatment fields. Protein lattice structures have different subunits that can be used as the interface between the inner and outer and subunits. The subunits can be easily modified genetically and chemically to demonstrate versatile functionality. Ferritin is a very large iron storage and detoxification protein found in many organisms [1,2]. In nature, ferritins are filled with iron. Ferritin is a natural nanocage and also ready to be combined with biomolecules for preparing nanobiosensors. Thus,

biomedical applications have a promising potential for sensitive and robust bioassays. Based on these properties, ferritin is not only due to its inherent nano-size and nanostructure, but also by its high stability and specific structures [3-9]. In addition to these superior properties, nanotechnology researchers have found that nanosized biomaterials such as ferritin, apoferritin in biomedical field, such as diagnosis and treatment of diseases because they are biodegradable, biocompatible and non-toxic properties [10-12].

In this study, it is aimed to developed ferritin nanocage-based platform to construct an enzyme system. To prepare this system, α -amylase enzyme was covalently crosslinked on the outer surface of the ferritin nanocages. The activity of this novel enzyme system was investigated for different temperatures and substrate concentrations using UV-vis spectrophotometer.

EXPERIMENTAL

Materials

All chemicals were used for the preparation enzyme immobilization ferritin nanocages. Ferritin nanocages Type I: From Horse Spleen and α -amylase (E.C.3.2.1.1, 47 kDa) were obtained from Sigma.

Enzyme immobilization

To immobilize α -amylase onto the ferritin nanocages, firstly, ferritin nanocages were suspended in phosphate buffer solution (pH 7.4) by ultrasonic bath

Article History:

Received: 2017/09/26

Accepted: 2017/11/27

Online: 2017/12/22

Correspondence to: Eylem Turan

Gazi University, Department of Chemistry,

Besevler, Ankara, Turkey

Tel: +90 (312) 202-1145

E-Mail: eylem.turan@gmail.com

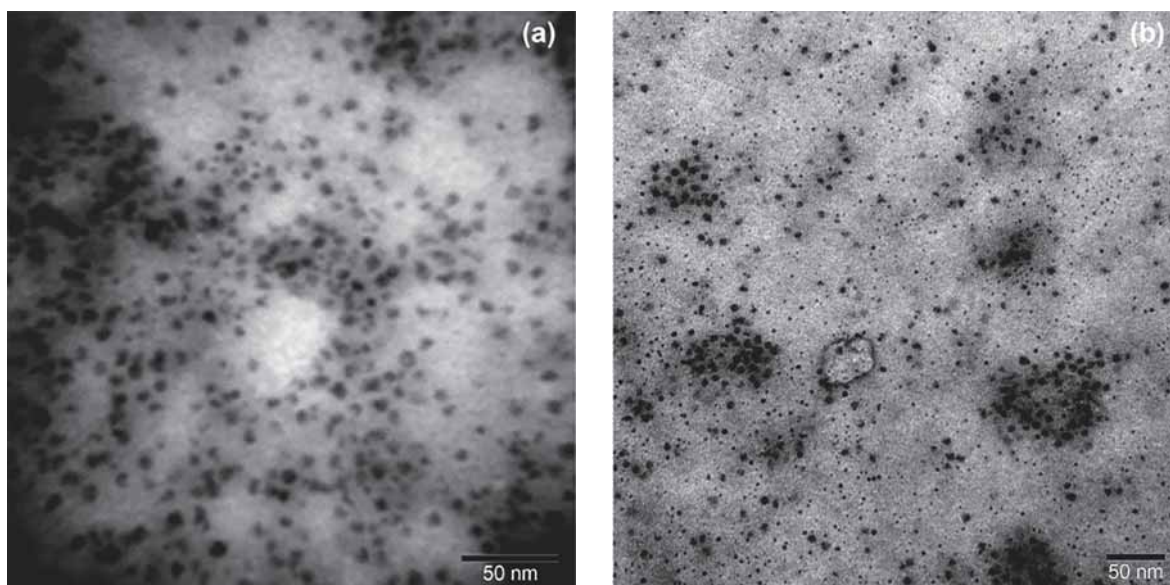


Figure 1. TEM images of a) ferritin nanocages b) enzyme immobilized ferritin nanocages

during 45 min. Then, α -amylase was also preactivated with EDC:NHS (1:1, w:w) and in phosphate buffer solution for 30 min, and added to the ferritin nanocage suspension, and stirred at room temperature for 4 h with constant shaking. The enzyme immobilized ferritin nanocages were washed with the buffer solution. Finally re-dispersed in phosphate buffer solution (pH 7.4). After redispersed in PBS (pH 7.4) enzyme immobilized ferritin nanocages were kept at +4 °C until further use.

Immobilization experiments

The activity of α -amylase was determined via examining the reduction of starch in different conditions. The concentration of substrate was determined via UV-vis spectrophotometer at 560 nm.

Immobilization efficiency was determined by using the Eq.1:

$$\text{Immobilization efficiency} = 1 - \left(\frac{[\text{enzyme}]_{\text{upper phase}}}{[\text{enzyme}]_{\text{initial}}} \right) \quad (1)$$

Where $[\text{enzyme}]_{\text{supernatant}}$ is the enzyme concentration in the upper phase and $[\text{enzyme}]_{\text{initial}}$ is the initial concentration of the enzyme.

Characterization

TEM investigation was performed using a JEOL 100CX instrument working at 120 kV. UV-vis absorbances were determined by a Shimadzu UV-2450 spectrophotometer at room temperature.

RESULTS AND DISCUSSION

Preparation of novel enzyme system

Firstly, α -amylase enzyme was covalently crosslinked

onto the ferritin nanocages via EDC/NHS. The TEM characterization results were summarized Fig. 1a.

Fig. 1a demonstrated the TEM images of bare ferritin nanocages. The bare ferritin nanocages were uniform size and no exhibited agglomeration in Fig. 1. Their average diameters 13.7 ± 0.54 nm. With the enzyme immobilized, the ferritin nanocages well dispersed with an average diameter 17.3 ± 0.82 nm was determined in Fig. 1b.

Enzyme immobilization was accomplished via reacting a constant concentration of ferritin nanocages with a fixed concentration of enzyme solution. α -amylase enzyme was preactivated by EDC/NHS in solution before it was linked on the ferritin nanocage surfaces. Finally, α -amylase enzyme was immobilized on the surface of the ferritin nanocages by reacting between the amino groups of nanocages and carboxyl groups of enzyme. The efficiency of immobilization was determined to be 97.3%. This result indicated that, binding process was successful.

Thermal stability of immobilized α -amylase was

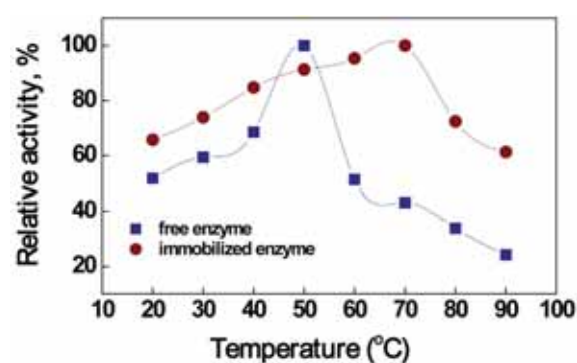


Figure 2. Effect of temperature on free and immobilized enzyme activity

Table 1. Kinetic parameters of free and immobilized enzymes

	K_m mg mL ⁻¹	V_{max} U mg ⁻¹
free enzyme	2.63	10.6×10^{-5}
immobilized enzyme	5.19	3.3×10^{-5}

compared with the free enzyme at different temperatures (20-90 °C). The results were showed in Fig 2.

Free enzyme very stable and can be incubated at 50 °C. Optimum temperature of immobilized enzyme was changed from 50 °C to 70 °C. As a result, immobilized enzyme more resistant to heat than the free enzyme. It can be probably ferritin nanocages were enhanced enzyme activity at higher temperatures. Moreover, it can be the hydration layer around the ferritin nanocages prevented the thermal denaturation of the enzyme.

Kinetic parameters of free and immobilized enzymes were determined by using the Michaelis-Menten equation. The results were summarized in Table 1.

The K_m values of free enzyme and immobilized enzymes were 2.63 and 5.19 mg mL⁻¹, respectively. The V_{max} values of free enzyme and immobilized enzymes were found to be 10.6×10^{-5} and 3.3×10^{-5} U mg⁻¹, respectively. The K_m value of immobilized enzyme higher then the free enzyme. It can be due to the changes in the conformation of the enzyme molecules after the immobilization and it may be increased enzyme activity [13].

Generally, enzymes may lose their activities due to environmental conditions. So that it is important their storage stability for industrial usage. In order to determine the storage stabilities of free and immobilized α -amylase enzyme, which were kept in phosphate buffer solution (pH 7.4) at +4 °C. Their activities were investigated in every 5 days during 30 days. (Fig. 3)

Free enzyme was lost its about all initial activity within 15 days but immobilized enzyme preserved about 96 % of the initial activity. After 30 days, the immobilized enzyme retained about 84 % of the initial activity. According to

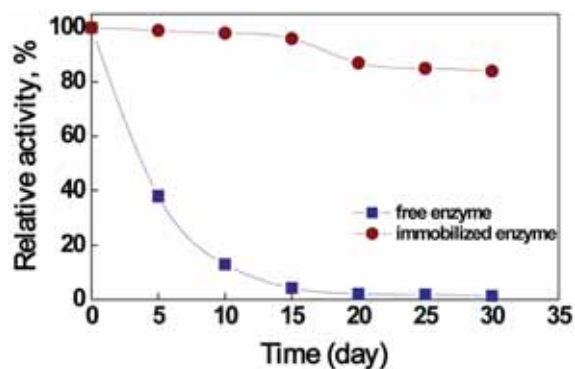


Figure 3. Storage stability of free and immobilized enzyme activity

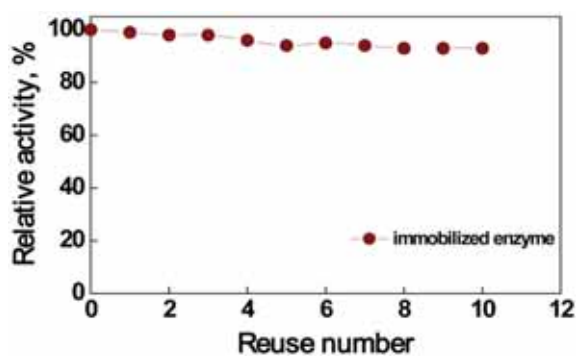


Figure 4. The reusability of immobilized enzyme

the results, the immobilization process and the ferritin nanocages increased the storage stability and durability of immobilized α -amylase.

The reusability of immobilized enzyme is very important feature for their large-scale applications. The reusability of immobilized enzyme was measured for 10 reuse in 1 day. (Fig.4)

In Fig. 4, after 10 reuses immobilized enzyme protected about 93% of the initial activity. This result showed that there was no significant loss after the 10 reuses. Therefore the ferritin nanocages can be reused and they could be an economic platform for enzyme immobilization.

CONCLUSION

A novel enzyme system was developed by using natural protein cages. Model enzyme α -amylase was covalently immobilized onto the nanocages and optimum immobilization conditions were determined. The immobilized enzyme showed better temperature resistance than the free enzyme. In addition, storage stability of immobilized enzyme was excellent when compared the free enzyme. These results can be attributed to the ferritin nanocages. As a result, ferritin nanocages are very important platforms for enzyme immobilization because of their enzyme mimic activity.

ACKNOWLEDGEMENTS

I am thankful to Prof. Dr. Zekiye Suludere for TEM analysis. I am also great thankful to Assoc. Prof. Dr. Hayrettin Tümtürk for his all support.

REFERENCES

1. Bou-Abdallah F, Zhao G, Biasiotto G, Poli M, Arosio P, Chasteen ND, Facilitated diffusion of iron(II) and dioxygen substrates into human H-chain ferritin. A fluorescence and absorbance study employing the ferroxidase center substitution Y34W. JACS, 130 (2008) 17801-17811.
2. Bulvik BE, Berenshtein E, Meyron-Holtz EG, Konijn

- AM, Chevion M, Cardiac protection by preconditioning is generated via an iron-signal created by proteasomal degradation of iron proteins. *PLoS ONE*, 7 (2012), 1–9.
3. Ullrich A, Horn S, Structural investigations on differently sized monodisperse iron oxide nanoparticles synthesized by remineralization of apoferritin molecules. *J. Nanopart. Res.* 15 (2013), 1–9.
 4. Zhen ZP, Tang W, Guo CL, Ferritin nanocages to encapsulate and deliver photosensitizers for efficient photodynamic therapy against cancer. *ACS Nano*, 7 (2013) 6988–6996.
 5. Tang Z, Wu H, Zhang Y, Li Z, Lin Y, Enzyme-Mimic Activity of Ferric Nano-Core Residing in Ferritin and Its Biosensing Applications. *Anal. Chem.* 83 (2011) 8611–8616.
 6. Tedesco AC, Oliviera DM, Lacava ZGM, Azevedo RB, Lima ECD, Morais PC, Investigation of the binding constant and stoichiometry of biocompatible cobalt ferrite-based magnetic fluids to serum albumin. *Journal of Magnetism and Magnetic Materials.* 272-276 (2004) 2404-2405.
 7. Powell JJ, Bruggraber SFA, Faria N, Poots LK, Hondow N, Pennycook TJ, Latunde-Dada GO, Simpson RJ, Brown AP, Pereira DIA, A nano-disperse ferritin-core mimetic that efficiently corrects anemia without luminal iron redox activity. *Nanomedicine: Nanotechnology, Biology, and Medicine* 10 (2014) 1529–1538.
 8. Rakshit T, Mukhopadhyay R, Tuning band gap of holoferritin by metal core reconstitution with Cu, Co and Mn. *Langmuir* 27 (2011) 9681–9686.
 9. Zhao J, Liu ML, Zhang YY, Li HT, Lin YH, Yao SZ, Apoferritin protein nanoparticles dually labeled with aptamer and horseradish peroxidase as a sensing probe for thrombin detection. *Anal. Chim. Acta* 759 (2013) 53–60.
 10. Soppimath KS, Aminabhavi TM, Kulkarni AR, Rudzinski WE, Biodegradable polymeric nanoparticles as drug delivery devices. *J. Control. Release* 70 (2001) 1–20.
 11. Mundargi RC, Babu VR, Rangaswamy V, Patel P, Aminabhavi TM, Nano/micro Technologies for delivering macromolecular therapeutics using poly(D,L-lactide-co-glycolide) and its derivatives. *J. Control. Release* 125 (2008) 193–209.
 12. Chomoucka J, Drbohlavova J, Huska D, Adam V, Kizek R, Hubalek J, Magnetic nanoparticles and targeted drug delivering. *Pharmacol. Res.*, 62 (2010) 144–149.
 13. Tümtürk H, Yüksekdağ H, Acetylcholinesterase immobilized onto PEI-coated silica nanoparticles. *Artificial Cells, Nanomedicine, and Biotechnology* 44 (2016) 443–447.

Explicit Solutions of a Three-Dimensional System of Nonlinear Difference Equations

Bahriye Yilmazyıldırım^a, Durhasan Turgut Tollu^b 

^aNecmettin Erbakan University Graduate School of Natural and Applied Science, Turkey

^bNecmettin Erbakan University, Department of Mathematics-Computer Sciences, Konya, Turkey

ABSTRACT

In this paper, we show that the system of difference equations

$$x_{n+1} = \frac{x_n + y_n}{1 + x_n y_n}, y_{n+1} = \frac{y_n + z_n}{1 + y_n z_n}, z_{n+1} = \frac{z_n + x_n}{1 + z_n x_n}, n \in \mathbb{N}_0,$$

where the initial values x, y, z are real numbers, are solvable in explicit form via some changes of variables and tricks. Also, we determine the forbidden set of the initial values x, y, z for the above mentioned system and investigate asymptotic behavior of the well-defined solutions by using these explicit formulas.

Keywords:

Asymptotic behavior; explicit solution; rational difference equation; system

AMS Classification:

39A10

INTRODUCTION

Nonlinear difference equations constitute an important class of difference equations and studying of this kind of equations have recently attracted great interest. One can see this in some recent studies. See, for example [2-4,7-8,15-16,18,24-27]. Particularly, there have been a renewed interest on solvable ones of such equations and systems. For example, published papers on solvability of some types can be found in the references [5-6,10-14,28,31]. Additionally, there are some equations and systems whose solvability are newly discovered. For example, the solvability of the nonlinear difference equation

$$x_{n+1} = \frac{a + x_n x_{n-1}}{x_n + x_{n-1}}, n \in \mathbb{N}_0, \quad (1)$$

where $a \in [0, \infty)$ and the initial values x_{-1}, x_0 are real numbers, which was studied by Xianyi and Deming in [29], is newly discovered. The fact remains that the equations and the systems in the references [1,19-21,23,30], are so.

Our aim in this study is to show that the following systems of difference equations

$$x_{n+1} = \frac{x_n + y_n}{1 + x_n y_n}, y_{n+1} = \frac{y_n + z_n}{1 + y_n z_n}, z_{n+1} = \frac{z_n + x_n}{1 + z_n x_n}, n \in \mathbb{N}_0, \quad (2)$$

where real initial values x_0, y_0 and z_0 are real numbers, can be solved in explicit form. Also, we determine the forbidden set of the initial values x_0, y_0, z_0 for the system and investigate asymptotic behavior of the well-defined solutions by using these formulas.

Definition

Let

$$\begin{aligned} x_{n+1} &= f(x_n, y_n, z_n), y_{n+1} = g(x_n, y_n, z_n), \\ z_{n+1} &= h(x_n, y_n, z_n), n \in \mathbb{N}_0, \end{aligned} \quad (3)$$

where $f: \mathbb{R}^3 \rightarrow \mathbb{R}$, $g: \mathbb{R}^3 \rightarrow \mathbb{R}$ and $h: \mathbb{R}^3 \rightarrow \mathbb{R}$ is given functions, be a system of difference equations of first-order, and D_f, D_g and D_h be the domains of the functions f, g and h , respectively. Forbidden set of difference equation (3) is given by

$$F = \left\{ \begin{aligned} &((x_0, y_0, z_0) \in \mathbb{R}^3 : (x_i, y_i, z_i) \in D \text{ for } \\ &i \in \mathbb{N}_0, n-1, n \in \mathbb{N}_0, \text{ and } (x_n, y_n, z_n) \notin D) \end{aligned} \right\}$$

Article History:

Received: 2017/06/21

Accepted: 2017/08/25

Online: 2017/12/22

Correspondence to: Durhasan Turgut Tollu
Necmettin Erbakan University, Faculty
of Science, Department of Mathematics-
Computer Sciences, Konya, Turkey
E-Mail: ttollu@konya.edu.tr

where $D := D_f \times D_g \times D_h$. This set contains all the initial values which causes the undefinable solutions of the system. That is, the initial values chosen from the complement of the forbidden set always produce the well-defined solutions.

RESULTS

In this section, we give our main results by obtaining the general solution in explicit form of the system (2). Next, we determine the forbidden set of the initial values x_0, y_0, z_0 for the system (2). Additionally, we investigate asymptotic behavior of the well-defined solutions by using their explicit formulas.

The Explicit General Solution Of The System

To solve the system (2), we apply the changes of variables

$$x_n = \frac{e^{u_n} - 1}{e^{u_n} + 1}, \quad y_n = \frac{e^{v_n} - 1}{e^{v_n} + 1}, \quad z_n = \frac{e^{w_n} - 1}{e^{w_n} + 1} \quad (4)$$

to the system. Then, we have the linear system

$$u_{n+1} = u_n + v_n, \quad v_{n+1} = v_n + w_n, \quad w_{n+1} = w_n + u_n, \quad n \in \mathbb{N}_0 \quad (5)$$

The system (5) can be written as

$$u_{n+3} - 3u_{n+2} + 3u_{n+1} - 2u_n = 0, \quad n \in \mathbb{N}_0, \quad (6)$$

$$v_{n+3} - 3v_{n+2} + 3v_{n+1} - 2v_n = 0, \quad n \in \mathbb{N}_0, \quad (7)$$

and

$$w_{n+3} - 3w_{n+2} + 3w_{n+1} - 2w_n = 0, \quad n \in \mathbb{N}_0, \quad (8)$$

which are disjoint. Note that the equations (6)-(8) are in the same form. Therefore, we only solve one of them. Let choose Eq. (6) which can be written as

$$(u_{n+3} - 2u_{n+2}) - (u_{n+2} - 2u_{n+1}) + (u_{n+1} - 2u_n) = 0, \quad n \in \mathbb{N}_0.$$

Set $u_{n+2} - 2u_{n+1} = \tilde{u}_n$, So, we get the linear equation of order two

$$\tilde{u}_{n+1} = \tilde{u}_n - \tilde{u}_{n-1}, \quad n \in \mathbb{N}_0, \quad (9)$$

Eq. (9) is periodic with period 6 such that $\tilde{u}_{6n+i} = \tilde{u}_i$, ($i = 0, 5$) which implies

$$u_{6n+2+i} - 2u_{6n+1+i} = u_{i+2} - 2u_{i+1}, \quad n \in \mathbb{N}_0. \quad (10)$$

By adding the backward iterate of (10) to own itself, we get

$$u_{6n+2+i} - 2u_{6n+1+i} + u_{6n+1+i} - 2u_{6n+i} = u_{i+2} - 2u_{i+1} + u_{i+1} - 2u_i$$

or

$$u_{6n+2+i} - u_{6n+1+i} - 2u_{6n+i} = u_{i+2} - u_{i+1} - 2u_i, \quad n \in \mathbb{N}_0. \quad (11)$$

Eq. (6) can be also written in the further form

$$(u_{n+3} - u_{n+2} + u_{n+1}) - 2(u_{n+2} - u_{n+1} + u_n) = 0. \quad (12)$$

If we apply the change of variables

$$u_{n+2} - u_{n+1} + u_n = \hat{u}_n \quad (13)$$

to Eq. (12), then, from Eq. (12), it follows that

$$\hat{u}_{n+1} - 2\hat{u}_n = 0 \quad (14)$$

whose the general solution is given by

$$\hat{u}_n = 2^n \hat{u}_0 \quad (15)$$

which implies

$$u_{n+2} - u_{n+1} + u_n = 2^n (u_2 - u_1 + u_0). \quad (16)$$

Eq. (16) can be decomposed in terms of its own subscript as follows;

$$u_{6n+2+i} - u_{6n+1+i} + u_{6n+i} = 2^{6n+i} (u_2 - u_1 + u_0), \quad i = \overline{0, 5} \quad (17)$$

By subtracting (11) from (17), we get the formula

$$u_{6n+i} = \frac{1}{3} (2^{6n+i} (v_1 + u_0) - (y_{i+1} - 2u_i)), \quad i = \overline{0, 5}, \quad (18)$$

for the solution (u_n) of Eq. (6). We also state the formula (18) explicitly such that

$$u_{6n} = \frac{2^{6n} + 2}{3} u_0 + \frac{2^{6n} - 1}{3} v_0 + \frac{2^{6n} - 1}{3} w_0, \quad (19)$$

$$u_{6n+1} = \frac{2^{6n+1} + 1}{3} u_0 + \frac{2^{6n+1} + 1}{3} v_0 + \frac{2^{6n+1} - 2}{3} w_0, \quad (20)$$

$$u_{6n+2} = \frac{2^{6n+2} - 1}{3} u_0 + \frac{2^{6n+2} + 2}{3} v_0 + \frac{2^{6n+2} - 1}{3} w_0, \quad (21)$$

$$u_{6n+3} = \frac{2^{6n+3} - 2}{3} u_0 + \frac{2^{6n+3} + 1}{3} v_0 + \frac{2^{6n+3} + 1}{3} w_0, \quad (22)$$

$$u_{6n+4} = \frac{2^{6n+4} - 1}{3} u_0 + \frac{2^{6n+4} - 1}{3} v_0 + \frac{2^{6n+4} + 2}{3} w_0, \quad (23)$$

$$u_{6n+5} = \frac{2^{6n+5} + 1}{3} u_0 + \frac{2^{6n+5} - 2}{3} v_0 + \frac{2^{6n+5} + 1}{3} w_0 \quad (24)$$

for $n \in \mathbb{N}_0$, Consequently, by the change of variables $x_n = \frac{e^{u_n} - 1}{e^{u_n} + 1}$, we have the formulas

$$x_{6n} = 1 - \frac{2}{\left(\frac{1+x_0}{1-x_0}\right)^{\frac{2^{6n+2}}{3}} \left(\frac{1+y_0}{1-y_0}\right)^{\frac{2^{6n-1}}{3}} \left(\frac{1+z_0}{1-z_0}\right)^{\frac{2^{6n-1}}{3}} + 1} \quad (25)$$

$$x_{6n+1} = 1 - \frac{2}{\left(\frac{1+x_0}{1-x_0}\right)^{\frac{2^{6n+1}+1}{3}} \left(\frac{1+y_0}{1-y_0}\right)^{\frac{2^{6n+1}-1}{3}} \left(\frac{1+z_0}{1-z_0}\right)^{\frac{2^{6n+1}-2}{3}} + 1} \quad (26)$$

$$x_{6n+2} = 1 - \frac{2}{\left(\frac{1+x_0}{1-x_0}\right)^{\frac{2^{6n+2}-1}{3}} \left(\frac{1+y_0}{1-y_0}\right)^{\frac{2^{6n+2}+2}{3}} \left(\frac{1+z_0}{1-z_0}\right)^{\frac{2^{6n+2}-1}{3}} + 1} \quad (27)$$

$$x_{6n+3} = 1 - \frac{2}{\left(\frac{1+x_0}{1-x_0}\right)^{\frac{2^{6n+3}-2}{3}} \left(\frac{1+y_0}{1-y_0}\right)^{\frac{2^{6n+3}+1}{3}} \left(\frac{1+z_0}{1-z_0}\right)^{\frac{2^{6n+3}+1}{3}} + 1} \quad (28)$$

$$x_{6n+4} = 1 - \frac{2}{\left(\frac{1+x_0}{1-x_0}\right)^{\frac{2^{6n+4}-1}{3}} \left(\frac{1+y_0}{1-y_0}\right)^{\frac{2^{6n+4}-1}{3}} \left(\frac{1+z_0}{1-z_0}\right)^{\frac{2^{6n+4}+2}{3}} + 1} \quad (29)$$

$$x_{6n+5} = 1 - \frac{2}{\left(\frac{1+x_0}{1-x_0}\right)^{\frac{2^{6n+5}-1}{3}} \left(\frac{1+y_0}{1-y_0}\right)^{\frac{2^{6n+5}-2}{3}} \left(\frac{1+z_0}{1-z_0}\right)^{\frac{2^{6n+5}+1}{3}} + 1} \quad (30)$$

which are the formulas of the variable x_n , for $n \in \mathbb{N}_0$. The formulas of y_n can be obtained by the first equation of (2). That is, by solving y_n in this equation, we have

$$y_n = \frac{x_{n+1} - x_n}{1 - x_{n+1}x_n}. \quad (31)$$

From (25)-(31), it follows that

$$y_{6n} = 1 - \frac{2}{\left(\frac{1+x_0}{1-x_0}\right)^{\frac{2^{6n}-1}{3}} \left(\frac{1+y_0}{1-y_0}\right)^{\frac{2^{6n}+2}{3}} \left(\frac{1+z_0}{1-z_0}\right)^{\frac{2^{6n}-1}{3}} + 1} \quad (32)$$

$$y_{6n+1} = 1 - \frac{2}{\left(\frac{1+x_0}{1-x_0}\right)^{\frac{2^{6n+1}-2}{3}} \left(\frac{1+y_0}{1-y_0}\right)^{\frac{2^{6n+1}+1}{3}} \left(\frac{1+z_0}{1-z_0}\right)^{\frac{2^{6n+1}+1}{3}} + 1} \quad (33)$$

$$y_{6n+2} = 1 - \frac{2}{\left(\frac{1+x_0}{1-x_0}\right)^{\frac{2^{6n+2}-1}{3}} \left(\frac{1+y_0}{1-y_0}\right)^{\frac{2^{6n+2}-1}{3}} \left(\frac{1+z_0}{1-z_0}\right)^{\frac{2^{6n+2}+2}{3}} + 1} \quad (34)$$

$$y_{6n+3} = 1 - \frac{2}{\left(\frac{1+x_0}{1-x_0}\right)^{\frac{2^{6n+3}+1}{3}} \left(\frac{1+y_0}{1-y_0}\right)^{\frac{2^{6n+3}-2}{3}} \left(\frac{1+z_0}{1-z_0}\right)^{\frac{2^{6n+3}+1}{3}} + 1} \quad (35)$$

$$y_{6n+4} = 1 - \frac{2}{\left(\frac{1+x_0}{1-x_0}\right)^{\frac{2^{6n+4}+2}{3}} \left(\frac{1+y_0}{1-y_0}\right)^{\frac{2^{6n+4}-1}{3}} \left(\frac{1+z_0}{1-z_0}\right)^{\frac{2^{6n+4}-1}{3}} + 1} \quad (36)$$

$$y_{6n+5} = 1 - \frac{2}{\left(\frac{1+x_0}{1-x_0}\right)^{\frac{2^{6n+5}+1}{3}} \left(\frac{1+y_0}{1-y_0}\right)^{\frac{2^{6n+5}+1}{3}} \left(\frac{1+z_0}{1-z_0}\right)^{\frac{2^{6n+5}-2}{3}} + 1} \quad (37)$$

for $n \in \mathbb{N}_0$. Similarly, from the second equation of (2), we obtain

$$z_n = \frac{y_{n+1} - y_n}{1 - y_{n+1}y_n} \quad (38)$$

which yields

$$z_{6n} = 1 - \frac{2}{\left(\frac{1+x_0}{1-x_0}\right)^{\frac{2^{6n}-1}{3}} \left(\frac{1+y_0}{1-y_0}\right)^{\frac{2^{6n}-1}{3}} \left(\frac{1+z_0}{1-z_0}\right)^{\frac{2^{6n}+2}{3}} + 1}$$

$$z_{6n+1} = 1 - \frac{2}{\left(\frac{1+x_0}{1-x_0}\right)^{\frac{2^{6n+1}+1}{3}} \left(\frac{1+y_0}{1-y_0}\right)^{\frac{2^{6n+1}-2}{3}} \left(\frac{1+z_0}{1-z_0}\right)^{\frac{2^{6n+1}+1}{3}} + 1}$$

$$z_{6n+2} = 1 - \frac{2}{\left(\frac{1+x_0}{1-x_0}\right)^{\frac{2^{6n+2}-1}{3}} \left(\frac{1+y_0}{1-y_0}\right)^{\frac{2^{6n+2}-1}{3}} \left(\frac{1+z_0}{1-z_0}\right)^{\frac{2^{6n+2}-1}{3}} + 1}$$

$$z_{6n+3} = 1 - \frac{2}{\left(\frac{1+x_0}{1-x_0}\right)^{\frac{2^{6n+3}+1}{3}} \left(\frac{1+y_0}{1-y_0}\right)^{\frac{2^{6n+3}+1}{3}} \left(\frac{1+z_0}{1-z_0}\right)^{\frac{2^{6n+3}-2}{3}} + 1}$$

$$z_{6n+4} = 1 - \frac{2}{\left(\frac{1+x_0}{1-x_0}\right)^{\frac{2^{6n+4}-1}{3}} \left(\frac{1+y_0}{1-y_0}\right)^{\frac{2^{6n+4}+2}{3}} \left(\frac{1+z_0}{1-z_0}\right)^{\frac{2^{6n+4}-1}{3}} + 1}$$

$$z_{6n+5} = 1 - \frac{2}{\left(\frac{1+x_0}{1-x_0}\right)^{\frac{2^{6n+5}-2}{3}} \left(\frac{1+y_0}{1-y_0}\right)^{\frac{2^{6n+5}+1}{3}} \left(\frac{1+z_0}{1-z_0}\right)^{\frac{2^{6n+5}+1}{3}} + 1}$$

for $n \in \mathbb{N}_0$, along with (32)-(38).

The Forbidden Set Of The Initial Values

The above obtained formulas exactly determine the solutions of the system (2). But, some initial values yield undefinable solution of the system. Now, we give the set of such initial values by using the formulas. To do this, we use the changes of variables (4) along with the formula (18) and so get the closed formula of x_n as follows:

$$x_{6n+i} = 1 - \frac{2}{\left(\frac{1+x_0}{1-x_0}\right)^{\frac{2^{6n+i}}{3}} \left(\frac{1+y_0}{1-y_0}\right)^{\frac{2^{6n+i}}{3}} \left(\frac{1+z_0}{1-z_0}\right)^{\frac{2^{6n+i}}{3}} \left(\frac{1+x_i}{1-x_i}\right)^2 \left(\frac{1-y_{i+1}}{1+y_{i+1}}\right) + 1} \quad (39)$$

for $i = \overline{0,5}$ and $n \in \mathbb{N}_0$. It is easy to see that the formula (39) is undefinable, if

$$\left(\frac{1+x_0}{1-x_0}\right)^{\frac{2^{6n+i}}{3}} \left(\frac{1+y_0}{1-y_0}\right)^{\frac{2^{6n+i}}{3}} \left(\frac{1+z_0}{1-z_0}\right)^{\frac{2^{6n+i}}{3}} \left(\frac{1+x_i}{1-x_i}\right)^2 \left(\frac{1-y_{i+1}}{1+y_{i+1}}\right) = -1$$

for $i = \overline{0,5}$ and $n \in \mathbb{N}_0$. Similarly, we have the closed formulas of y_n and z_0 as follows

$$y_{6n+i} = 1 - \frac{2}{\left(\frac{1+x_0}{1-x_0}\right)^{\frac{2^{6n+i}}{3}} \left(\frac{1+y_0}{1-y_0}\right)^{\frac{2^{6n+i}}{3}} \left(\frac{1+z_0}{1-z_0}\right)^{\frac{2^{6n+i}}{3}} \left(\frac{1+y_i}{1-y_i}\right)^2 \left(\frac{1-z_{i+1}}{1+z_{i+1}}\right) + 1} \quad (40)$$

and

$$z_{6n+i} = 1 - \frac{2}{\left(\frac{1+x_0}{1-x_0}\right)^{\frac{2^{6n+i}}{3}} \left(\frac{1+y_0}{1-y_0}\right)^{\frac{2^{6n+i}}{3}} \left(\frac{1+z_0}{1-z_0}\right)^{\frac{2^{6n+i}}{3}} \left(\frac{1+z_i}{1-z_i}\right)^2 \left(\frac{1-x_{i+1}}{1+x_{i+1}}\right) + 1} \quad (41)$$

for $i = \overline{0,5}$ and $n \in \mathbb{N}_0$ respectively. Consequently, we find the forbidden set of the initial values x_0, y_0, z_0 as follows:

$$F = \left\{ \begin{array}{l} (x_0, y_0, z_0) \in \mathbb{R}^3 : \\ \left(\frac{1+x_0}{1-x_0} \right)^{\frac{\delta n+i}{3}} \left(\frac{1+y_0}{1-y_0} \right)^{\frac{\delta n+i}{3}} \left(\frac{1+z_0}{1-z_0} \right)^{\frac{\delta n+i}{3}} \left(\frac{1+x_i}{1-x_i} \right)^2 \left(\frac{1-y_{i+1}}{1+y_{i+1}} \right) = -1 \\ \left(\frac{1+x_0}{1-x_0} \right)^{\frac{\delta n+i}{3}} \left(\frac{1+y_0}{1-y_0} \right)^{\frac{\delta n+i}{3}} \left(\frac{1+z_0}{1-z_0} \right)^{\frac{\delta n+i}{3}} \left(\frac{1+y_i}{1-y_i} \right)^2 \left(\frac{1-z_{i+1}}{1+z_{i+1}} \right) = -1, \\ \left(\frac{1+x_0}{1-x_0} \right)^{\frac{\delta n+i}{3}} \left(\frac{1+y_0}{1-y_0} \right)^{\frac{\delta n+i}{3}} \left(\frac{1+z_0}{1-z_0} \right)^{\frac{\delta n+i}{3}} \left(\frac{1+z_i}{1-z_i} \right)^2 \left(\frac{1-x_{i+1}}{1+x_{i+1}} \right) = -1 \\ i = \overline{0,5}, n \in \mathbb{N}_0 \end{array} \right\}$$

Asymptotic Behavior Of The Well-Defined Solutions

We investigate the asymptotic behavior of the well-defined solutions of the system (2). The main result of this subsection is given by the following theorem.

Theorem

Suppose that the sequence $(x_n, y_n, z_n)_{n \geq 0}$ is a well-defined solution of the system (2), that is, $(x_0, y_0, z_0) \notin F$, Then,

$$\lim_{n \rightarrow \infty} (|x_n|, |y_n|, |z_n|) = (1, 1, 1).$$

Proof

To prove, we use the function $f(x) = \frac{1+x}{1-x}$ along with the formulas (39)-(41). Before proving, we can say that the points $(0,0,0)$, $(1,1,1)$ and $(-1,-1,-1)$ are equilibrium points of the system (2). That is, equilibrium solutions of the system (system) are given by $(x_n, y_n, z_n)_{n \geq 0} = (0,0,0)$, $(x_n, y_n, z_n)_{n \geq 0} = (1,1,1)$ and $(x_n, y_n, z_n)_{n \geq 0} = (-1,-1,-1)$, respectively. We here deal with nonequilibrium solutions of the system (2). We observe for the function f that if $x \in (-\infty, 0)$, then $f(x) \in (-1, 1)$; if $x \in (0, 1) \cup (1, \infty)$, then $f(x) \in (-\infty, -1) \cup (1, \infty)$, Hence, we prove the theorem in three cases:

(i) If $x_0, y_0, z_0 \in (-\infty, 0) \setminus F$, then $f(x_0), f(y_0), f(z_0) \in (-1, 1)$, Therefore, from the formulas (39)-(41), we get the limit

$$\lim_{n \rightarrow \infty} (x_n, y_n, z_n) = (1, 1, 1), \text{ as } n \rightarrow \infty,$$

(ii) If $x_0, y_0, z_0 \in (0, 1) \cup (1, \infty) \setminus F$, then $f(x_0), f(y_0), f(z_0) \in (-\infty, -1) \cup (1, \infty)$, Therefore, from the formulas (39)-(41), we get

$$\lim_{n \rightarrow \infty} (x_n, y_n, z_n) = (-1, -1, -1).$$

(iii) If $x_0, y_0, z_0 \in (-\infty, \infty) \setminus F$, then we can not say about the quantities $f(x_0)$, $f(y_0)$ and $f(z_0)$ exactly. But, the sequences

$$s_n^{(1)} = \left(\frac{1+x_0}{1-x_0} \right)^{\frac{\delta n+i}{3}} \left(\frac{1+y_0}{1-y_0} \right)^{\frac{\delta n+i}{3}} \left(\frac{1+z_0}{1-z_0} \right)^{\frac{\delta n+i}{3}} \left(\frac{1+x_i}{1-x_i} \right)^2 \left(\frac{1-y_{i+1}}{1+y_{i+1}} \right),$$

$$s_n^{(2)} = \left(\frac{1+x_0}{1-x_0} \right)^{\frac{\delta n+i}{3}} \left(\frac{1+y_0}{1-y_0} \right)^{\frac{\delta n+i}{3}} \left(\frac{1+z_0}{1-z_0} \right)^{\frac{\delta n+i}{3}} \left(\frac{1+y_i}{1-y_i} \right)^2 \left(\frac{1-z_{i+1}}{1+z_{i+1}} \right)$$

and

$$s_n^{(3)} = \left(\frac{1+x_0}{1-x_0} \right)^{\frac{\delta n+i}{3}} \left(\frac{1+y_0}{1-y_0} \right)^{\frac{\delta n+i}{3}} \left(\frac{1+z_0}{1-z_0} \right)^{\frac{\delta n+i}{3}} \left(\frac{1+z_i}{1-z_i} \right)^2 \left(\frac{1-x_{i+1}}{1+x_{i+1}} \right)$$

tend to either to 0 or to ∞ . So, by the formulas (39)-(41), we obtain the limit

$$\lim_{n \rightarrow \infty} (|x_n|, |y_n|, |z_n|) = (1, 1, 1).$$


which completes the proof.

References

1. R. Abu-Saris, C. Cinar and I. Yalcinkaya, On the asymptotic stability of , Computers & Mathematics with Applications, 56(5) (2008), 1172-1175.
2. I. Dekkar, N. Touafek and Y. Yazlik, Global stability of a third-order nonlinear system of difference equations with period-two coefficients, Revista de la real academia de ciencias exactas, físicas y naturales. Serie A. Matemáticas, Doi:10.1007/s13398-016-0297-z.
3. E.M. Elsayed, Qualitative behavior of a rational recursive sequence, Indagationes Mathematicae 19(2)(2008), 189-201.
4. E.M. Elsayed, Qualitative properties for a fourth order rational difference equation, Acta Applicandae Mathematicae 110(2)(2010), 589-604.
5. N. Haddad, N. Touafek and J. F. T. Rabago, Solution form of a higher-order system of difference equations and dynamical behavior of its special case, Mathematical Methods in the Applied Sciences, (2016), doi: 10.1002/mma.4248.
6. N. Haddad, N. Touafek and J. F. T. Rabago, Well-defined solutions of a system of difference equations, Journal of Applied Mathematics and Computing, (2017), Doi:10.1007/s12190-017-1081-8.
7. Y. Halim, N. Touafek and Y. Yazlik, Dynamic behavior of a second-order nonlinear rational difference equation, Turkish Journal of Mathematics 39(6)(2015), 1004-1018.
8. A. S. Kurbanli, C. Çinar and D. Şimşek, On the periodicity of solutions of the system of rational difference equations, Applied Mathematics, 2 (2011), 410-413.
9. S. Stevic, On some solvable systems of difference equations, Applied Mathematics and Computation, 218 (2012) 5010-5018.
10. S. Stevic, M. A. Alghamdi, N. Shahzad and D. A. Maturi, On a class of solvable difference equations, Abstract and Applied Analysis, Vol. 2013, Article ID 157943, 7 pages.

11. S. Stevic, Representation of solutions of bilinear difference equations in terms of generalized Fibonacci sequences, *Electronic Journal of Qualitative Theory of Differential Equations*, 2014, No. 67, (2014), 1–15.
12. S. Stevic, J. Diblík, B. Iricanin and Z. Šmarda, On a solvable system of rational difference equations, *Journal of Difference Equations and Applications*, 20(5–6)(2014): 811–825.
13. S. Stevic, M. A. Alghamdi, A. Alotaibi and E. M. Elsayed, Solvable product-type system of difference equations of second order, *Electronic Journal of Differential Equations*, 2015, No:169, (2015), 1–20.
14. S. Stevic, New class of solvable systems of difference equations, *Applied Mathematics Letters*, 63(2017), 137–144.
15. N. Taskara, K. Uslu and D. T. Tollu, The periodicity and solutions of the rational difference equation with periodic coefficients, *Computers & Mathematics with Applications*, 62 (2011), 1807–1813.
16. D. T. Tollu, Y. Yazlik and N. Taskara, On the solutions of two special types of Riccati difference equation via Fibonacci numbers, *Advances in Difference Equations*, 2013, 2013:174.
17. D. T. Tollu, Y. Yazlik and N. Taskara, On fourteen solvable systems of difference equations, *Applied Mathematics and Computation*, 233 (2014), 310–319.
18. N. Touafek, On a second order rational difference equation, *Hacettepe Journal of Mathematics and Statistics*, 41(6) (2012), 867–874.
19. I. Yalcinkaya, C. Cinar and D. Simsek, Global asymptotic stability of a system of difference equations, *Applicable Analysis*, 87(6)(2008), 677–687, DOI: 10.1080/00036810802140657.
20. I. Yalcinkaya, On the global asymptotic stability of a second-order system of difference equations, *Discrete Dynamics in Nature and Society*, vol. 2008, Article ID 860152, 12 pages, 2008. doi:10.1155/2008/860152.
21. I. Yalcinkaya, On the global asymptotic behavior of a system of two nonlinear difference equations, *Ars Combinatoria*, 95 (2010), 151–159.
22. I. Yalcinkaya and C. Cinar, Global asymptotic stability of two nonlinear difference equations, *Fasciculi Mathematici*, 43 (2010), 171–180.
23. I. Yalcinkaya and D. T. Tollu, Global behavior of a second-order system of difference equations, *Advanced Studies in Contemporary Mathematics*, 26(4)(2016), 653–667.
24. Y. Yazlik, On the solutions and behavior of rational difference equations, *Journal of Computational Analysis & Applications*, 17(3)(2014), 584–594.
25. Y. Yazlik, E. M. Elsayed and N. Taskara, On the behaviour of the solutions of difference equation systems, *Journal of Computational Analysis & Applications*, 16(5)(2014), 932–941.
26. Y. Yazlik, D. T. Tollu and N. Taskara, On the behaviour of solutions for some systems of difference equations, *Journal of Computational Analysis & Applications*, 18(1)(2015), 166–178.
27. Y. Yazlik, D. T. Tollu and N. Taskara, On the solutions of a max-type difference equation system, *Mathematical Methods in the Applied Sciences*, 38(17)(2015), 4388–4410.
28. Y. Yazlik, D. T. Tollu and N. Taskara, On the solutions of a three-dimensional system of difference equations, *Kuwait Journal of Science* 43(1)(2016), 95–111.
29. L. Xianyi and Z. Deming, Global asymptotic stability in a rational equation, *Journal of Difference Equations and Applications*, 9(9)(2003), 833–839.
30. L. Xianyi and Z. Deming, Two rational recursive sequences, *Computers & Mathematics with Applications*, 47 (2004) 1487–1494.
31. X. Wang and Z. Li, Global asymptotic stability for two kinds of higher order recursive sequences, *Journal of Difference Equations and Applications*, 22(10)(2016), 1542–1553, DOI: 10.1080/10236198.2016.1216111.

Impact of the Cascade Hydropower Construction (HPC) on Water Quality of the Seyhan River, Turkey

Mehmet Özçelik 

Suleyman Demirel University, Geological Engineering Department, Isparta, Turkey

ABSTRACT

Cascade hydropower construction is a series of hydroelectric power stations located on different sections of river. Hydropower constructions (HPC) in the environment have both positive and negative effect. HPCs are works that have brought enormous benefits to providing electric energy, water storage, controlling floods, irrigation, transportation, human communities, and areas of recreation, etc. These engineering works can be providing large economic development in the regions where they are located. But, dam construction converts the natural stream flow to human control. This paper summarizes the impacts of cascade HPC on water quality in the Seyhan River. Water quality data were collected and data were divided into two stage: before HPC (1995-2008) and during HPC construction (2009-2014). Dam construction negatively affects water quality based on water quality data. The analysis results were compared with maximum permissible limit values recommended by Turkish Water Pollution Control Regulation (TWPCR) standards. The contents of all chemical and physical parameters are higher before construction, and water pollution was observed at HPC construction site. Also, biological oxygen demand, chloride, nitrite nitrogen, total dissolved solids and total coliform bacteria were found to be above TWPCR.

Keywords:

Cascade Hydropower; Environmental degradation; Seyhan River; Water pollution; Water quality

Article History:

Received: 2017/03/24

Accepted: 2017/10/24

Online: 2018/04/06

Correspondence to: Mehmet Ozcelik,
Suleyman Demirel University, Geological
Engineering Department, 32260-Isparta,
TURKEY

E-Mail: ozcelikmehmet@sdu.edu.tr

Phone: +90 246 211 1327

INTRODUCTION

Cascade HPC is an important engineering measure in dealing with the relationship between water and human being [1-4]. Water quality characteristics may change engineering constructions in a river system [5]. Dam construction may cause considerable impacts on river hydrology, water resource allocation [6]. Some studies have shown that dams can cause disturbances in downstream flow [7], sediment accumulation in reservoirs [8], and fluctuations in water levels [9]. Dam construction is an important issue for water resource management and is essential for environmental protection and policy making [10-11]. Cascade HPC is a major driver of land cover changes and has a confirmed influence on landscape pattern variation, independent of construction type [12-14]. Changes in the local microclimate and river-water quality have been described to result from this

hydrological transformation [13]. Some researchers were studied on environmental deterioration of dam construction for different rivers in Turkey [16-19]. The Seyhan River Basin offers the people in the region various agricultural possibilities as dry farming, irrigated farming and livestock [20]. This basin has eight wildlife reserve sites, three wetlands and one nature conservation area. One of the wetlands (Lake Akyatan) has been declared as a Ramsar site (a wetland of international importance according to the Ramsar convention signed in 1971 by member countries) [21].

The present study summarizes the effect of cascade HPC on water quality in the Seyhan River basin during the 1995–2014 periods. Seyhan River basin has twenty two HPCs.

MATERIAL AND METHODS

Twelve HPCs were studied using site investigations from the Environmental Impact Assessment Reports (EIARs) for each dam. The EIARs contained information on geology, hydrogeology, water quality (physical, chemical and biological parameters), and dam characteristics. In order to assess the impact of cascade HPC on water quality, their process without interruption by dams must be known [22]. Water quality and quantity data were analyzed before construction (1995-2008) and during construction period (2009-2014). Data were obtained from the Feasibility Study Report for the HPC Stations and State Hydraulic Works Reports. Water quality data were evaluated in order to study the impact of HPCs on water quality of the Seyhan River.

Site Description

Seyhan River is the longest river in Turkey that flows into the Mediterranean Sea. The river is 560 km length and its source in Tahtalı Mountains (in Sivas and Kayseri provinces) to discharge in the Mediterranean. The river has

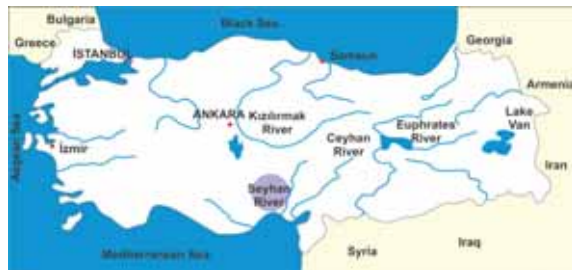


Figure 1. Location map of the Seyhan River

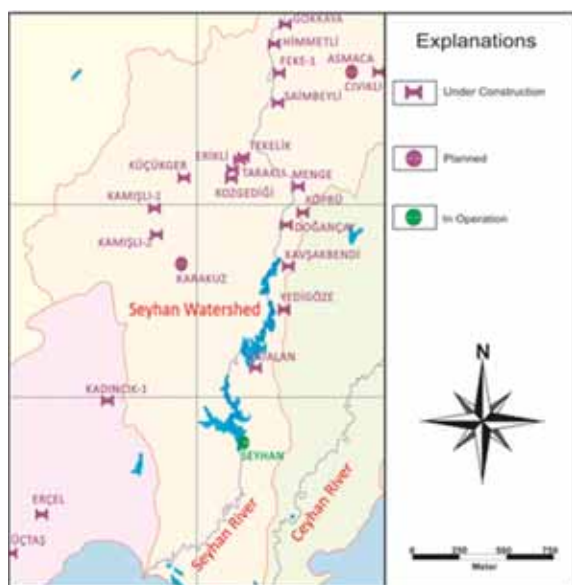


Figure 2. Location map of HPC on the Seyhan River hydrological watersheds

a 20731 km² catchment area. The climate in the basin is strongly influenced by topography. The northern part of the basin exhibits the characteristics of central Anatolian climate. Annual precipitation is around 350-500 mm. The highest precipitation is observed at highlands, particularly around the Aladag region with an annual quantity of 1500 mm. The region between the coastal zone and Taurus Mountains has a semi-arid meso-thermal Mediterranean climate with dry and hot summers, and rainy and warm winters [20]. The annual precipitation is approximately 700 mm at the south of the basin [23]. The basin hosts the most fertile and productive agricultural lands of Turkey (Fig. 1).

Seyhan River basin is very attractive for agricultural and industrial perspectives. Additionally, there are 18 cascade dams under construction (Data: State Hydraulic Works 2015) on the river for energy production and water supply (Fig. 2).

Water Quality

During the HPC phase, water mainly consumed in concrete production, washing of concrete aggregate, watering for dust suppression, and domestic purposes such as drinking, personnel usage. Water was used in concrete batching plant for washing of concrete aggregate and watering for dust suppression was supplied from the Seyhan River and its tributaries. Seyhan Dam Lake and Catalan Dam Lake now compensate for the lack of major water bodies in the region. In terms of hydrological features, Göksu, Zamantı and Pozantı streams are the main streams and they merge to form Seyhan River in the northern basin. Totally 18 cascade HPCs are under construction with the total installed capacity of 7869.9 Megawatt (MW) and the annual generating capacity of 3261.175 Gigawatthour (GWh) (Table 1).

Surface water samples for analysis were taken from the 12 different locations of Seyhan River before HPCs stage by EIE (General Directorate of Electrical Power Resources Survey and Development Administration). The coordinates of surface water sampling locations are given in Table 2. At the 12 water quality monitoring stations (Table 2), operated by EIE, collected samples were analyzed for temperature (°C) and pH value at site while collecting water sample. The collected water sample bottles were sealed at site and transported to the chemical lab for the detail analysis. The ion contents were measured by using titration techniques, flame photometer, spectrophotometer etc. The parameters such as pH, electrical conductivity (EC), Dissolved Oxygen (O₂), chloride (Cl⁻), Sulfate (SO₄), Chemical Oxygen Demand (COD), Biological Oxygen Demand (BOD), Nitrate Nitrogen (NO₃-N), Nitrite Nitrogen (NO₂-N), Iron (Fe), Mangan-

Table 1. Description of cascade dams [24-33] .

Dam Project Name	Province	Total Install Capacity (MW)	Total Energy (GWh/year)	Present stage
Asmaca	Adana	22	72	Master Planned
Cıvıklı	Adana	0.32	1.39	Under Const.
Catalan	Adana	169	596	In operation
Erikli	Adana	0.96	3.5	Under Const.
Kamışlı-1	Adana	4.3	20.34	Under Const.
Kamışlı-2	Adana	15.54	79.01	Under Const.
Karakuz	Adana	96	444	Master Planned
Kozgediği	Adana	2.03	6.98	Under Const.
Küçükger	Adana	0.89	6.98	Under Const.
Seyhan	Adana	54	350	In operation
Taraklı	Adana	0.56	1.87	Under Const.
Tekelik	Adana	0.56	1.74	Under Const.
Yamanlı I	Adana	22	100	Under Const.
Yamanlı II	Adana	78	308	Under Const.
Yamanlı III	Adana	30	119.116	Under Const.
Saimbeyli	Adana	8.76	237.940	Under Const.
Himmetli	Adana	27	106.159	Under Const.
Feke I	Adana	30	117	Under Const.
Feke II	Adana	70	225	Under Const.
Dogancay	Adana	49.17	190.15	Under Const.
Kavsakbendi	Adana	181.81	715	Under Const.
Yedigoze	Adana	300	949	Under Const.

nese (Mn), Alluminium (Al), TDS (Total Dissolved Solids) were analyzed for collected water samples. Statistics of the

13 mean parameters for 13 years before the construction stage (1995-2008) used in present study is given in Table 3.

Table 2. The coordinates of surface water sampling locations during the construction stage [24-33] .

Sample Location	Coordinates		
	UTM Zone	East	North
Cukurkisla Dam	37S	262762	4225971
Saimbeyli Dam	37S	243059	4199331
Gokkaya Dam	37S	244614	4194416
Yamanlı III Dam	37S	239228	4194879
Feke I Dam	36S	762380	4195577
Asmaca Dam	36S	754994	4190292
Feke II Dam	36S	751394	4181653
Kopru Dam	36S	736731	4166333
Kavsakbendi Dam	36S	723536	4160876
Menge Dam	36S	739670	4176823
Yedigoze Dam	36S	717046	4141802
Dogancay Dam	36S	714330	4161283

Table 3. Mean values of water quality characteristics before the construction stage (1995-2008) [46-48] .

Parameter	Unit	Mean values of 13 year
Temperature	C	12.5
pH	SU	6-9
Dissolved Oxygen (O ₂)	mgL ⁻²	3-5
Chloride (Cl)	mgL ⁻²	na
Sulfate (SO ₄)	mgL ⁻²	13.5
Chemical Oxygen Demand (COD)	mgL ⁻²	>70
Biological Oxygen Demand (BOD)	mgL ⁻²	0.6
Nitrate Nitrogen (NO ₃ -N)	mgL ⁻²	0.8
Nitrite Nitrogen (NO ₂ -N)	mgL ⁻²	>0.005
Iron (Fe)	mgL ⁻²	>0.5
Manganese (Mn)	mgL ⁻²	>3
Alluminium (Al)	mgL ⁻²	>1
TDS (Total Dissolved Solids)	mgL ⁻²	300

RESULTS AND DISCUSSION

Water quality in many large river waters has deteriorated significantly worldwide due to anthropogenic activities in the past two-three decades [34]. Pollution entering the rivers from agricultural runoff has caused significant increases in nutrient concentrations such as nitrogen (N) and phosphorus (P) [35-37]. It is also widely accepted that wastewaters from treatment plants supply significant amounts of P to rivers, particularly in populated urban areas [38]. Nutrient enrichment can result in excessive growth of aquatic plants, algae productivity and reductions in dissolved oxygen in rivers [39]. Turkey is still engaged in its “hydraulic mission” characterized by intensive dam and irrigation canal constructions [40] because water resource management is still at an early stage. The EU Water Framework Directive (WFD) is also likely to bring monetary support for improving the country’s water infrastructure and pollution prevention measures [41-42]. These characteristics make Turkey a country where, similarly to other rapidly developing economies [40] such as Brazil [43] and China [44], the nutrient cycle is increasingly controlled by human activities as opposed to natural processes [44]. The waters in the Seyhan River system provide many ecosystem functions including public drinking water supply, industrial water supply, irrigation water for agriculture, cultural and sporting activities such as swimming and fishing and conservation

value for wildlife habitats, fisheries and biodiversity [40].

The aim of this study was to examine to determine water quality of Seyhan River before and during HPC. According to TWPCR [45] Official Gazette, water quality of inland waters is classified into four groups as: high quality waters (Class I), moderate quality waters (Class II), polluted waters (Class III), and highly polluted waters (Class IV). There are 18 dams on the Seyhan River that are under construction for energy production and water supply. All the water quality data were collected and data were divided into two stage: before HPC period (1995-2008) and HPC period (2009-2014). The comparison of water quality characteristics of the HPCs during two stages, i.e. before and during HPC, enabled us to assess changes in the Seyhan River. Impact of HPC on Seyhan River water quality was analyzed, which were helpful for understanding the environmental features of the entire watershed. Based on the water quality data, HPCs are negatively affected water quality. According to Fig. 3, dissolved oxygen value is limited and total dissolved solids value is very high at the construction period (2009-2014).

The catchment has been monitored for flow and water quality at over 12 monitoring stations for 47 determinands. To determine sampling locations previous locations of Feasibility Study studies, locations determined during monitoring period were considered to facilitate comparati-

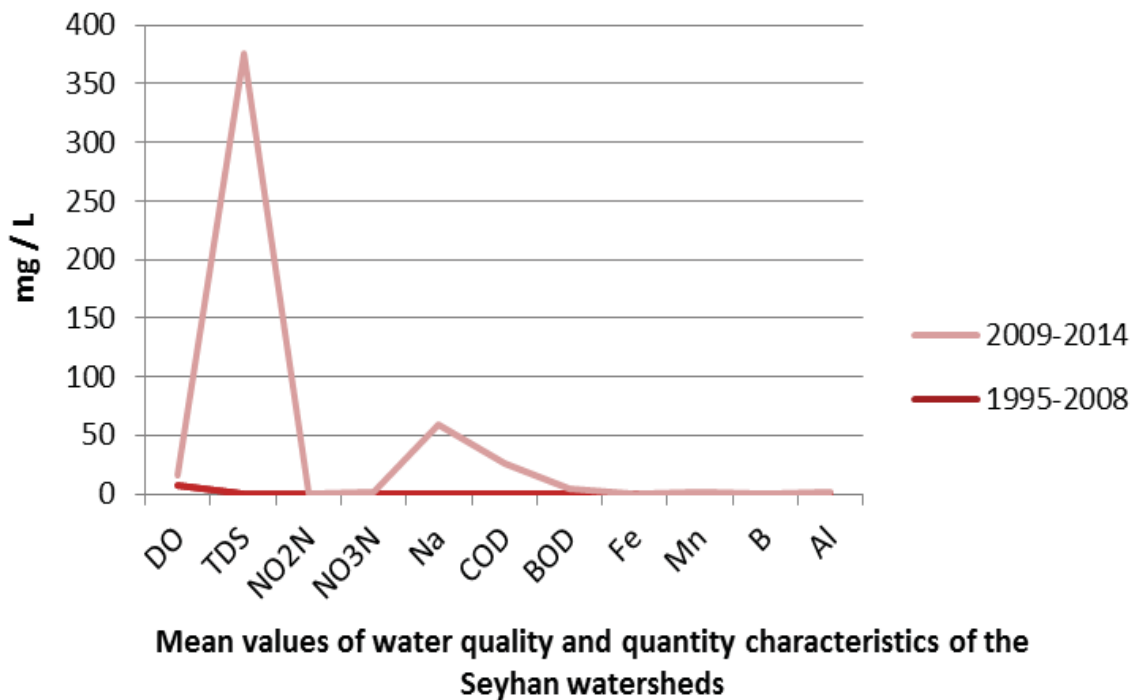


Figure 3. Location map of HPC on the Seyhan River hydrological watersheds

Table 4. Mean values of water quality characteristics during the construction (2009-2014) stage [24-33, 49].

Parameter	Unit	Surface water quality measurement locations											
		Cukurkisa Dam	Saimbeyli Dam	Gokkaya Dam	Yamanli III Dam	Fekeli Dam	Asmaca Dam	Fekeli II Dam	Kopru Dam	Kavakbendi Dam	Menge Dam	Yedigöze Dam	Dogançay Dam
Temperature	C	9.3	12.8	11.8	12.1	12.0	11.9	12.1	13.9	14.1	13.3	14.9	12.7
pH	SU	7.94	8.25	7.92	7.88	7.89	8.22	7.91	8.08	8.08	8.13	7.84	8.85
Dissolved Oxygen (O ₂)	mgL ⁻¹	9.38	10.55	9.99	9.88	9.91	10.22	9.37	9.26	9.60	8.94	8.27	9.72
Oxygen Saturation (% O ₂)	%	114.7	126.6	120.7	119.7	120.7	124.0	114.1	112.6	117.2	109.6	101.7	120.8
Chloride (Cl)	mgL ⁻¹	6.5	5.0	8.5	7.5	8.0	46.0	584.8	119.5	69.5	125.0	65.0	8.0
Sulfate (SO ₄)	mgL ⁻¹	13.5	18.6	93.5	92.4	88.1	56.3	117.1	79.7	54.3	84.5	45.3	4.9
TSS (Total Suspended Solids)*	mgL ⁻¹	9.2	< 1.0 **	108.4	359	144.1	< 1.0 **	< 1.0 **	24.8	100.4	6.8	2.4	< 1.0 **
Ammonium Nitrogen (NH ₄ -N)	mgL ⁻¹	< 0.15 **	0.18	< 0.15 **	< 0.15 **	< 0.15 **	0.17	0.36	0.59	< 0.15 **	< 0.15 **	< 0.15 **	0.19
Nitrate Nitrogen (NO ₃ -N)	mgL ⁻¹	1.40	1.10	0.96	0.94	0.99	0.55	0.92	0.78	0.92	0.77	0.98	0.23
Nitrite Nitrogen (NO ₂ -N)	mgL ⁻¹	0.012	0.025	0.004	0.006	0.008	< 0.002	0.009	0.005	0.005	0.005	< 0.002	0.004
Total Phosphorus (P)	mgL ⁻¹	< 0.3 **	< 0.3 **	0.5	3.5	1.7	< 0.3 **	< 0.3 **	< 0.3 **	< 0.3 **	< 0.3 **	< 0.3 **	< 0.3 **
TDS (Total Dissolved Solids)	mgL ⁻¹	10.0	260.0	326.0	304.0	238.0	382.0	1,324.0	326.0	292.0	370.0	366.0	302.0
Color	mgL ⁻¹ Pt/Co scale	7.1	7.6	7.1	7.6	8.2	7.1	6.0	4.9	6.5	4.3	6.5	6.0
Sodium (Na)	mgL ⁻¹	4.555	4.390	6.303	6.067	6.280	30.350	375.20	108.30	43.41	73.46	43.97	6.60
Chemical Oxygen Demand (COD)	mgL ⁻¹	< 20.0 **	< 20.0 **	20.3	31.9	64.2	< 20.0 **	34.9	< 20.0 **	< 20.0 **	< 20.0 **	< 20.0 **	< 20.0 **
Biological Oxygen Demand (BOD)	mgL ⁻¹	< 4.0 **	< 4.0 **	5.0	7.8	5.8	< 4.0 **	< 4.0 **	< 4.0 **	< 4.0 **	< 4.0 **	< 4.0 **	< 4.0 **
TOC (Total Organic Carbon)	mgL ⁻¹	1.1	1.0	0.9	1.6	0.9	1.0	1.0	0.7	0.9	0.9	1.2	1.0
Total Kjeldahl Nitrogen (TKN)	mgL ⁻¹	1.7	< 0.8	< 0.8	< 0.8	< 0.8	< 0.8	< 0.8	< 0.8	< 0.8	< 0.8	< 0.8	< 0.8
Oil and grease**	mgL ⁻¹	< 1.5 **	3.6	< 1.5 **	1.6	< 1.5 **	< 1.5 **	< 1.5 **	< 1.5 **	< 1.5 **	1.6	< 1.5 **	< 1.5 **
MBAS ((materials giving rxn with methyl blue.)	mgL ⁻¹	0.06	< 0.06 **	< 0.06 **	< 0.06 **	< 0.06 **	< 0.06 **	< 0.06 **	< 0.06 **	< 0.06 **	< 0.06 **	< 0.06 **	< 0.06 **
Phenols	mgL ⁻¹	< 0.002	< 0.002	< 0.002	< 0.002	< 0.002	< 0.002	< 0.002	< 0.002	< 0.002	< 0.002	< 0.002	< 0.002

Table 4. Mean values of water quality characteristics during the construction (2009-2014) stage [24-33, 49](continued).

Parameter	Unit	Surface water quality measurement locations											
		Cukurkisa Dam	Saimbeyli Dam	Gokkaya Dam	Yamami III Dam	Feki I Dam	Asmaca Dam	Feki II Dam	Kopru Dam	Kavakbendi Dam	Menge Dam	Yedigöze Dam	Dogançay Dam
Mineral Oils (C10-C40-Index)	mgL ⁻¹	< 0.1(LOD)	< 0.1(LOD)	< 0.1(LOD)	< 0.1(LOD)	< 0.1(LOD)	< 0.1(LOD)	< 0.1(LOD)	< 0.1(LOD)	< 0.1(LOD)	< 0.1(LOD)	< 0.1(LOD)	< 0.1(LOD)
Pesticides (30 parameters)***	SU	< 0.05x10 ⁻³	< 0.05x10 ⁻³	< 0.05x10 ⁻³	< 0.05x10 ⁻³	< 0.05x10 ⁻³	< 0.05x10 ⁻³	< 0.05x10 ⁻³	< 0.05x10 ⁻³	< 0.05x10 ⁻³	< 0.05x10 ⁻³	< 0.05x10 ⁻³	< 0.05x10 ⁻³
Mercury (Hg)	mgL ⁻¹	< 0.0030	< 0.0030	< 0.0030	< 0.0030	< 0.0030	< 0.0030	< 0.0030	< 0.0030	< 0.0030	< 0.0030	< 0.0030	< 0.0030
Cadmium (Cd)	mgL ⁻¹	0.0053	0.0056	0.0057	0.0053	0.0055	0.0054	0.0053	0.0056	0.0056	0.0054	0.0055	0.0055
Lead (Pb)	mgL ⁻¹	< 0.0100	< 0.0100	< 0.0100	< 0.0100	< 0.0100	< 0.0100	< 0.0100	< 0.0100	< 0.0100	< 0.0100	< 0.0100	< 0.0100
Arsenic (As)	mgL ⁻¹	< 0.0030	< 0.0030	0.0106	0.0098	0.0117	< 0.0030	0.0089	0.0056	0.0076	< 0.0030	< 0.0030	< 0.0030
Copper (Cu)	mgL ⁻¹	0.0705	0.0707	0.0792	0.0772	0.0980	0.0785	0.0698	0.0840	0.0550	0.0618	0.0696	0.0696
Chromium (Cr), Total	mgL ⁻¹	< 0.010	< 0.010	< 0.010	< 0.010	< 0.010	< 0.010	< 0.010	< 0.010	< 0.010	< 0.010	< 0.010	< 0.010
Chromium (Cr6+)	mgL ⁻¹	< 0.01	< 0.01	< 0.01	< 0.01	< 0.01	< 0.01	< 0.01	< 0.01	< 0.01	< 0.01	< 0.01	< 0.01
Cobalt (Co)	mgL ⁻¹	< 0.0030	< 0.0030	< 0.0030	0.0032	< 0.0030	< 0.0030	< 0.0030	< 0.0030	< 0.0030	< 0.0030	< 0.0030	< 0.0030
Nickel (Ni)	mgL ⁻¹	< 0.0100	< 0.0100	< 0.0100	< 0.0100	< 0.0100	< 0.0100	< 0.0100	< 0.0100	< 0.0100	< 0.0100	< 0.0100	< 0.0100
Zinc (Zn)	mgL ⁻¹	0.0324	0.0451	0.0500	0.0482	0.0671	0.0386	0.0293	0.0388	0.0352	0.0341	0.0347	0.0347
Total cyanide (CN ⁻)	mgL ⁻¹	< 0.002	< 0.002	< 0.002	< 0.002	< 0.002	< 0.002	< 0.002	< 0.002	< 0.002	< 0.002	< 0.002	< 0.002
Fluoride (F ⁻)	mgL ⁻¹	< 0.3	< 0.3	0.3	< 0.3	0.3	< 0.3	0.5	0.4	0.4	0.3	0.3	0.3
Free Chlorine (Cl ₂)	mgL ⁻¹	0.09	0.05	0.10	0.12	0.14	0.02	0.05	0.13	0.07	0.03	0.03	0.03
Sulphur (S ₂ ⁻)	mgL ⁻¹	< 1.0	< 1.0	< 1.0	< 1.0	< 1.0	< 1.0	< 1.0	< 1.0	< 1.0	< 1.0	< 1.0	< 1.0
Iron (Fe)	mgL ⁻¹	0.1844	0.1875	0.8178	2.8850	1.7290	0.1280	0.1509	0.2581	0.1773	0.1717	0.0859	0.0859
Manganese (Mn)	mgL ⁻¹	0.0255	0.5004	0.0614	0.1686	0.0617	0.0632	0.0333	0.2327	0.0385	0.2044	0.0125	0.0125
Baron (B)	mgL ⁻¹	0.2136	0.3098	0.3700	0.2373	0.1211	< 0.010	0.7306	< 0.0100	< 0.0100	< 0.0100	< 0.0100	< 0.0100
Selenium (Se)	mgL ⁻¹	0.0070	0.0070	0.0116	< 0.0050	0.0071	< 0.005	< 0.005	0.0054	0.0076	0.0093	0.0098	0.0098
Barium (Ba)	mgL ⁻¹	0.0554	0.0524	0.0610	0.0792	0.0618	0.0883	0.0570	0.0717	0.0671	0.0768	0.0196	0.0196
Aluminium (Al)	mgL ⁻¹	0.0812	0.0354	0.3092	0.6985	0.3726	0.0256	0.0490	0.1261	0.0822	0.0699	0.0274	0.0274
Fecal Coliform Bacteria	kob/100 mL	265	250	> 1000	> 1000	> 1000	160	210	>1000	70	100	88	88
Total Coliform Bacteria	kob/100 mL	840	820	> 1000	> 1000	> 1000	610	720	>1000	320	480	560	560

Table 4. Mean values of water quality characteristics during the construction (2009-2014) stage [24-33, 49](continued).

Parameter	Unit	Surface water quality measurement locations											
		Cukurkisa Dam	Saimbeyli Dam	Gokkaya Dam	Yamanli III Dam	Feki I Dam	Asmaca Dam	Feki II Dam	Kopru Dam	Kavsakbendi Dam	Menge Dam	Yedigöze Dam	Dogancay Dam
Radioactivity (Alfaactivity)	Bq/L	< 0.07	< 0.08	< 0.09	< 0.26	< 0.12	< 0.09	< 0.19	< 0.08	< 0.09	< 0.08	< 0.08	< 0.04
Beta Activity	Bq/L	0.08	0.09	0.10	0.24	0.14	0.07	0.71	0.15	0.12	0.17	0.09	0.06

LOD Limit of Detection

*TSS parameter cannot be compared with Table 4, in TWPCR because there is no classification in Table 5.

** It is observed that the detection limit for these analysis by using those methods are not possible to conduct other more precise measurement

*** 31 Pesticides parameters are analyzed by Agrolab Labor gruppe. In Table 5 of TWPCR, the limit value for pesticides is given as "Total Pesticides" but detailed list or explanation of these pesticides is not given. Therefore, it is determined that all 31 Pesticides are below "Class I" limit value since they are under " $0.05 \times 10^{-3} \mu\text{g/L}$ ".

ve analysis. Since 2014, samples at 12 HPC sites have been collected regularly in January, April, July and October. Thus in this study, I used data from 2009 to 2014 at these HPCs sites. Water quality parameters like temperature, pH, total dissolved solids, and electric conductivity were measured in the sites using, a thermometer, pH meter, conductivity meter and TDS meter respectively. For dissolved oxygen (DO), samples were collected into 300-ml plain glass bottles and the DO fixed using the azide modification of the Winkler's method. Samples for bacteriological analyses were collected into sterilized plain glass bottles. For oil, grease, and other parameters samples were collected in simple plastic bottles. All samples of 12 stations were stored in an icebox and transported to Encon Environmental Laboratory for analyses. The method used for water quality tests are presented below in the Table 4. Water quality determinands presented in this paper are dissolved oxygen (DO), biological oxygen demand (BOD), ammonium (NH₄-N), nitrite (NO₂-N), nitrate (NO₃-N) as well as major dissolved ions. Water quality classes were determined based on the water quality criteria presented in Table 5.

The variations in water quality parameters from 1995 to 2014 were evaluated and standardized. Some of the the major parameters (e.g. NO₂-N, NO₃-N, TDS, COD, BOD, Fe, Mn, B, Al) were evaluated corresponding to before construction (1995-2008) and during construction (2009-2014) periods. According to the Table 5, the water quality is listed from good quality to worse, respectively class I, II, III and IV. Since any water resource should satisfy all the parameters given for a category to be classified as within that water quality class. It can be stated that the quality class of surface water in Dogancay Dam and Yedigöze Dam are Class II water quality. Cukur Kışla, Gokkaya Dam, Kopru Dam, Kavsakbendi Dam are Class III and Saimbeyli Dam, Yamanli III Dam, Feki I Dam, Feki II Dam, and Menge Dam is Class IV water quality. Water quality is decreased depending on construction facilities (Fig. 3).

The obtained results have been compared with those from literature [50-53], and it can be observed a similarity with these, where the authors show high incidence of pathogenic and opportunistic bacteria isolated different water resources. The existing literature and observational data demonstrate that the cascading dams have led to a decline in the flood season water discharge and annual sediment flux within Turkey borders, reservoir aggradations, and degradation of water quality within the reservoirs. Furthermore, the dams have negatively affected the riverine aquatic biological communities and fish assemblages [54-55]. During the construction stage, due to the lack of dissolved oxygen, fish assemblages tried to get oxygen from the air in the Seyhan Dam reservoir (Fig.4a, b).

Table 5. Turkish Water Pollution Control Regulation [45].

Parameter	Water quality classes			
	I	II	III	IV
<i>General conditions</i>				
Temperature (°C)	≤ 25	≤ 30	≤ 30	> 30
Color	RES 436 nm: ≤ 1,5	RES 436 nm: 3	RES 436 nm: 4,3	RES 436 nm: >4,3
	RES 525 nm: ≤ 1,2	RES 525 nm: 2,4	RES 525 nm: 3,7	RES 525 nm: >3,7
	RES 620 nm: ≤ 0,8	RES 620 nm: 1,7	RES 620 nm: 2,5	RES 620 nm: >2,5
pH	6,5-8,5	6,5-8,5	6,0-9,0	< 6,0 veya > 9,0
Electrical conductivity (µS/cm)	< 400	1000	3000	> 3000
Oil and grease (mgL ⁻¹)	Floating liquids such as oil, tar, garbage and similar solid materials and foam can not be found.			-
<i>(A) Oxygenation Parameters</i>				
Oxygen Saturation (%) (b)	>90	70	40	< 40
Dissolved Oxygen (mgL ⁻¹)	> 8	6	3	< 3
Chemical Oxygen Demand (COD) (mgL ⁻¹)	< 25	50	70	> 70
Biological Oxygen Demand (BOD) (mgL ⁻¹)	< 4	8	20	> 20
<i>B) Nutrient (Nutrient Elements) Parameters</i>				
Ammonium Nitrogen (NH ₄ -N) mgL ⁻¹	< 0,2	1	2	> 2
Nitrate Nitrogen (NO ₃ -N) mgL ⁻¹	< 5	10	20	> 20
Nitrite Nitrogen (NO ₂ -N) mgL ⁻¹	< 0,01	0,06	0,12	> 0,3
Total Kjeldahl Nitrogen (TKN)	< 0,5	1,5	5	> 5
Total phosphorus (mg P/L)	< 0,03	0,16	0,65	> 0,65
<i>C) Trace Elements (Metals) and Inorganic Pollution Parameters</i>				
Aluminium (Al) (mgL ⁻¹)	≤ 0,3	≤ 0,3	1	> 1
Arsenic (µg/L)	≤ 20	50	100	> 100
Copper (µg/L)	≤ 20	50	200	> 200
Barium (µg/L)	≤ 1000	2000	2000	> 2000
Boron (µg/L)	≤ 1000	≤ 1000	≤ 1000	> 1000
Mercury (µg/L)	≤ 0,1	0,5	2	> 2
Zinc (µg/L)	≤ 200	500	2000	> 2000
Iron (µg/L)	≤ 300	1000	5000	> 5000
Florür (µg/L)	≤ 1000	1500	2000	> 2000
Cadmium (µg/L)	≤ 2	5	7	> 7
Cobalt (µg/L)	≤ 10	20	200	> 200
Chromium (µg Cr+6/L)	Not measurable	20	50	> 50
Chromium (total) (µg/L)	≤ 20	50	200	> 200
Lead (µg/L)	≤ 10	20	50	> 50
Manganese (µg Mn/L)	≤ 100	500	3000	> 3000
Nickel (µg/L)	≤ 20	50	200	> 200

Table 5. Turkish Water Pollution Control Regulation [45] (continued).

Parameter	Water quality classes			
	I	II	III	IV
<i>C) Trace Elements (Metals) and Inorganic Pollution Parameters(continued)</i>				
Selenium ($\mu\text{g Se/L}$)	≤ 10	≤ 10	20	> 20
Serbest klor ($\mu\text{g Cl}_2/\text{L}$)	≤ 10	≤ 10	50	> 50
Cyanide (total) ($\mu\text{g/L}$)	≤ 10	50	100	> 100
Sulphur ($\mu\text{g/L}$)	≤ 2	≤ 2	10	> 10
Dangerous materials	Dangerous substances and other pollutants not provided in this tablature will be evaluated from 1 January 2016 after the relevant country inventory (reference values) has been created.			
<i>D) Bacteriological Parameters</i>				
Fecal Coliform Bacteria (numbers/100 mL)	≤ 10	200	2000	> 2000
Total Coliform Bacteria (numbers/100 mL)	≤ 100	20000	100000	> 100000

- I. High quality waters
- II. Moderately quality waters
- III. Polluted waters
- IV. Extremely polluted water



Figure 4. The struggle for survival of fish assemblages

These photos are the best way to show the environmental impact of dams. Photos were taken on February 5, 2015.

CONCLUSION

As a one of active international research areas, studies on the impact of HPCs on water quality and environment deterioration is a new task in the basin management in Turkey. This study evaluated the impact of HPCs on wa-

ter quality in the Seyhan River. According to analyzing results, covering the period 1995-2008 was evaluated taking into consideration the major parameters. The quality of the water meets the requirements of Class I water specified in the TWPCR regulations. Evaluation of construction period (2009-2014), BOD, Cl, NO₂-N, TDS and Total Coliform Bacteria values were increased. This increase points out the pollution related to the construction activities. Water quality characteristics were evaluated results of the “Feasibility Study Report for the HPC Stations” and “the General Plan of the EIE”, from the different stations of the Seyhan River. The results show that the water can be used for municipal and agricultural purposes.

However, this paper is evaluated the impact of cascade dams on water quality at the before and during construction stage. Further analysis regarding environmental protection is needed. Issues such as intensive human activities on land use cannot be addressed here. In order to achieve a unified operation of HPCs for water quality, especially during water pollution events, an optimal monitoring program needs to be developed as well.

Consequently, these cascade HPCs have led to changes in the quality of the water. Careful planning and a design process that incorporate the public involvement are crucial to minimize the negative effects of the cascade HPC on the environment. When the appropriate mitigation measure are identified early in the planning and design process for cascade HPCs, they can be effectively and efficiently incorporated into the design, construction and operation of the project. Therefore, a long-term basin-wide terrestrial and

aquatic environment and ecosystem monitoring program consisting of permanent field monitoring stations and multiscale Environmental Sensor Networks should be planned and implemented to obtain additional geological, hydrological, ecological, meteorological and biodiversity information. The main recommendations are for planners, developers, financial institutions and environmental managers to reduce damage to a minimum through rational and intelligent solutions. They have negatively affected environmental deterioration and water quality.

ACKNOWLEDGMENTS



The author is deeply grateful to two anonymous reviewers and editors who helped improve the scientific content of this study. The author thank to the State Hydrolic Works and ENERJISA Group. The author also extends his appreciations to ENCON Environmental Engineering, CINAR Engineering; DOKAY Environmental Engineering; PRD Engineering; SELIN Const. engineers for providing the data.

References

- Hu WW, Wang GX, Deng W, Li SN. The influence of dams on ecohydrological conditions in the Huaihe River basin, China. *Ecological Eng.* 33(3-4) (2008) 233-241.
- Burke M, Jorde K, Buffington JM. Application of a hierarchical framework for assessing environmental impacts of dam operation: Changes in streamflow, bed mobility and recruitment of riparian trees in a western North American river. *J Environ Manage.* 90 (2009) 224-236.
- Zhao Q, Liu S, Deng L, Dong S, Yang J, Wang C. The effects of dam construction and precipitation variability on hydrologic alteration in the Lancang River basin of southwest China. *Stoch Environ Res Risk Assess.* 26 (2012) 993-1011.
- Morimoto R. Incorporating socio-environmental considerations into project assessment models using multi-criteria analysis: A case study of Sri Lankan hydropower projects. *Energy Policy* 59 (2013) 643-653.
- Huang WR, Foo S Neural network modeling of salinity variation in Apalachicola River. *Water Res.* 36 (2002) 356-362.fdf
- Tealdi S, Camporeale C, Ridolfi L. Modeling the impact of river damming on riparian vegetation. *J Hydrology* 396(3-4) (2011) 302-312.
- Elhatip H, Hınıs MA, Gulbahar N. Evaluation of the water quality at Tahtali Dam watershed in Izmir -Turkey by means of statistical methodology. *Stoch Environ Res Risk Assess.* 22(3) (2008) 391-400.
- Snyder NP, Rubin DM, Alpers CN, Childs JR, Curtis JA, Flint LE, Wright SA. Estimating accumulation rates and physical properties of sediment behind a dam: Eglebright Lake, Yuba River, northern California. *Water Res Research* 40(11) (2004) W11301.
- Lee JY, Choi YK, Kim HS, Yun ST. Hydrologic characteristics of a large rockfill dam: implications for water leakage. *Eng Geol.* 80 (1-2) (2005) 43-59.
- Bunkei M, Ming X, Takehiko F. Characterizing the changes in landscape structure in the Lake Kasumigaura Basin, Japan using a high-quality GIS dataset. *Landscape Urban Plan.* 78 (2006) 241-250.
- Chon, H., Vassilev, A., DePamphilis, M.L., Zhao, Y., Zhang, J., Burgers, P.M., Crouch, R.J., and Cerritelli, S.M. Contributions of the two accessory subunits, RNASEH2B and RNASEH2C, to the activity and properties of the human RNase H2 complex. *Nucleic Acids Res.* 37 (2009) 96-110.
- Hooke, J.M., Human impacts on fluvial systems in the Mediterranean region. *Geomorphology* 79(3-4) (2006) 311-335.
- Ouyang W, Skidmore AK, Hao FH, Toxopeus AG, Abkar A. Accumulated effects on landscape pattern by hydroelectric cascade exploitation in the Yellow River basin 1976 to 2006. *Landscape Urban Plan.* 93(3-4) (2009) 163-171.
- Liu S, Zhao Q, Wen M, Deng L, Dong S, Wang C. Assessing the impact of hydroelectric project construction on the ecological integrity of the Nuozhadu Nature Reserve, southwest China. *Stoch Environ Res Risk Assess.* 27 (2013) 1709-1718.
- Ouyang W, Hao F, Song K, Zhang X. Cascade dam-induced hydrological disturbance and environmental impact in the upper stream of the Yellow River. *Water Res Manag.* 25 (2011) 913-927.
- Akkoyunlu A. Water quality assessment of Omerli Dam reservoir (Istanbul, Turkey). *Freseneus Environ Bull* 11 (2002) 208-217.
- Kurunc A, Yurekli K, Okman C. Effects of Kilickaya Dam on concentration and load values of water quality constituents in Kelkit Stream in Turkey. *J Hydrology* 317 (2006) 17-30.
- Tahmicioglu MS, Anul N, Ekmekci F, Durmus N. Positive and negative impact of dams on the environment, International Congress on River Basin Management, Turkey, Chapter 2, 759-769, 2007.
- Tanrıverdi C, Alp A, Demirkıran AR, Uçkardes F. Assessment of surface water quality of the Ceyhan River basin, Turkey. *Environ Monit Assess.* 167 (2010) 175-184.
- Golge M, Yenilmez F, Aksoy A. Development of pollution indices for the middle section of the Lower Seyhan Basin (Turkey). *Ecological Indicator* 29 (2013) 6-17.
- RAMSAR (2012) The Ramsar Sites Database. Database/Searchforsites/tabid/765/Default.aspx. <http://ramsar.wetlands.org/> (Accessed 1 Nov 2016).
- Zhang Y, Xia J, Liang T, Shao Q. Impact of water projects on river flow regimes and water quality in Huai River basin. *Water Res Manag.* 24 (2009) 889-908.
- Fujihara Y, Tanaka K, Watanabe T, Nagano T, Kojiri T. Assessing the impacts of climate change on the water resources of the Seyhan River Basin in Turkey: Use of dynamically downscaled data for hydrologic simulations. *J Hydrology* 353 (2008) 33-48.
- Dokay Environmental Engineering Co. Yedigoze Dam, HEPP and Quarries Project Final EIA Report, Ankara, 2007.
- Cinar Engineering Co. Yamanli III HEPP EIA Report, Ankara, 2008.
- Prd Construction Co. Feke II Dam and HEPP, EIA Report, Ankara, 2008.
- Cinar Engineering Co. Feke I Weir and HEPP Project Information Report, Ankara, 2009.
- Dokay Environmental Engineering Co. Kavsakbendi Dam and HEPP Capacity Increase Final EIA Report, Ankara, 2009a.
- Dokay Environmental Engineering Co. Yamanli II Weir, HEPP and Quarries Final EIA Report, Ankara, 2009b.
- Dokay Environmental Engineering Co. Kopru Dam and HEPP Final EIA Report, Ankara, 2009c.
- Dokay Environmental Engineering Co. Menge Dam and HEPP Final EIA Report, Ankara, 2009d.
- Selin Const. Co. Dogancay Weir and HEPP, Final EIA Report, Ankara, 2009.

33. Selin Const. Co. Saimbeyli Weir and HEPP, EIA Introduction Report, Ankara, 2010.
34. Ferrier RC, Edwards AC, Hirst D, Littlewood IG, Watts CD, Morris R. Water Quality of Scottish Rivers: Spatial and Temporal Trends. *Sci Total Environ.* 265(1-3) (2001) 327-342.
35. Neal C, Jarvie HP, Love A, Neal M, Wickham H, Harman S. Water quality along a river continuum subject to point and diffuse sources. *J Hydrology* 350(3-4) (2008) 154-165.
36. Royer TV, David MB, Gentry LE. Timing of riverine export of nitrate and phosphorus from agricultural watersheds in ILLINOIS: Implications for reducing nutrient loading to the Mississippi River. *Environ Sci Tech.* 40(13) (2006) 4126-4131.
37. Withers PJA, Lord EI. Agricultural nutrient inputs to rivers and groundwaters in the UK: Policy, Environmental management and research needs. *Sci Total Environ.* 282(1) (2002) 9-24.
38. Jarvie HP, Neal C, Withers PJA. Sewage-Effluent phosphorus: A greater risk to river eutrophication than agricultural phosphorus? *Sci Total Environ.* 360(1-3) (2006) 246-253.
39. Whitehead PG, Johnes PJ, Butterfield D. Steady state and dynamic modelling of nitrogen in the River Kennet: Impacts of land use change since the 1930s, *Sci Total Environ.* 282(2002) 417-434.
40. Jin L, Whitehead P, Hadjikakou M. A study of the Yesilirmak River catchment in Northern Turkey: Spatial patterns and temporal trends in water quality. *J Environ Protec* 4(2013) 104-120.
41. Kibaroglu A. Analysis of the integrated water resources management approach: Turkey-EU water relations as a case study, Paper presented in BALWOIS 2008 (Balkan Water Observation and Information Systems for Balkan Countries), Ohrid, 27-31 May 2008.
42. Gurluk S. Turkey's challenges of river basin management and implementation of the European Union Water Framework Directive, Paper presented in BALWOIS 2008 (Balkan Water Observation and Information Systems for Balkan countries). Ohrid, 27-31 May 2008.
43. Filoso S, Martinelli LA, Howarth RW, Boyer EW, Dentener F. Human activities changing the nitrogen cycle in Brazil. *Biogeochem* 79(1-2) (2006) 61-89.
44. Xia J, Cheng S, Hao X, Xia R, Liu X. Potential impacts and challenges of climate change on water quality and ecosystem: case studies in representative rivers in China. *J Resour Ecology* 1(1) (2010) 31-35.
45. Turkish Water Pollution Control Regulation, Official Gazette No. 25687 dated December 31, 2004 and revised in Official Gazette No. 28257 dated October 30, 2012.
46. General Directorate of Electrical Power Resources Survey and Development Administration (EIE) Water Discharges, Ankara, 305 pp. 2010.
47. Devlet Su Isleri Genel Müdürlüğü, Seyhan Havzası Master Plan Raporu, DSI 6 Bölge Müdürlüğü, Adana, 2014.
48. Devlet Su İşleri Genel Müdürlüğü, Adana DSI 6 Bölge Müdürlüğü ve Kayseri DSI 12 Bölge Müdürlüğü Takdim Raporları, 2015.
49. TÜBİTAK (The Scientific & Technical Research Council of Turkey) MAM ÇEVRE ENSTİTÜSÜ, Havza koruma eylem planları - Seyhan Havzası. 459 pp. http://www.cygm.gov.tr/CYGM/Files/Guncelbelgeler/HAVZA_FINAL/Seyhan/Seyhan_Havzasi.pdf
50. Kinge CW, Mbewe M. Bacterial contamination levels in river catchments of the North West Province, South Africa: Public health implications. *Afr J Microbiol Res.* 6(7) (2012) 1370 - 1375.
51. Niewolak S, Opieka A. Potentially pathogenic microorganisms in water and bottom sediments in the Czarna Hańcza River. *Pol J Environ Stud.* 9 (2000) 183-194.
52. Orozco LN, Felix EA, Ciapara IH, Flores RJ, Cano R. Pathogenic and non-pathogenic *Vibrio* species in aquaculture shrimp ponds. *Rev Microbiol.* 49(3-4) (2007) 60-67.
53. Obi CL, Bessong PO, Momba MNB, Potgieter N, Samie A, Igumbor IE. Profiles of antibiotic susceptibilities of bacterial isolates and physico-chemical quality of water supply in rural vanda communities, South Africa. *Water SA* 30(4) (2004) 515-520.
54. Bai J, Xiao R, Cui B, Zhang K, Wang Q, Liu X, Gao H, Huang L. Assessment of heavy metal pollution in wetland soils from the young and old reclaimed regions in the Pearl River Estuary, South China. *Environ Poll.* 159 (2011) 824-917.
55. Wang QG, Du YH, Su Y, Chen KQ. Environmental impact post-assessment of dam and reservoir projects: A review. *Procedia Environ Sci.* 13 (2012) 1439-1443.

Preparation of Silicon-Antimony Based Anode Materials for Lithium-Ion Batteries

Asuman Celik Kucuk  Samet Ozturk  Barış Cem Alpaya, Mine Yorulmaz

Marmara University, Department of Metallurgical and Materials Engineering, Istanbul, Turkey

ABSTRACT

In this study, SixSb immiscible composite blend as anode materials have been synthesized using micron-sized silicon and antimony particles in different compositions through chemical reduction-mechanical alloying method (CR-MA). The obtained microstructures have been investigated by X-ray diffraction (XRD) and Scanning Electron Microscopy (SEM) with Energy Dispersive X-Ray analysis (EDX). Spectroscopic characterizations of the composite materials showed that a traditional intermetallic compound could not be achieved. However a novel immiscible composite blend system have been developed. One of the newly prepared composite materials, Si^{0.65}Sb, exhibits an initial capacity of 790 mAh g⁻¹ and a good cyclic stability compared to the pure silicon. The battery performance results of the micron-sized Si^{0.65}Sb blend system have been compared with the commercially used graphite and the nano-sized Si/Sb alloy systems. The cycling stability of the micron-sized Si^{0.65}Sb blend system showed an improvement compared to nano-sized Si/Sb alloy systems. Moreover its specific capacity is slightly higher than the commercial graphite anode material. These results portray the importance of micron sized Si/Sb system in large-scale applications due to its low cost.

Article History:

Received: 2017/04/28

Accepted: 2017/12/04

Online: 2018/04/06

Correspondence to: Asuman Çelik Küçük
Marmara University, Department of
Metallurgical and Materials Engineering,
34722, İstanbul, Turkey
Tel: +90 (216) 348-02-92
Fax: +90 (216) 347-28-59
E-Mail: asuman.celik@marmara.edu.tr

Keywords: Silicon-Antimony based materials, Negative electrode, Li-ion battery

INTRODUCTION

The increased necessity for longer lasting and higher capacity batteries have led to the rapid development of lithium-ion batteries and their widespread use. This demand forces researchers to develop anode materials that could provide higher capacity along the numerous cycles [1]. Graphite, which is a commonly used anode material, has just 372 mAh g⁻¹ initial theoretical capacity [2]. On the other hand, silicon is a promising anode material due to its high theoretical specific capacitance (4200 mAh g⁻¹). However Si faces drastic volume change up to 300% during lithiation and delithiation processes. Thus, silicon cannot retain its integrity during incessant battery cycles and this creates dead weight (inactive material) in battery [3]. To increase the cycling performance of Si-based anode materials, several approaches have been proposed in the literature such as; (1) developing nanostructured Si-based materials [4,5], (2) synthesis of Si-based alloy [6,7], and (3) preparation of amorphous silicon materials [8,9].

Among these, the approach of Si-based alloy

system is comparable advantageous as it has a potential to prevent disintegration that occurs due to the volume expansion of silicon during the charge/discharge process. Therefore, several Si based alloy systems such as Si/C, Si/Ti, Si/Ni, Si/Fe [10-19] have been studied so far. Recently, Xinpeng Ai et al. developed a FeSi₂/Si nanocomposite that exhibits a high Li storage capacity of ~1010 mAh g⁻¹ and an excellent cyclability with 94% capacity retention after 200 cycles [18]. Martin Winter et al. synthesized porous NiSi₂/Si/carbon composites [16], which resulted in good stability and high capacity.

Antimony (Sb) takes more attention due to great cycling stability even after numerous cycles [20]. However, the initial theoretical capacity of Sb is just 650 mAh g⁻¹. Therefore, in the Si/Sb alloy system, the high capacity of silicon can be combined with the high cyclic stability of antimony. According to our knowledge just one group, which is Jingwei Wang et al., have developed Si/Sb alloy system using nano-sized Si and Sb particles [21]. They claimed that SixSb immiscible alloy system have been succeeded by the chemical reduction-mechanical

alloying method and found specific capacity of 1194 mAh g⁻¹. However after seven cycles, it drops to 596.4 mAh g⁻¹.

The motivation of this work is to obtain high capacity compared to the graphite anode material and cycling stability compared to the nano-sized Si/Sb alloy system. Therefore, alternative to nano-sized Si/Sb alloy system, micron-sized silicon and antimony particles have been utilized to develop Si/Sb alloy system by chemical reduction-mechanical alloying (CR-MA) method. However XRD, SEM-EDX studies displayed that alloying of Si and Sb in micron size cannot be succeeded but stable immiscible blend system can be. The battery performance results obtained from the micron-sized Si_{0.65}Sb blend system have been compared to graphite and the nano-sized Si/Sb alloy system. It has been found that there is an improvement in cycling stability compared to nano-sized Si/Sb alloy system and in specific capacity compared to graphite anode material.

EXPERIMENTAL

Materials: Silicon powder (-100 mesh, 99.9% purity, density 2.329 g/cm³), Antimony powder (-100 mesh, 99.5 % purity, density 6.697 g/cm³), and absolute ethanol were purchased from Aldrich Chemical Co. Inc. and used as received. For battery tests; acetylene black, polyvinylidene fluoride (PVDF), and 1-methyl-2-pyrrolidinone (NMP) were kindly donated by Aldrich Chemical Co. Inc.

Preparation of Alloy: To obtain Si and Sb based alloy, chemical reduction and mechanical alloying method was used. Si and Sb mixed at different molar ratios into the attrition milling, while adding ethanol (300 ml) as milling control agents, charged with nitrogen as a protective gas. Samples were dried in a vacuum oven at 120 °C after milling process. Molar ratios, milling and drying times are shown in the Table 1.

Spectroscopic Characterization: XRD was performed using a Bruker AXS X-ray generator and diffractometer with Cu K α radiation. The instrument operates at room temperature, with θ -2 θ optics, and is equipped with a 3 kW generator and Cu K α X-ray tubes. The system is interfaced with Visual XRD and Traces version 6.6.10 software designed for graphical processing and manipulation. The tube voltage and current were set at 40 kV and 25 mA, respectively.

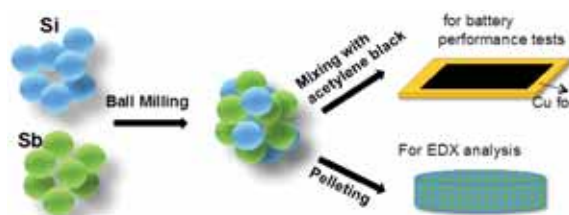


Figure 1. The concept and formation process of micron-sized Si/Sb blend system

Sample morphologies were investigated using a JEOL JEM-3000 (30 kV) SEM. Some of the higher resolution SEM images in this research work were obtained by using a field emission scanning electron microscope (FE-SEM), a JEOL JSM-7500FA. The elemental analysis of some particles was performed with energy dispersive X-ray spectroscopy (EDX).

Cell assembly and measurement: The electrode was prepared by mixing 70 wt% active materials, 10 wt% acetylene black and 20 wt% polyvinylidene fluoride (PVDF) binder in 1-methyl-2-pyrrolidinone (NMP) to form slurry, which was then spread onto a copper grid. Galvanostatic cycling measurements were performed with a classical two-electrode Swagelok-typeTM cell at a C/10 current density. Half-cell Li ion battery for test was assembled inside in an argon filled glove box to evaluate the electrochemical characteristics of Si_{0.65}Sb alloy blend system. Ethylene carbonate (EC) and dimethyl carbonate (DMC) (EC/DEC: 1/1, V/V) was used as electrolyte and a porous polyethylene (PE) membrane was used as a separator. The cell was galvanostatically charged (Li⁺ insertion) and discharged (Li⁺ extraction) in the voltage range of 0.01–2.0 V vs Li/Li⁺ at different current densities at room temperature using VMP3 Biologic battery test system.

RESULTS AND DISCUSSION

Micron sized Si and Sb particles have been utilized to obtain Si/Sb alloy systems by CR-MA method. Si and Sb have been mixed at different molar ratios into the attrition milling, and obtained three different components. After milling process, samples have been dried in a vacuum oven at 120 °C. XRD, SEM-EDS and battery performance tests have been done for each Si_xSb blend system (Fig. 1).

XRD has been used to illuminate the microstructure of Si/Sb systems (Fig. 2). In the Fig. 2, the diffraction peaks of a series Si–Sb are attributed to Si and Sb phases. It has not

Table 1. Conditions of chemical reduction and mechanical alloying method and ratios of Si and Sb amounts in alloy samples

	Si	Sb	Drying time (h)	Milling time (h)
Experiment I/Si _{0.65} Sb	0.05 mol	0.08 mol	10	20
Experiment II/Si _{0.85} Sb	0.06 mol	0.07 mol	10	20
Experiment III/SiSb	0.07 mol	0.07 mol	10	20

been observed any shift of Si and Sb peaks, meaning that traditional intermetallic compounds cannot be occurred. Jingwei Wang et al. have obtained same XRD result with that obtained in this study. However they investigated the peaks characteristic of Si-Sb immiscible alloy and observed an enhancement with the increasing Si contents, stating that an appropriate addition of Si contributes to the formation of Si-Sb immiscible alloy material [21]. However in this study, there is no relation between the peak areas of the elements in the X-ray diffraction spectroscopy and those of mixing ratios. Therefore, it has been concluded that alloying cannot be achieved using micron sized (100 mesh) silicone and antimony particles.

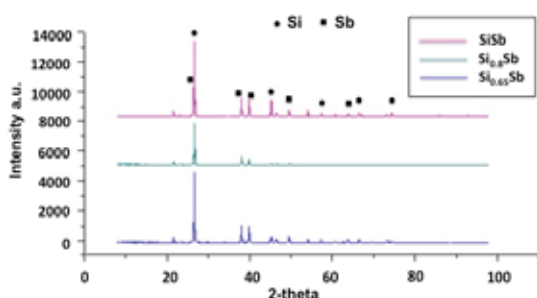


Figure 2. XRD patterns of Si-Sb immiscible blend system

Despite the preparation of three different samples, further experiments have been carried out for one specimen which is $\text{Si}_{0.65}\text{Sb}$ immiscible composite blend system.

The SEM image of $\text{Si}_{0.65}\text{Sb}$ immiscible blend system is showed in Fig.3. As schematically depicted in Fig. 3, the sample is formed by tiny irregular particles and the particles aggregated into homogenous secondary particles, which are uniformly distributed without distinct agglomeration.

An energy dispersive X-Ray analysis (EDX) is utilized to provide elemental identification and quantitative compositional information. Therefore further microstructure conformation has been done by SEM-EDX analysis (Fig. 4). The mixing ratio of Si:Sb in the $\text{Si}_{0.65}\text{Sb}$ immiscible blend system

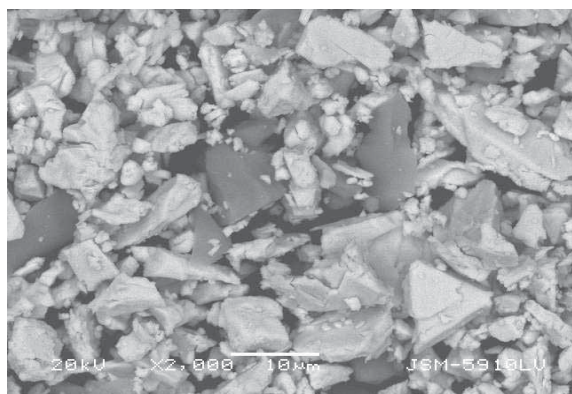


Figure 3. SEM image of $\text{Si}_{0.65}\text{Sb}$ immiscible blend materials.

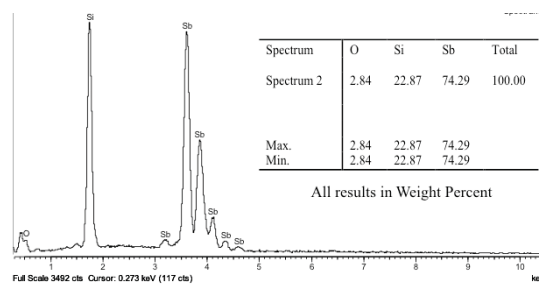


Figure 4. SEM-EDX result for $\text{Si}_{0.65}\text{Sb}$ blend system.

is 0.15 in weight. When the SEM-EDX analysis has been carried out for $\text{Si}_{0.65}\text{Sb}$, the normalised concentration ratio of the elements (Si:Sb) in weight percent is found to be 0.31. It has been clearly seen that no any relation between analysis results of the SEM-EDX and mixing ratios of Si and Sb powders. Aforementioned results obtained from XRD and EDX display that alloying of micron-sized Si and Sb particles cannot be achieved.

The prepared half-cell was galvanostatically charged (Li^+ insertion) and discharged (Li^+ extraction) in the voltage range of 0.01–2.0 V vs Li/Li^+ to evaluate the electrochemical characteristics of $\text{Si}_{0.65}\text{Sb}$ alloy blend system at a C/10 (Fig. 5). Fig. 5 depicts the cycle performance of $\text{Si}_{0.65}\text{Sb}$ alloy anode material, providing a direct evidence of the good lithium storage performance due to the proper silicon contents.

The initial discharge capacity of the micron-sized $\text{Si}_{0.65}\text{Sb}$ anode material, which is obtained using the CRMA method, is 790 mAh g^{-1} and the discharge capacity at the end of the 7th cycle is maintaining 520 mAh g^{-1} (Fig. 6). Although the initial specific capacity of the nano-sized Si/Sb alloy system is about 1194 mAh g^{-1} , its capacity drop to 596.4 mAh g^{-1} which means cycling stability of nano-sized Si/Sb alloy system is lower than micron-sized $\text{Si}_{0.65}\text{Sb}$ anode material. On the other hand, when the capacity values of the obtained $\text{Si}_{0.65}\text{Sb}$ anode material are compared with those of the conventional graphite anode material, it has been clearly seen that specific capacity of $\text{Si}_{0.65}\text{Sb}$ is higher than graphite anode material (Table 2)

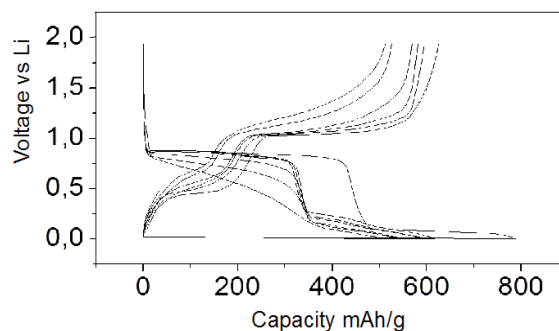


Figure 5. Initial charge-discharge curves of $\text{Si}_{0.65}\text{Sb}$ alloy anode material.

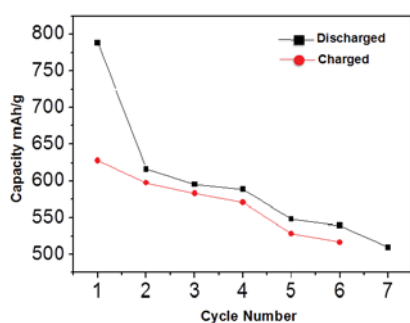


Figure 6. Cycle performance of Si_{0.65}Sb anode material in the potential range of 2.0 V – 0.01 V at a scan rate of 0.05 mV s⁻¹ (vs. Li/Li+).

Table 2. Capacity comparison of Si_{0.65}Sb anode material with the literature.

Anode Materials	1 st cycling	7 th cycling
Graphite [25]	372 mAh g ⁻¹	350 mAh g ⁻¹
Silicium [26]	4200 mAh g ⁻¹	1580 mAh g ⁻¹
Antimony [27]	650 mAh g ⁻¹	200 mAh g ⁻¹
Nano-sized Si _{0.65} Sb alloy [21]	1194 mAh g ⁻¹	596.4 mAh g ⁻¹
Micron-sized Si _{0.65} Sb anode material [this study]	790 mAh g ⁻¹	520 mAh g ⁻¹

CONCLUSION

Stable immiscible blend systems composed of micron-sized silicon and antimony particles have been developed using CR-MA method. Si^{0.65}Sb blend system exhibits initial capacity of 790 mAh g⁻¹ and a superior capacity of 520 mAh g⁻¹ after 7 cycles. Although the blend system composes of micron size Si and Sb particles, which means interaction occurs in micron distances, the results are promising when compared to the nano-sized Si/Sb alloy system or to commercial using graphite.

ACKNOWLEDGEMENT

This work was financially supported by Marmara University scientific research projects FEN-A-150513-0173, FEN-E-120314-0064 and partially by the Scientific and Technological Research Council Of Turkey (TUBITAK). We thank Marmara University Scientific Research Project Unit (BABKO).

REFERENCES

- Goodenough, J.B.; Park, K.S.; J. Am. Chem. Soc 2013, 135, 1167-1176
- Horiba, T.; Maeshima, T.; Matsumura, Koseki, M.; Arai, J.; Muranaka, Y., Journal of Power Sources 2005, 146, 107-110.
- Johnson, B. A.; White, R. E., Journal of Power Sources 1998, 70, 48-54.
- Chan C.K., Peng H., Liu G., Mcllwraith K., Zhang X.F., Huggins R.A., Nat Nanotechnol 2008, 3, 31 - 35.
- Peng K.; Jie J.; Zhang W.; Appl Phys Lett 2008, 93, 033105.
- Al-Maghrabi, M.A.; Thorne, J.S.; Sanderson, R.J.; Byers, J.N.; Dahn, J.R.; Dunlap, R.A.; J., Electrochem. Soc. 2012, 159, A119-A711.
- Zhang, W.-J.; J. Power Sources 2011, 196, 13-24.
- Yue, L.; Zhong, H.; Tang, D.; Zhang, L.; J. Solid State Electrochem. 2013, 17, 961- 968.
- Astrova, E.V.; Fedulova, G.V.; Smirnova, I.A.; Remenyuk, A.D.; Kulova, T.L.; Skundin, A.M.; Technol. Phys. Lett. 2011, 37, 731-734.
- Wang, M.S.; Fan L.Z.; J. Power Sources 2013, 244 570-574.
- Zhang, K.; Zhao, Q.; Tao, Z.; J. Chen, Nano Res 2013, 6, 38-46.
- Hu, Y.S.; Demir-Cakan, R.; Titirici, M.M.; Muller, J.O.; Schlogl, R.; Antonietti, M.; J. Maier, Angew. Chem. 2008, 47, 1645-1649.
- Liu, W.R.; Yen, Y.C.; Wu, H.C.; Winter, M.; Wu, N.L.; J. Appl. Electrochem 2009, 39, 1643-1649.
- Vadchenko, S.G.; Sytschev, A.E.; Kovalev, D.Y.; Shchukin, A.S.; Konovalikhin, S.V.; Nanotechnologies in Russia 2015, 10, 67-74.
- Konovalikhin, S.V.; Kovalev, D.Y.; Sytschev, A.E.; Vadchenko, S.G.; Shchukin, A.S.; Int. J. Self-Propag. High-Temp. Synth 2014, 23, 217-221.
- Jia, H.; Stock, C.; Kloepsch, R.; He, X.; Badillo, J.P.; Fromm, O.; Vortmann, B.; Winter, M.; Placke T.; ACS Appl. Mat. Interfaces 2015, 7, 1508-1515.
- Wang, X.; Wen, Z.; Liu, Y.; Xu, X.; Lin, J.; Journal of Power Sources 2009, 189 121-126.
- Chen, Y.; Qian, J.; Cao, Y.; Yang, H.; Ai, X.; ACS Appl. Mat. Interfaces 2012, 4, 3753-3758.
- Park, H.; Lee, S.; Yoo, S.; Shin, M.; Kim, J.; Chun, M.; Choi, N.S.; Park, S.; ACS Appl. Mat. Interfaces 2014, 6, 16360-16367.
- Huggins, R. A., Advanced Batteries: Materials Science Aspects 1sted.; Springer, LLC: New York, NY, 2009.
- Wang, J.; Wang, Y.; Zhang, P.; Zhang, D.; Ren, X.; Journal of Alloys and Compounds 2014, 610, 308-314.
- Deng, D.; Energy Science and Engineering 2015, 3, 385-418.
- Horiba, T.; Maeshima, T.; Matsumura, Koseki, M.; Arai, J.; Muranaka, Y., Journal of Power Sources 2005, 146, 107-110.
- Johnson, B. A.; White, R. E., Journal of Power Sources 1998, 70 48-54.
- Kim, H.; Choi, J.; Sohn, H.J.; Kang, T.; J. Electrochem. Soc. 1999, 146(12), 4401-4405.
- Moriga, T.; Watanabe, K.; Tsuji, D.; Massaki, S.; Nakabayashi, I.; J. Solid State Chem. 2000, 153(2), 386-390.
- Roberts, G.A.; Cairns, E.J.; Reimer, J.A.; J. Power Sources 2002, 110(2), 424-429.



Design and Implementation of an Underwater Telemetric Glucose Monitoring System for Scuba Divers

S. Murat Egi^{1,2}, Corentin Altepe^{3,4}, Massimo Pieri¹, D. Ruzgar Sinoplu³, Danilo Cialoni¹, Tamer Özyiğit², Paola Pierleoni⁴, Alessandro Marroni¹

¹DAN Europe Research Division, Contada Padune 11, Roseto degli Abruzzi TE, ITALY

²Galatasaray University, Department of Computer Engineering, Istanbul, TURKEY

³Bogazici Underwater Research Center, Istanbul, TURKEY

⁴Marche Polytechnic University, Department of Information Engineering, Ancona, ITALY

ABSTRACT

Despite the abundance of telemetric applications for ecology, behaviour and physiology of marine life, few efforts were reported about the use of acoustic telemetry for SCUBA divers. Such systems are required to follow the medical conditions of divers with chronic health problems such as diabetics. This study communicates the details of a study to design, manufacture and test a prototype system that measures the blood glucose while diving and transmit the results in real time to the surface. A subcutaneous glucose sensor placed on the diver transmits wirelessly the glycaemia data to a microcontroller based RF receiver board placed in a custom built waterproof casing. This board works as a relay to transmit the blood glucose value to an acoustic modem SAM-1 (Desert Star Systems LLC, Monterey Bay, CA, USA) via RS232 serial communication. The modem transmits the data to the other modem, which is placed underwater at 1 m depth with a maximum baud rate of 100 bit/sec with ultrasound communication. Finally, the data reaches a portable computer from RS232 serial interface of the acoustic modem. The data is displayed and logged on the computer based at the surface. The whole system is tested to 11 Bar in hyperbaric chamber. The acoustical data link is first established between two computers located at surface to test the reliability of the communication. The acoustical link experiments were successful for 20 minutes of simulated signals for the depth, interstitial glycaemia, breathing frequency and temperature information. The overall efficiency was 80.1%, with 474 bytes sent and 378 bytes received. The bandwidth of the acoustical link is very low (max 4 reading/min) but is adequate for glycaemia monitoring that can be as low as 1 reading every 5 minutes. Finally the system recorded the interstitial glucose of divers in 8 open water dives successfully and will be beneficial for studying diabetic divers. The system has a potential to be used to verify and optimize the existing protocols on diabetic divers. It offers as well an emergency system to monitor the non-diabetic divers during extreme exposures such as saturation diving.

Keywords:

Diabetes; Underwater; Diving; Glycaemia; Subsea; Real time monitoring

INTRODUCTION

Insulin-dependent diabetes has been considered for long time as a scuba diving contraindication due to the hypoglycaemia problems potentially exposing the diver to danger. An analysis of Divers Alert Network (DAN) database from 1993 to 2007 has shown that a small percentage of DAN members were diabetic. However, it must be considered that a large proportion of diabetic divers do not declare their condition, increasing the risk for themselves and for their dive buddies. Knowing that that about 10% of world po-

pulation suffers from diabetes, a workshop was organized to draft the guidelines for diabetes and diving and protocols have been suggested for safe diving [1]. This protocols necessities the frequent measurement of blood glucose (BG). However, in some cases dives can be very long and the measurement of BG during the dive is beneficial. Pieri et al, designed and used a continuous monitoring system for BG underwater [2]. This system can be used by the diver or other members of the team, but in case of emergency it is

Article History:

Received: 2017/08/25

Accepted: 2017/11/21

Online: 2018/04/06

Correspondence to: Salih Murat Egi,
Galatasaray University, Department of
Computer Engineering,, Ciragan Cad. 36
Ortakoy 34349 Istanbul, TURKEY
E-Mail: smegi@daneurope.org

also useful that the surface attendants know the hypo/hyperglycaemia conditions in order to take necessary actions. A second benefit of a telemetric system will be to use the transmission signal for geolocalisation of the diver and thereby provide efficient search and recovery in case of emergencies.

Electromagnetic waves are rapidly absorbed by water and acoustic telemetry is the only effective method for wireless underwater monitoring [3]. Despite the abundance of telemetric applications for ecology, behaviour and physiology of marine life, few efforts were reported about the use of acoustic telemetry for SCUBA divers [4-7]. This limited number of studies had been devoted to monitor mainly ECG, temperature, heart rate and respiration frequency of divers using open circuit SCUBA. A monitoring system offers to report technical problems with rebreather equipment underwater using acoustic telemetry [8]. The previous pilot study has recorded the glucose levels of scuba divers while underwater [2]. This study to acquire in real time BG values at surface and is a continuation of this monitoring system while enabling topside bystanders to initiate any rescue in case a dangerous BG level is measured. This system will be used to verify the efficiency of the existing protocols of diabetic divers and has a potential to be used for diver geolocalisation using the single bacon navigation technique [9].

MATERIAL AND METHODS

System Design

A glycaemia measurement system that has a wireless transmitter is selected in order to intercept the signal (Dexcom G4 PLATINUM CGM System, Dexcom Inc., San Diego, CA, USA). Dexcom G4 PLATINUM CGM System consists of 3 parts. A small sensor that measures glucose levels just underneath the skin; a transmitter that is fastened on top of the sensor and sends data wirelessly to the receiver and a receiver that displays glucose trends. The sensor-transmitter pair of the system has been previously demonstrated to have a high performance under hyperbaric conditions [2]. The RF signal range of the transmitter is only 6 metres in the air and few cm in water. In order to transmit the glycaemia sensor data from a diver to the surface or to another diver, it was necessary to use acoustical modems. A pair of low cost/low baud rate (max 100 bit/sec) and relatively high range (1000 m) acoustic modems were selected (SMA-1, Desert Star Systems LLC, Monterey Bay, CA, USA). The acoustic modems accept the RS232 compatible signals, so it was necessary to convert the RF signals of the Dexcom sensor to RS232 using an open source design [10]. An electronic board was designed to accommodate the Wixel board, to pre-process the data and to configure the modems during booting sequence.

System Overview

The system is composed of;

- a G4 Platinum glucose sensor placed on the skin of the diver,
- an electronics board serving as transmitter, based on the open-source RF receiver board inside a water proof housing
- a pair of acoustic modems SMA-1,
- a computer

The main elements of the system and their workflow are represented in Fig. 1. The glucose sensor placed on the diver transmits its measure to the nearby Wixel receiver wirelessly with RF communication, which transmits the measures to an acoustic modem SAM-1 (Desert Star Systems LLC, Monterey Bay, CA, USA) with electrical, serial communication RS232. The modem transmits the measure to the other modem, which is near the surface, with ultrasound communication. Finally, the data is transmitted to the computer with an RS232 communication. The data is displayed and logged on the computer based at the surface.

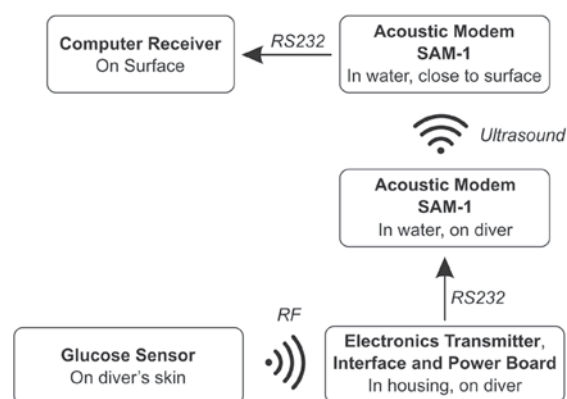


Figure 1. Block diagram of the system's composition and workflow

Glucose Sensor

The glucose G4 sensor is placed on the skin of the diver, as illustrated in Fig. 2. The sensor is made of a needle placed inside the skin, in contact with the subject's blood, a unit containing the electronics and battery, carrying out the measures and transmitting them with RF communication. The sensor measures the glucose every five minutes and transmits the data immediately. PLATINUM CGM System has its own receiver device that displays trends and instantaneous values of glucose and provides alarms. This measurement accuracy of the system under hyperbaric conditions was tested in the earlier study by Pieri et al [2] using capillary blood glucose as reference. BG was monitored every five minutes on every dive, by a dedicated CGM, and the mean of relative difference between CGM and capillary blood glucose was calculated.

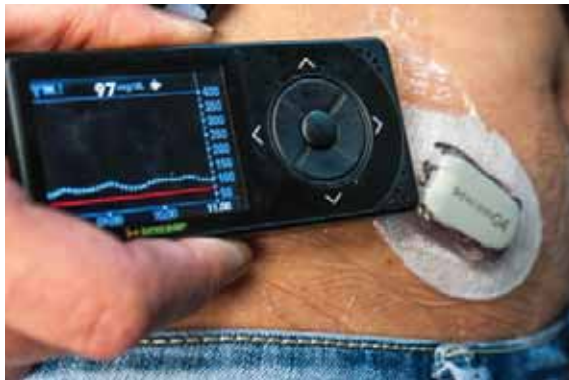


Figure 2. Dexcom G4 sensor placed on the skin of a patient

Measurement accuracy was assessed according to ISO guideline 15197 [11] and by Clarke Error Grid analysis [12] and was found to be adequate.

Electronics Transmitter, Interface and Power Board

The electronics transmitter was designed to serve several purposes;

- supply power to the diver's acoustic modem
- configure the acoustic modem upon power-up
- filter out the data received from the sensor to only transmit the significant data
- serve as an interface between the sensor and the acoustic modem

Fig. 3 details the composition of the electronics transmitter. Wixel is a general-purpose programmable module featuring a 2.4 GHz radio and USB. It is based on the CC2511F32 microcontroller from Texas Instruments, which has an integrated radio transceiver, 32 KB of flash memory, 4 KB of RAM, and a full-speed USB interface [13]. The board has 15 user I/O lines, featuring 6 analogue inputs, 2 USARTs (for serial or SPI), and 7 timer channels (capable of PWM) 4 KB of RAM and 29 KB of application program memory (flash). The Wixel features a built-in USB bootloader that can be used in conjunction with Wixel Configuration Utility software to upload custom programs or precompiled, open-source apps to the Wixel. Based on the previous experience of the firmware development on TI environment [14], the firmware of Wixel was modified to configure the acoustic modem at power-up and to filter the data received from the sensor before transmitting the data to the modem. Both the electronics transmitter and the acoustic modem placed on the diver are powered with a single, rechargeable, 9V battery. While the modem requires a supply of 8V to 16V, the electronics transmitter is powered with 3.3V and requires a step-down converter for power efficiency. An electronics board based on the FT232R chip (Future Technology Devices International Ltd., Glasgow, Scotland) is used to translate the electronic levels from 3.3V UART to RS232 for the acoustic modem.



Figure 3. Electronic circuit built for interface, transmission and power. Photograph of the electronics transmitter. 1: Modified Wixel board. 2: battery. 3: step-down converter. 4: UART-RS232 board. 5: power supply to acoustic modem. 6: power supply connector to battery

Waterproof Housing

The electronics transmitter must be placed close to the glucose sensor, because the RF transmission will be very limited in the water. Meanwhile, the electronics must be protected from the water. Therefore, a dry casing was manufactured to embed the electronics transmitter. This casing will contain a single connector to one acoustic modem. The dry casing is designed to be held at the belt of the diver, close to the sensor.

Acoustic Modems

Two identical modems SAM-1 are used for transmission of the data underwater. The SAM-1 is a miniature acoustic modem. It will transmit and receive digital data between underwater stations up to a typical range of 250 meters, with up to 1000 meters possible under ideal (quiet, deep-water) conditions. The SAM-1 features a 5-pin underwater connector through which it communicates with the host and receives power. The connectors on the SAM-1 are models MCIL5F (Seacon, El Cajon, CA, USA). Data exchange is sent to the modem as serial data, converted to an acoustic waveform, transmitted to any modems listening, received, and converted back to serial data format. Data can be exchanged between two or more SAM devices at underwater locations or between an underwater SAM and a SAM lowered by cable from a vessel at the surface. The modem has a data mode and a control mode. Data Mode is used to transmit and receive data. Control Mode is available to change modem operation parameters. The modem will be in data mode after power up. To switch to control mode the user should send '###'. The modem will acknowledge control mode by sending '<CM>'. To return to data mode, send 'D'. The modem will acknowledge data mode by sending '<DM>'. There are 3 important parameters to control the optimal transmission: Sx; Rx and Txx.



Figure 4. Close up picture of the system mounted on the diver

Sx sets the acoustic transmit data speed. Since the blood glucose data is sampled every 5 minutes, this value is set to 3 bits/sec to economise on power.

Rx sets the acoustic receive data speed. For the same reason as Sx, this value is set to 3 bits/sec. The maximum value of Sx is 154 bit/sec while and Rx is 38 bits/sec.

Txx sets the receiver detection threshold. The minimum possible threshold is T01. The modem is at its maximum sensitivity of 85 dB. The maximum threshold is T99, equivalent to a sensitivity 125 dB. The optimal Txx may change according to the medium and was set to T01 within the scope of this work.

A first modem is carried by the diver, and connected to the electronics transmitter. A second modem is near the surface and connected to a PC.

Computer

The computer is the final receiver unit. It is connected to the second modem with a serial, RS232 connection. A

terminal application is used to configure the modem and to display and log the received data.

Validation

A validation of the communication between the two modems was carried out in a swimming pool, where the conditions are less ideal due to the reverberation caused by the walls of the pool. The two modems were placed underwater, 5 to 7 meters apart and connected to two separate computers. An application was developed to quantify the quality of communication between two acoustic modems in a given medium. The application, shown in Fig. 5, connects to the modems. It sends simulated packages of 2 bytes representing either a depth, glucose level, breathing rate or a temperature through one modem at regular intervals and counts the proper reception on the second modem. The maximum sensitivity (T01) was used with Sx and Rx set to 3 bits/sec.

RESULTS

During the validation trails at the pool, different positions, threshold levels and communication rates were tested to establish the best configuration for the given conditions. After a total transmission of 398 bytes, 84.3% of the packages were properly received as a worst case. The bandwidth of the acoustical link is very low (max 4 reading/min) but is adequate for glycaemia monitoring that can be as low as 1 reading every 5 minutes.

The first dive is performed in “Istanbul Aquarium” located at Florya, Istanbul, Turkey on May 2017. A Fifty one year old, non-diabetic diver with 21 years of SCUBA diving experience made a dive to 3,8 m for 36 minutes (Fig. 6, 7). He was instructed to follow at all times the safety protocol

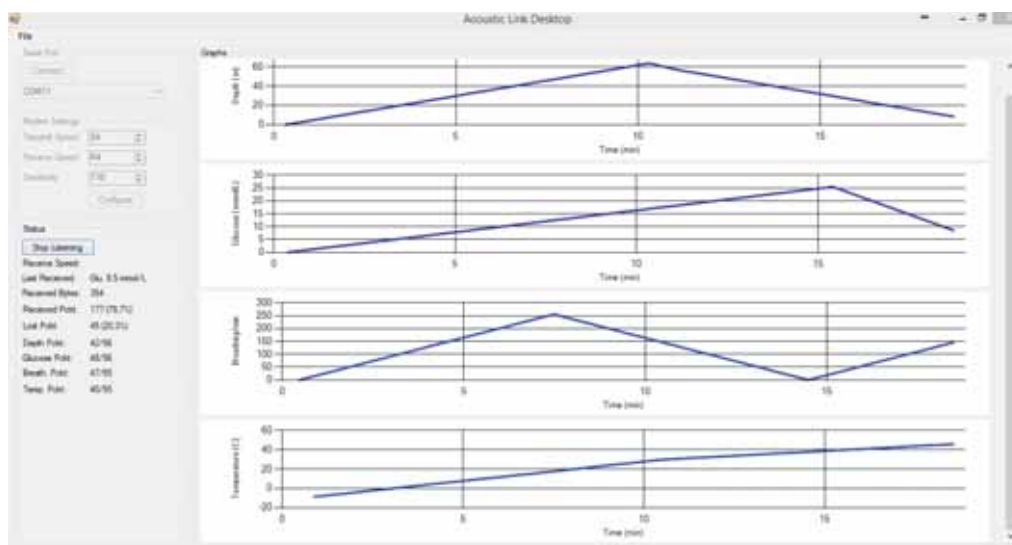


Figure 5. The graphic user interface of the application developed to validate the acoustical communication

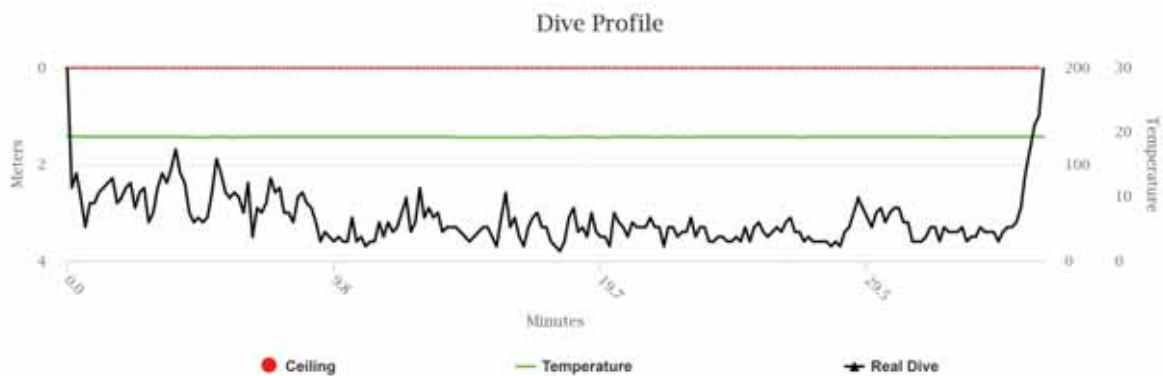


Figure 6. The Depth/Time graphic of the first dive with the acoustical monitoring system

he was trained to, and to abandon the test should any equipment fail and cause to threaten his safety. One hour prior to the dive, a value transmitted by the glucose sensor was recorded. During the dive, the glucose sensor transmitted every 5 minutes. During this dive, 7 BG data have been collected from the water to the surface station and no data was lost. Immediately after the dive, the scuba divers glucose level was measured again.

The system stated to be used to supervise a female diabetic diver, 33 year old, with more than 300 of dives of experience since May 2017. In total, 129 minutes of diving is supervised and 27 BG data is collected while 2 data packages are lost during transmission. The maximum depth of dives was 10.4m.



Figure 7. The telemetric system during the first test dive at Istanbul Aquarium

DISCUSSION

Diabetes, particularly insulin-requiring diabetes mellitus has most commonly been viewed as a condition that should preclude participation in activities during which sudden loss of consciousness may pose a significant risk. Scuba diving is one such activity, as impaired consciousness due to hypoglycaemia underwater would impair the ability to help oneself or a partner and could be fatal [15]. On the other side, The Americans with Disabilities Act [16] was designed to remove barriers and promote equal access for all individuals. A secondary effect was that exclusionary policies were more easily challenged, thus requiring clear and compelling evidence to justify such decisions. The legislation has substantial weight in cases where prohibitions are primarily based on theoretical risk. Subsequent protocols are established to provide recreational diving opportunities for diabetics [1] and were evaluated using pre and post dive data [17]. The study presented in this communication establishes a firm way of supervising the diabetics while diving and shall provide adequate protection for a significant population of world who is diabetic. In fact, World Health Organization guidelines based estimated prevalence of diabetes is very high(12.3%) and includes many individuals for whom no formal diagnosis has been made.

The system needs software and hardware improvements in order to be more useful. The number of lost data during sea dives is even lower than pool trials (93,21% versus 80,1% efficiency) probably due to the challenging reverberation effects at the pool. However, the transmission protocol was decided to be modified such that each BG data should be sent 10 times in expense of reducing the battery life. Therefore, a fresh battery needs to be placed before each dive and will provide autonomy of 75 minutes as a minimum.

The system presented in this study a one-way data flow: from the sensor to the supervisor. However, the acoustic modems enable a two way communication. Such system

could be enhanced with the capability for the supervisor to send messages to the diver. The communication protocol could be improved with an acknowledgement for each package sent, avoiding any data loss in harsh environment conditions and economizing the battery life.

Such system could be integrated in a dive computer to display the glucose levels to the diver while transmitting the same data to surface. In the future, the monitoring system could extend automatic alerts to inform both the surface staff and the diver (sound, vibration and/or light). This system could be extended further to interface with a web server, for remote monitoring and to alert authorities in case of a safety threat. Finally, the supervisor could use such system to send messages to the diver, such as requesting an abortion of the dive and to start the ascent.

CONCLUSION

Today, diabetic divers measure their level before a dive, sometimes twice with a time interval to guess the trend. However, while underwater, it is impossible for them to know whether their glucose is reaching dangerous levels (either high or low).

The prototype of the system presented in this study is fully assembled, programmed, validated and tested on scuba divers at the Istanbul Aquarium, Istanbul, Turkey, in May 2017. The system is in use to collect more data on a diabetic diver since May 2017. Such development participates in making recreational diving a safer activity for the diabetic divers. The system presented in this study brings an extra layer of security while diving and visibility of the trend of the glucose level. Diabetic divers could benefit from real-time blood glucose monitoring during their dives to prevent worsening of hypoglycaemia and to correctly interpret hypoglycaemia-like symptoms whilst diving.


ACKNOWLEDGEMENTS

This study is financed partially by the GreenBubbles project that has received funding from the European Union's Horizon 2020 Research and Innovation programme under the Marie Skłodowska-Curie grant agreement No 643712. This document reflects only the authors view. The Research Executive Agency is not responsible for any use that may be made of the information it contains.

References

1. Pollock, NW, Uguccioni, DM, Dear, GdeL. (Eds.). Diabetes and recreational diving: guidelines for the future. Proceedings of the UHMS/DAN Workshop, Durham, NC, 19 June, Divers Alert Network, 136 p, 2005.
2. Pieri, M, Cialoni, C, Marroni, A. Continuous real-time monitoring and recording of glycemia during scuba diving: pilot study. *Undersea Hyperb Med* 43 (2016) 265-272.
3. Baggeroer, AB. Acoustic telemetry overview. *IEEE J Oceanic Engineering* 9 (1984) 229-235.
4. Fell, RB, Skutt, HR, Waterfield, A. Four-channel ultrasonic telemetry system for obtaining physiological data from ocean divers. *Biotelemetry* 1 (1974) 50-59.
5. Gooden, BA, Feinstein, R, Skutt HR. Heart rate responses of scuba divers via ultrasonic telemetry. *Undersea Biomed Res* 2 (1975) 11-19.
6. Istepanian, RHS. Use of microcontrollers for diver monitoring by underwater acoustic biotelemetry in multipath environments. PhD thesis, Loughborough Univ. U.K., 1994.
7. Woodward, B, Istepanian, RSH. Physiological monitoring by underwater ultrasonic biotelemetry. *J. Soc. Underwater Technol* 18 (1992) 34-44.
8. Egi, SM. Design of an acoustic telemetry system for rebreathers. *Undersea Hyperb Med* 36 (2009) 65-71.
9. Vaganay J, Baccou P, Jouvencel B. Homing by acoustic ranging to a single beacon. Proceedings OCEANS 2000 MTS/IEEE Conference, 3 (2000), 1457-1462.
10. Black, S. wixel-xdrip. <https://github.com/StephenBlackWasAlreadyTaken/wixelxDrip>, 2015. Access date: 20.08.2017.
11. In vitro diagnostic test systems -- Requirements for blood-glucose monitoring systems for self-testing in managing diabetes mellitus. ISO 15197:2013.
12. Clarke WL, Cox D, Gonder-Frederick LA, Carter W, Pohl SL. Evaluating clinical accuracy of systems for self-monitoring of blood glucose. *Diabetes Care* 10 (1987) 622-628
13. <https://www.pololu.com/product/1336>. Access date: 14.11.2017.
14. http://www.innovasub.com/pages/decopage.aspx?pro=uepm_d_board. Access date: 14.11.2017.
15. Davis J, Bove AA. Medical Evaluation for Sport Diving. In: Bove AA, ed. *Diving Medicine*, 3rd ed. Philadelphia, PA: WB Saunders Co.; 1997: 355-6.
16. USA Public Law 101-336; 104 Stat. 327; 1990
17. Dear G de L, Pollock NW, Uguccioni DM, Dovenbarger J, Feinglos MN, Moon, RE. Plasma glucose responses in recreational divers with insulin-requiring diabetes. *Undersea Hyperb Med* 2004; 31(3)291-301.
18. The Expert Committee on the Diagnosis and Classification of Diabetes Mellitus. Report of the Expert Committee on the Diagnosis and Classification of Diabetes Mellitus. *Diabetes Care* 2003;26(S):5-20.

Investigation of the Suitability of a Pipe Stock Site in Terms of Geotechnical Characterization and Engineering Design Parameters Considering the Economic Aspects

Mustafa Can Canoglu 

Department of Environmental Engineering, Sinop University, 57000, Sinop, TURKEY

ABSTRACT

Geotechnical investigations are generally site specific and the parameters variate spatially and sometimes temporally due to meteorological events and earth dynamics. In this study, the suitability of an inert area to utilize a pipe stock site under a natural gas pipeline project was investigated, while considering the economic yield. Within the context of this study, office works and field works are performed. Geotechnical data are collected during the field work in order to assess sub-surface conditions, prevailing under the proposed loads or pipe batch structures. Under field works, drilling operations, in-situ testing are performed. Assessment of the collected sub-surface data and its interpretation are realized within the office works. In other respects, rentability is one of the main parameters controlling the feasibility of the project in engineering. In this study, the bearing capacity of the soil profile and the liquefaction potential of the investigated area are enlightened and the suitability of the study area for the project is evaluated by comparing it with the various alternatives of soil remediation techniques and the consideration of their costs. As a result of this study, it is revealed that the soil remediation costs are much more than port storage renting fees.

Keywords:

Bearing capacity; Liquefaction analysis; Geotechnical investigations

INTRODUCTION

In geotechnical engineering, soil is defined as the unaggregated natural material formed by the weathering and deposition processes of rock cycle. Due to the inhomogeneous nature and complexity of soil forming processes, physical parameters of soils variate spatially [1]. Soil moisture content variations by virtue of the rainfall runoff dynamics, a temporal variation of physical parameters of soils come into question. Additionally, inherent variability of different soil parameters include also measurement errors and model transformation uncertainties [1]. Soil liquefaction is an important event which can be occurred by an earthquake in fully saturated and cohesionless soils. In consequence of liquefaction, pore water pressure of soil increases which provoke a dramatical shear strength loss, and important decrease in bearing capacity. The results of low bearing capacity and liquefaction have critical and severe concerns in engineering. For this reason, prior to the construction

stage, geotechnical characterization of soil should be investigated precisely to predict the liquefaction potential and bearing capacity problems. Under these circumstances, engineering use of lands requires a detailed ground investigation in order to assess the liquefaction potential and the bearing capacity characteristics. Geotechnical site characterization in terms of soil bearing capacity and foundation analysis are studied by many researchers [2, 3, 4, 5, 6, 7]. In these studies, obtaining of the geotechnical parameters in the most correct way with in-situ testing and laboratory testing are emphasised. Bowles [2] expressed bearing capacity considering SPT. Random field theory and elasto-plastic finite element analysis are used to determine the spatial variability of cohesion and angle of internal friction by [3, 4]. Geotechnical site characterization with in-situ testing applications are presented by [5]. Measurement errors for soil in-situ testing in a geotechnical site characterization is

Article History:

Received: 2017/09/27

Accepted: 2018/03/21

Online: 2018/04/06

Correspondence to: Mustafa Can Canoglu,
Department of Environmental Engineering,
Sinop University, 57000, Sinop, TURKEY
Phone: +90 368 271 4151
Fax: +90 368 271 4152
E-mail: mccanoglu@sinop.edu.tr

studied by [6]. Vanmarcke [7] modelled the engineering properties through a soil profile.

The aim of this study is to investigate the geotechnical characteristics and to determine the soil remediation costs of an inert area with a low rental cost to use as a pipe storage site for an international natural gas pipeline project. The soil remediation costs of this inert area is compared with a regular port storage area (which is expected of no soil remediation) as an alternative since its rental costs are 800% higher than the inert area.

MATERIAL AND METHODS

In terms of definition of the geotechnical problems which is assumed to be faced in the field and search for solutions; preliminary works including office and field survey/analysis and detailed site works and detailed office works are also performed throughout the project. Field pre-studies consist of investigation of detailed geological mapping of the study area and its near environ. Drilling operations, in-situ testing are conducted under detailed site works. The results of these systematic works are evaluated with detailed office works considering the profitability of subjected study area including the soil remediation costs. As a result of these engineering works, ultimate feasibility of the storage operations on the study area is determined in terms of geotechnical applicability.

Profitability of a project is one of the main issues in engineering. In this study, the soil remediation alternatives are evaluated considering their costs and construction time. In this regard, excavation of problematic layer of soil and filling it with suitable natural structural material, jet grouting, drain swamping and port storage renting fees are also compared. Within the context of this study, the engineering approaches are presented when assessing different soil remediation alternatives and project feasibility in terms of project profitability.

STUDY AREA

Study area is located in İskenderun (Mediterranean Region) in which the climate is characterized by dry summers and mild rainy winters. İskenderun is an important county of Hatay city with a huge seaport and industrial potential. The average temperature during the hottest month is around 32 to 34°C whereas the average temperature during the coldest month is around 10 to 12°C. Mean annual rainfall is 850 mm with an irregular regime. This precipitation regime causes an inharmonic fluctuation of water table considering the elevation of the study area which is 2.5 m on average. This situation affects the soil dynamics in terms of soil moisture content and liquefaction potential.

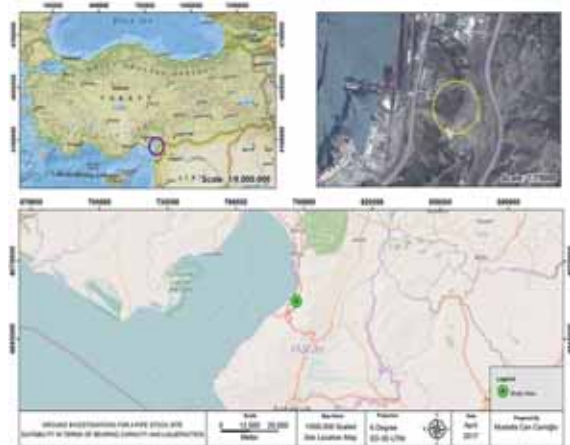


Figure 1. Site location map of the study area



Figure 2. General view of study area

The study area is identified in 1/25000 scaled Hatay O36-d3 topographic map prepared by National Mapping Agency of Turkey [8]. Investigations are conducted in the swamp region that is located on the western side of İskenderun-Payas state road. İskenderun-Ceyhan highway is located on the eastern side of the study area where, there is a military area on the southern side. Additionally, İskenderun-Payas state road is located on the western side of study area where FIL Filter Factory and warehouses of logistic companies are located on the northern side. Transportation is provided by highways for four seasons (Fig. 1 - 2).

Geological Setting of Study Area

In the study area and its near environ the Mesozoic and Cenozoic aged geological units are dominantly observed. Triassic-Jurassic aged Demirkazık Formation (Tj) are founded in the base of stratigraphic array. Demirkazık Formation is covered discordantly by Cretaceous aged Kızıldağ Ophiolites (Ck) [9]. Finally, Quaternary aged alluvium (Qal) and slope debris (Qsw) cover all these units discordantly (Fig. 3 - 4).

Demirkazık Formation (Tj)

The eastern side of İskenderun depression and along the line of Amanos Mountain, the formation consists of micritic limestone. This formation is light- dark gray colored,

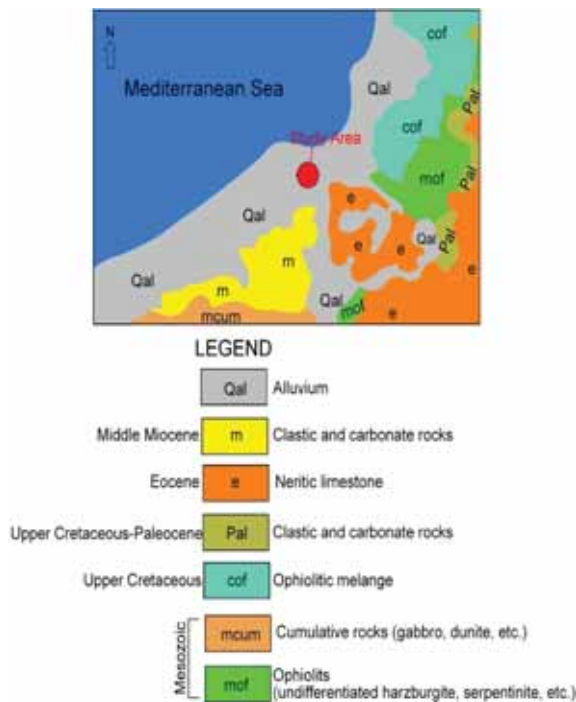


Figure 3. Simplified geological map of the study area

medium to coarse grained bedded and microfossiliferous [9].

Kızıldağ Ophiolite (Ck)

The outcrop of Kızıldağ Ophiolite is observed at the eastern side of the project area through a north-south (NS) direction. This allochthonous unit composes the section of Amanos Mountain's southwest margin. Kızıldağ Ophiolite is generally formed by; from youngest to oldest, tectonite, cumulate, diabase, dyke mélangé, pillow lavas and volcano-sedimentary rocks, respectively. In the investigation area, olivine serpentinization is observed for different rock types of Kızıldağ Ophiolite. Isoclinal folding is specifically characterized for Kızıldağ Ophiolites. This folding can be evaluated as the trace of an active tectonism which can cause liquefaction potential in the study area during a possible earthquake. The outcrops of this unit are generally weathered and can be classified as soil [9].

Slope Debris (Qsw)

Blocky structured slope debris are formed by the weathered bedrock and transported to piedmont. For this reason, slope debris is constituted by coarse gravel and clay sized material and the cementation is observed. The color of slope debris is generally light brown-brown, greenish gray and white, its grain size varies between clay to coarse gravel. Pebbles and blocks are angular, semian-gular or rounded and the origin is serpentine. The slope debris thickness can reach up to 1,5 m based on field observations.

UPPER SYSTEM	SYSTEM	SERIES	FORMATION	SYMBOL	LITHOLOGY	EXPLANATIONS
CENOZOIC	QUATERNARY		Alluvion	Qal	[Symbol]	Formed by permeable materials such as, sand, gravel, clayey gravel, sandy clay, silt.
			Slope Wash	Qsw	[Symbol]	On the piedmont of steep slope, grain size varies between clay to coarse block.
MESOZOIC	CRETACEOUS		Kızıldağ Ophiolite	Ck	[Symbol]	Tectonite, Cumulate, Diabase, Dyke Mélangé, Pillow Lavas, Volcano-Sedimentary Rocks, Serpentinities
			Demirkazlı Formation	Taf	[Symbol]	Miocenic Limestone
	TRIASSIC					

Figure 4. : Columnar stratigraphic section in the study area [modified from 9]

Alluvium (Qal)

Quaternary aged alluviums are formed by the sediments transported by the Yarikkaya River by erosion, transportation and deposition processes. This unit is constituted by gravel, sand, silt and clay sized material. According to the drilling works, the thickness of the alluvium is varies between 2.50 - 5.00 m in the study area.

GEOTECHNICAL CHARACTERIZATION OF STUDY AREA

In the study area 11 ground investigation boreholes are drilled in order to determine the geotechnical parameters and the prediction of potential risks. These investigations reveal two different zones in the study area in terms of different soil bearing capacity characteristics under dynamic loads (Fig. 5).

In the study area, some traces of active tectonism are observed, this part consist of normal faulting component presumably developed in the East Anatolian Fault Zone (EAFZ) [10]. In Fig 6, the fault which is found in the study area is presented. That fault is crossing the quaternary aged alluvium which indicates that the fault is potentially active. As liquefaction needs dynamic movements to be occurred in soft soils, this fault could be evaluated as the triggering effect of a potential liquefaction in the study area.

During field observations, we have discovered some areas having very low bearing capacity which was proved

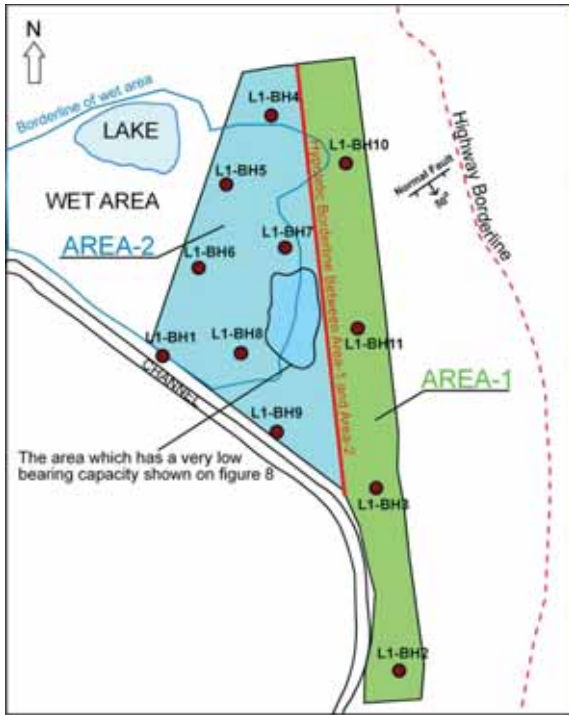


Figure 5. Zonation plan of the project area

by a picture shown in Fig 7. For this reason, the study area is separated into two different area; area-1 and area-2 namely.

In Area-1, the soil is cohesionless and the depth varies between 7.0 – 16.5 m. For the borehole L1-BH3, the bedrock extends to 20 m depth. For the boreholes, L1-BH2, L1-BH10 and L1-BH11 the bedrock (serpentine) is located under the subjected cohesionless soil. In Area-2 a peat type soil is encountered which is known with its low bearing capacity. The depth of peat varies between 2.0 – 11.7 m and under the peat bedrock depth is deeper than 20 m (Fig. 8). 8 types of



Figure 6. Normal faulting observed in the study area, the arrows show the direction of the movement along the fault scarp (red line)



Figure 7. A photograph showing the very low soil bearing capacity of area-2

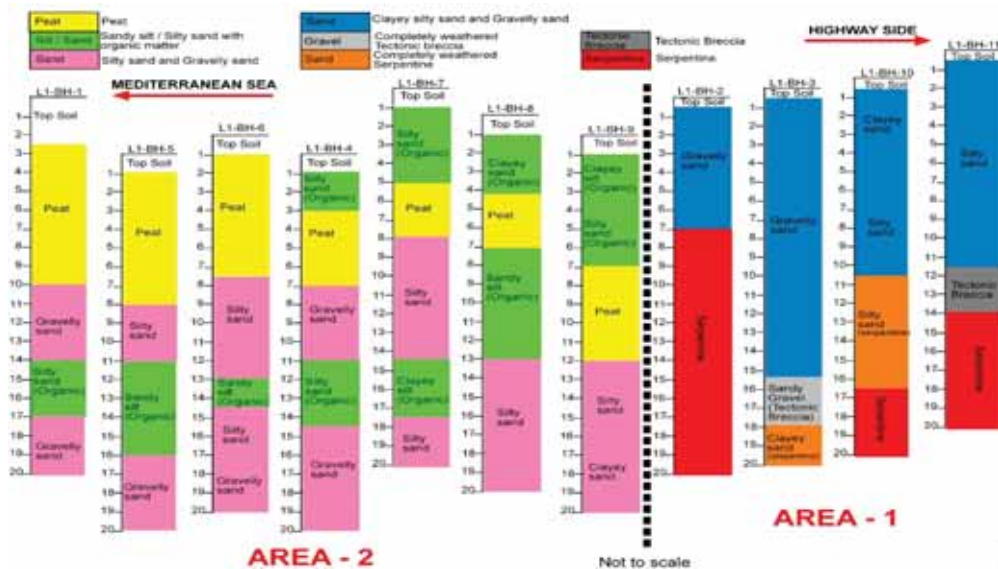


Figure 8. Stratigraphic correlation of the lithological logs collected from the study area

ground is sampled during drilling operations and laboratory tests that has been performed to determine their geotechnical characteristics.

Top Soil

The thickness of top soil layer observed in all boreholes (L1-BH-4 is the exception) is up to 0.70 meters from the ground level. It is planned to remove top soil layer by stripping excavations. For this reason, any of laboratory tests were carried out for this layer.

Filling material

This layer constitute of the residual soil subjected to a recent fill material and decided to be removed by stripping excavations due to its soft character and low bearing capacity.

Peat

This layer contains highly organic soil which is dark brown - black, with vegetable tissue, fibrous – amorphous texture, with organic odour. This layer is generally consists of 4% gravel, 37% sand and 59% fine materials and observed in the boreholes; L1-BH-1 between 2.50 – 9.65 meters, L1-BH-4 between 2.90 – 7.05 meters, L1-BH-5 between 0.90 – 7.85 meters, L1-BH-6 between 1.20 – 7.40 meters, L1-BH-7 between 4.90 – 7.90 meters, L1-BH-8 between 4.00 – 7.00 meters, L1-BH-9 between 7.20 – 11.70 meters. The Geotechnical parameters of peat layer are listed in Table 1.

Sandy silt and silty sand

This layer consists of clay-silt-sand and gravel units with different ratios. Sand and Silt units are the dominant ones. This layer contains dense organic material. Gravels

and clays are observed locally. This layer is characterized by Sandy Silt – Silty Sand which consists of 10% gravel, 43% sand and 47% fine materials. The layer observed in the boreholes; L1-BH-1 between 14.00 – 17.30 meters, L1-BH-4 between 0.80 – 2.90 and 11.00 – 14.60 meters, L1-BH-5 between 11.00 – 16.00 meters, L1-BH-6 between 13.00 – 14.50 meters, L1-BH-7 between 0.90 – 4.90 and 14.70 – 17.50 meters, L1-BH-8 between 0.90 – 4.00 and 7.00 – 13.00 meters, L1-BH-9 between 1.10 – 7.20 meters. The Geotechnical parameters of sandy silt and silty sand layer are listed in Table 2.

Silty sand and gravelly sand

Silty sand and gravelly sand layer is a multi-coloured and heterogonous. It consists of silty- gravelly sand. The saturation level is approximately 90% for this layer. The mean grain size distribution is 20% gravel, 59% sand and 22% fine material and clay-silt-sand and gravel units with different ratios. Sand and Silt are dominant units. This layer contains dense organic material. Gravels and clays are observed in the boreholes; L1-BH-1 between 9.65 - 14.00 and 17.30 – 21.50 meters, L1-BH-4 between 7.05 – 11.00 and 14.60 – 20.13 meters, L1-BH-5 between 7.85 – 11.00 and 16.00 – 20.00 meters, L1-BH-6 between 7.40 – 13.00 and 14.50 – 19.95 meters, L1-BH-7 between 7.90 – 14.70 and 17.50 – 20.00 meters, L1-BH-8 between 13.00 – 20.00 and, L1-BH-9 between 11.70 – 20.00 meters. The Geotechnical parameters of silty sand and gravelly sand layer are listed in Table 3.

Clayey sand – silty sand – gravelly sand

Clayey sand – silty sand – gravelly sand layer is multi-coloured and heterogonous. It consists of loose to very dense clayey - silty – gravelly sand. The moisture con-

Table 1. Geotechnical characteristics of peat layer

Test Name		Minimum	Average	Maximum	
Moisture Content	W_n	32.6	141.2	301.8	%
Bulk Density	V_n	1.07	1.30	1.60	g/cm ³
Dry Density	V_d	0.29	0.60	1.02	g/cm ³
Specific Gravity	G_s	1.85	2.36	2.62	
Sieve Analysis	No.4 Retaining	0.0	4.4	26.1	%
	No.200 Passing	17.5	59.1	99.0	%
Atterberg Limits	Liquid Limit	NP		89	%
	Plastic Limit	NP		69	%
	Plasticity Index	NP		37	%
Triaxial Test	Cohesion	0.07	0.26	0.33	kg/cm ²
	Internal Friction Angle	1	2	4	o
Consolidation Test	Swelling Pressure		<0.10		kg/cm ²
	Void Ratio	1.567	3.538	6.703	
SPT	Field Values	0	3	11	
	Corrected Values	0	2	8	
Soil Classification			PT		

tent of this layer around the study area is generally 90 to 95%. The mean grain size distribution is 21% gravel, 52% sand and 27% fine material and clay-silt-sand and gravel units with different ratios. Sand and Silt units are dominant. This layer contains dense organic material. Gravels and clays are observed in the boreholes; L1-BH-2 between 0.30 – 7.00 meters, L1-BH-3 between 0.10 – 15.85 meters, L1-BH-10 between 0.30 – 10.30 meters, L1-BH-11 between 0.20 – 11.40 meters. The Geotechnical parameters of clayey sand – silty sand – gravelly sand layer are listed in Table 4.

Tectonic breccia

This layer consist of yellowish beige, slightly to highly we-

athered (W3-W4) and fractured rock medium. Tectonic breccia unit is observed in the borehole L1-BH-11 between 11.40 – 13.80 meters. The Geotechnical parameters of tectonic breccia unit are listed in Table 5.

Serpentine

This layer constitute of dark green to greenish brown, slightly to highly weathered (W3-W4) and highly fractured rock medium. Serpentine unit is observed in the boreholes; L1-BH-2 between 7.00 – 20.00 meters, L1-BH-10 between 16.50 – 20.00 meters and L1-BH-11 between 13.80 – 20.00 meters. The Geotechnical parameters of serpentine unit are listed in Table 6.

Table 2. Geotechnical characteristics of sandy silt and silty sand layer.

Test Name			Minimum	Average	Maximum	
Moisture Content		W_n	11.25	35.66	83.20	%
Sieve Analysis	No:4 Retaining		0.0	10.4	38.0	%
	No:200 Passing		9.9	46.5	82.8	%
Atterberg Limits	Liquid Limit	LL	NP		59	%
	Plastic Limit	PL	NP		43	%
	Plasticity Index	PI	NP		21	%
SPT	Field Values	N_{30}	0	14	R	
	Corrected Values	$N_{1,60}$	0	10	>50	
Soil Classification				MLO/SCO		(generally)
				SMO,SCO,SM,ML		(locally)

Table 3. Geotechnical characteristics of silty sand and gravelly sand layer.

Test Name			Minimum	Average	Maximum	
Moisture Content		W_n	5.06	17.53	31.50	%
Sieve Analysis	No:4 Retaining		0.0	19.7	47.4	%
	No:200 Passing		3.4	21.6	48.6	%
Atterberg Limits	Liquid Limit	LL	NP		59	%
	Plastic Limit	PL	NP		34	%
	Plasticity Index	PI	NP		25	%
SPT	Field Values	N_{30}	7	32	R	
	Corrected Values	$N_{1,60}$	3	21	>50	
Soil Classification				SC/SM		

Table 4. Geotechnical characteristics of clayey sand – silty sand – gravelly sand.

Test Name			Minimum	Average	Maximum	
Moisture Content		W_n	8.70	17.59	31.43	%
Sieve Analysis	No:4 Retaining		6.8	20.6	42.5	%
	No:200 Passing		9.5	26.9	48.6	%
Atterberg Limits	Liquid Limit	LL	NP		51	%
	Plastic Limit	PL	NP		30	%
	Plasticity Index	PI	NP		21	%
SPT	Field Values	N_{30}	4	32	R	
	Corrected Values	$N_{1,60}$	2	21	>50	
Soil Classification				SC/SM		

Table 5. Geotechnical characteristics of tectonic breccia unit.

Test Name		Minimum	Average	Maximum	
Natural Unit Weight	V_n :	1.19	1.88	1.85	g/cm ³
Point Load Index	$I_{s(so)}$:	0.04	0.045	0.05	MPa
Field Values	TCR :		100		%
	RQD :	0	25	100	%

Table 5. Geotechnical characteristics of serpentine unit.

Test Name		Minimum	Average	Maximum	
Natural Unit Weight	V_n :	1.72	2.10	2.38	g/cm ³
Point Load Index	$I_{s(so)}$:	0.01	0.07	0.17	MPa
Field Values	TCR :	33	79	100	%
	RQD :	0	7	100	%

RESULTS AND CONCLUSION

In this study, the spatial variations of the soil geotechnical parameters of the study area are determined by the systematic analyses of drilling, in-situ test and geotechnical laboratory surveys. As discussed earlier, the study area is divided into two areas namely area-1 and area-2 in terms of their geotechnical properties. Within the project, It is predicted that area-1 will have approximately 250 kPa service load in total (live loads; ground pressure of crawler crane is 109 kPa for this project, fill loads; max. height of fill is approximately 4.00 m. and pipe loads; the weight of a long pipe is 15 ton, 3 rows were stacked, load is distributed from 2 points). The soil strength of the area-1 is enough to bear these service loads under existing conditions. However, this area is located on a flooding gully and Ground Water Level (GWL) can rise up to ground level during a heavy rains. For this reason, area-1 tends to liquefy in case of seismic loads as there is an active fault in and close proximity of the study area. Additionally, the soil material in this area can be subjected to liquefaction under dynamic loads which is controlled by the active tectonism of EAFZ. Under seismic loading, bearing capacity would be decreased dramatically (Fig 7).

For shallow footings, an embankment with a thickness of minimum 50 cm formed by cleaned granular material is proposed for Area-1. This granular fill should be covered by a lean concrete of minimum 20 cm thick. Placement of an appropriate geotextile under this granular fill, to prevent the water infiltration, can be considered as another alternative.

Area-1 and area-2 are compared in terms of bearing capacity values and possible soil improvement techniques. Area-1 have poor soil conditions with a groundwater level (GWL) deeper than 7m. The liquefaction potential of Area-2 is higher than Area-1; but for some local parts of Area-1 can be evaluated as susceptible for liquefaction. In Area-2 the

groundwater level is shallow and the general topography of the Area-2 can be evaluated as flooding gully. Deep foundations are obligatory for Area-2. However the costs of deep foundations are not profitable for this project.

The soil improvement techniques are assessed for Area-1 and Area-2 in order to find out the most suitable and rentable technique. With this context, removing the problematic soil layer and replacing it with rock fill is evaluated. But the soil thickness planned to be removed by the stripping excavation is approximately 3.5m. In this case, approximately 550 000 m³ of excavation is predicted. In consideration of unit prices for excavation which is evaluated by General Directorate of State Hydraulic Works (DSI) and General Directorate of Highways (KGM), the costs will exceed the economic limits of the project. Additionally, in case of heavy rainfall, GWL can rise up to ground level and soil tend to liquefy under even slightest dynamic load caused by an earthquake or a dynamic vibration during the handling operation. Consolidation (preloading + drainage) and vibro-replacement stone column alternatives are also considered but these techniques consume time and not suitable for the soil type of the study area. For the dynamic compaction alternative, Atterberg limits could be fulfilled. However non-plastic (NP) soil is not dominated the whole area. At least Jet grouting and/or pile foundation are recommended in order to remediate the soil of the pipe storage area. It is emphasized that with this remediation load bearing capacity which is controlled by only pile point strata and frictional resistance will be improved since liquefaction potential of soil is ignored. Under this circumstance, pile foundation and jet grouting alternatives can be applied to augment the bearing capacity but these techniques are not effective for a potential liquefaction event. In conclusion, excavation and rock infilling, pile foundation, jet grouting, vibro replacement stone, drain swamping, utilizing geotextile are compared as the different alternatives of soil remediation in terms of feasibility and profitability. On the other hand, the port

storage alternative (renting fee is 8 times more expensive) which has no need of soil remediation, is also evaluated. In this context, need of 550 000 m³ excavation is not rentable based on the unit prices valued by DSI and KGM. Pile foundation and jet grouting techniques are also neglected due to their ineffectiveness in prevention from liquefaction. Vibro replacement stone and drain swamping alternatives are also evaluated within the scope of the project. However, these techniques are time consuming and do not meet the urgency criterion of the project. An embankment of gravel (minimum 50 cm thick) and concreting on it and protect this construction with an impermeable geotextile is also recommended as an alternative. But this alternative is also time consuming and exceed the economic limits of the project. For this reason, the port storage is the most suitable alternative regarding the project schedule, and economic aspects in spite of its 800% more expensive renting fee. The remediation costs of the study area will be also more expensive than the port storage renting fees.

ACKNOWLEDGEMENTS

Author thanks sincerely to SuYapı Engineering and Consulting Co. family especially to Department of Geology and Geotechnics who finance for this article and share their engineering experiences with their scientific support.

References

1. Phoon, K.K. and Kulhawy, F.H., 1999. Characterisation of geotechnical variability. *Can. Geotech. J.* 36, 612–624.
2. Bowles, J.E., 1996. *Foundation analysis and design*, fifth ed. McGraw - Hillbook Co.
3. Fenton, G.A. and Griffiths, D.V., 2003. Bearing capacity prediction of spatially random $c-\Phi$ soils. *Can. Geotech. J.* 40(1), 54–65.
4. Griffiths, D.V. and Fenton, G.A., 2001. Bearing capacity prediction of spatially random soil: the undrained clay Prandtl problem revisited. *Géotechnique* 54 (4), 351–359.
5. Huang A.B. and Mayne, P.W., 2008. In: Huang Mayne (Eds.), *Geotechnical and Geophysical Site Characterisation*. Taylor and Francis Group, London. ISBN:978-0-415-46936-4.
6. Jaksa, M.B., Brooker, P.I. and Kaggwa, W.S., 1997. Inaccuracies associated with estimating random measurement errors. *ASCE J. Geotech. Geoenviron. Eng.* 123 (5), 393–401.
7. Vanmarcke, E.H., 1977. Probabilistic modelling of soil profiles. *ASCE J. Geotech. Eng.* 103 (11), 1227–1246.
8. National Mapping Agency of Turkey, 1999. 1/25000 scaled Hatay O36-d3 topographical map.
9. Tekeli, O. and Erendil, M., 1985. Kızıldağ ofiyolitinin (Hatay) jeoloji ve petrolojisi. *MTA Dergisi*. 33–48.
10. Barka, A. and Reilinger, R., 1997. Active tectonics of the Eastern Mediterranean region: deduced from GPS, neotectonic and seismicity data. *Annali Di Geofisica*. XL (3), 587–610.

Thermal Behaviour of Residential Buildings with Cantilever Beams under Winter Boundary Conditions

Lütfü Namli

Ondokuz Mayıs University, Department of Mechanical Engineering, Samsun, Turkey

ABSTRACT

In this study, the thermal behaviour of residential buildings with cantilever beam under winter boundary conditions was numerically investigated by means of the open-ended structure approach. For this purpose, parametric studies were carried out for various ratios of cantilever beam depth/cantilever beam height (d/H) and Rayleigh numbers using a computer program for no wind laminar flow conditions. Analyses were conducted for Rayleigh numbers in the range of 10^3 to 10^6 . The calculations were carried out for the ratios of d/H , namely 0.0, 0.2, 0.4, 0.6, 0.8 and 1.0. The working fluid was treated as air ($Pr=0.71$). According to the findings, the mean Nu number along with the outer vertical wall (surface L) of the residential building, in general, decreases as d/H increases. This decrease in the mean Nu number is evident for $Ra \leq 10^4$, but it appears to be more pronounced after $Ra=10^5$. To have minimum heat loss from a residential building under winter day boundary conditions, it is suggested that the ratio of d/H should be between 0.2 and 0.5.

Keywords:

Open-ended structure; Extended boundaries; Cantilever beam; Laminar natural convection

Article History:

Received: 2017/07/16

Accepted: 2017/12/20

Online: 2017/12/26

Correspondence to: Lütfü Namli,
Department of Mechanical Engineering,
Ondokuz Mayıs University, Samsun, Turkey
e-mail: lnamli@omu.edu.tr

INTRODUCTION

In recent years, the fluid flow and heat transfer phenomena surrounding open-ended cavities or enclosures related to the natural convection mechanism have received significant interest from many researchers, both numerically and experimentally. There are many reasons for this interest. In particular, several applications of practical interest, such as thermal building insulation by means of air gaps, solar energy collectors, fire control in buildings, thermal storage systems, and electronic cooling in which can be modelled by different extensions of similar geometry [1-2]. One such field of application is a thermal performance in residential buildings. Residential buildings are one of the most important energy consumers in the world. Approximately 30% of European and Middle Eastern energy consumption occurs in residential buildings [3-5]. Reducing thermal energy consumption is, therefore, an important issue facing the building industry. However, the great majority of studies on the thermal performance of residential buildings have focused on insulating them by applying various building envelopes [5-7]. However, an equally important matter is the exterior geometry of the buildings. The literature related to the effects of building exterior geometry on the thermal perfor-

mance of residential buildings has not been adequately studied. Current studies are usually concerned with examining the effects of exterior geometry on the interior ventilation of a building [8]. One of the most important structures that form the external geometry of residential buildings is the cantilever beam, which is very common in many countries, e.g. Turkey [7]. In this field, numerous efforts have been taken to analyse these rectangular cavities, which are often two-dimensional. Two-dimensional natural convection related to cavities or enclosures comprises a large proportion of these analyses in the literature. However, a relevant but more complicated problem related to open-ended or partial enclosures cavities has attracted less attention. The two-dimensional natural convection related to open-ended enclosures (cavities) have been examined by many researchers in the cited literature in the past four decades [9, 10]. Chan and Tien [10] carried out a numerical laminar natural convection study for a two-dimensional open-ended enclosure having a vertical wall. In this study, the vertical wall of the enclosure was heated and the other two horizontal walls of the enclosure were insulated. The study results indicated the influences of the extended boundary on the main flow

forms. Analyses were performed in the computational zone extended along with the open plane of the open-ended cavity for Rayleigh numbers ranging from 103 to 109. The same authors [10] also calculated the steady-state laminar natural convection in a two-dimensional rectangular open-ended cavity by applying the proximate boundary circumstances at the enclosure open plane. A detailed study was carried out by Vafai and Ertfagh [11, 12] to analyse the characteristics and physics of flow areas in enclosures. The same authors [11, 12] also studied the extended computational zone effect upon fluid flow and heat transfer in an enclosure and its immediate environment. Similarly, many researchers have studied buoyancy-driven fluid flow and heat transfer within enclosures that have one side open by giving particular importance to their outer approximate confines. The studies cited in the literature have concentrated on obtaining an exact representation of the prevalent boundary circumstances at the open plane in both two- and three-dimensional open-ended cavities [13-16].

The effects of cantilever beam applications, which are commonly encountered in buildings and other constructions in many countries, on the thermal behaviour of residential buildings are subjects which can be analysed in the scope of the natural convection subject using an open-cavity approach. In the literature, there are many studies of flow in open cavities and the resulting effects on heat transfer [11, 13]. However, no study has examined the effects of cantilever beam applications on the thermal behaviour of residential buildings. However, a few studies related to the energy-saving designs for buildings' frontispieces are available in the literature. One of the most comprehensive studies on this subject was conducted by Prianto and Depecker [17]. In their study, the effects of projecting balconies on indoor air quality were investigated computationally in detail. Lai and Wang [18] examined the key factors in building frontispiece design which saves energy in Taiwan by utilizing the simulation software eQUEST. Chan and Chow [19] investigated an ordinary residential flat with a balcony built into the living room and its energy performance utilizing the typical weather data set of Hong Kong, which has a subtropical climate. Chand et al. [20] experimentally investigated the influence of balconies on ventilation, which induces the prevailing wind forces. The experimental results showed that provision of balconies changes wind pressure distribution on the windward wall but does not display considerable alteration in it on the leeward side. Namli (21) studied airflow and heat transfer in built-in balcony applications, using a computational investigation based on the open-ended structure approach. The numerical results indicated that the built-in balcony application on buildings reduces heat loss for all Rayleigh numbers considered.

In this study, the main problem is the heat loss of the residential buildings due to the entrances on the external geometry of the buildings. The entrance of the residential buildings such as the cantilever beam applications was considered as a cavity. Then, the heat loss from the exterior surface of the residential building was determined by utilizing open-ended enclosure and extended boundaries approaches and calculating the Nu number. That is, the open-ended cavity approach is adapted to this heat loss problem related to the residential buildings. A similar study is not available in the literature. As mentioned above, current studies in the literature are usually concerned with examining the effects of exterior geometry on the interior ventilation of a building. Accordingly, the cantilever beam application has been considered as a form of the cavity and have been subjected to numerical investigation in terms of building thermal performance. Considered all these, the aim of this study is that the thermal behaviour of residential buildings with cantilever beams, which are often used for creating balconies or other extensions above ground level in residential architecture, was investigated computationally by means of the open-ended enclosure approach. For this purpose, a parametric study was conducted for various ratios of cantilever beam depth/cantilever beam height (d/H) and Rayleigh numbers using a computer program encoded in Fortran when there was no wind for laminar flow. In the computational analysis, according to Boussinesq's approach (for $\Delta T \leq 20$ °C), the change in density caused by heat difference was taken into account only when calculating buoyancies. The other density values in the analysed equations are assumed to be constant in this temperature range. However, the air taken into account in the analysis was accepted as the Newtonian fluid, and $Pr=0.71$ was accepted. Vorticity, stream function and energy equations were analysed together within the boundary conditions defined. The findings obtained were arranged in the counter diagrams for both streamlines and isotherms. To determine the heat loss, the mean Nusselt numbers were defined for the outer vertical wall of L within the enclosure for each case.

Analyses were conducted for Rayleigh numbers ranging from 10^3 to 10^6 so long as they stayed in the laminar flow. In the calculations, values of 0.0, 0.2, 0.4, 0.6, 0.8 and 1.0 were used as the ratios of d/H . In this way, the analysis for the various ratio values of d/H for especially high Rayleigh numbers was obtained in the range of $0.0 \leq d/H \leq 1.0$. As a result of the discussion of the findings obtained, the effects of the various ratios of d/H and the Rayleigh numbers on the mean Nusselt number calculated along the L surface (the outer vertical wall of the enclosure) were examined.

FORMULATION AND NUMERICAL SCHEME

The two-dimensional enclosure analysed in this work, which has an open side (open-ended cavity) of height $(H + L)$ and width B , is shown simply as a schematic diagram in Fig. 1. The vertical and horizontal walls of the building are heated to a constant temperature t_H , while the horizontal ground of the solution section is maintained at a constant temperature t_C , which is lower than t_H . The surrounding fluid which interacts with the open-ended enclosure is at an ambient temperature t_∞ , which is in thermal equilibrium with t_C . The working fluid at atmospheric air and Newtonian, and the flow is presumed to be incompressible and laminar. The fluid properties are constant except for the density ρ , which is assumed to differ linearly from the temperature in reference to Boussinesq's approximation. Joule heating and viscous dissipation were neglected in this study. The working fluid was treated as air whose Prandtl number was equal to 0.71.

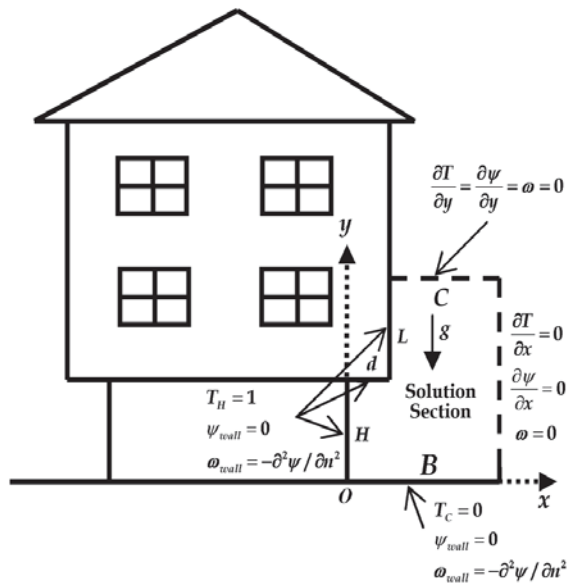


Figure 1. Schematic representation of solution domain

Considering the aforementioned assumptions, the governing equations can be expressed in the dimensionless form of stream function-vorticity equations as follows:

$$\frac{\partial}{\partial x} \left(T \frac{\partial \psi}{\partial y} \right) - \frac{\partial}{\partial y} \left(T \frac{\partial \psi}{\partial x} \right) - \frac{\partial}{\partial x} \left(\frac{1}{Pr} \frac{\partial T}{\partial x} \right) - \frac{\partial}{\partial y} \left(\frac{1}{Pr} \frac{\partial T}{\partial y} \right) = 0 \quad (1)$$

$$\frac{\partial}{\partial x} \left(\omega \frac{\partial \psi}{\partial y} \right) - \frac{\partial}{\partial y} \left(\omega \frac{\partial \psi}{\partial x} \right) - \frac{\partial}{\partial x} \left(\frac{\partial \omega}{\partial x} \right) - \frac{\partial}{\partial y} \left(\frac{\partial \omega}{\partial y} \right) = 0 \quad (2)$$

$$\frac{\partial^2 \psi}{\partial x^2} + \frac{\partial^2 \psi}{\partial y^2} = -\omega \quad (3)$$

where

$$\omega = \frac{\partial v}{\partial x} - \frac{\partial u}{\partial y}, \quad u = \frac{\partial \psi}{\partial y}, \quad v = -\frac{\partial \psi}{\partial x} \quad (4)$$

Equations (1)-(3) are the equations of the dimensionless temperature, vorticity and stream function, respectively.

The Dimensionless Boundary Conditions

As is the case with Fig. 1, the dimensionless boundary conditions in the extended computational zone can be written as:

1. For the left vertical and horizontal walls of the enclosure at $x=0$ and $0 \leq y \leq H$; $x=d$ and $H \leq y \leq L$; at $y=H$ and $0 \leq x \leq d$;

$$T_H = 1, \quad \psi_{wall} = 0, \quad \omega_{wall} = -\frac{\partial^2 \psi}{\partial n^2} \quad (5)$$

2. For the bottom horizontal wall of the enclosure at $y=0$ and $0 < x \leq B$;

$$T_C = \psi_{wall} = 0, \quad \omega_{wall} = -\frac{\partial^2 \psi}{\partial n^2} \quad (6)$$

3. For the x - far field open boundary at $x=B$ and $0 < y \leq H+L$;

$$\frac{\partial T}{\partial x} = \frac{\partial \psi}{\partial x} = \omega = 0 \quad (7)$$

4. For the y - far field open boundary at $y=H+L$ and $d < x \leq C$;

$$\frac{\partial T}{\partial y} = \frac{\partial \psi}{\partial y} = \omega = 0 \quad (8)$$

where ω_{wall} is the vorticity value at the wall and n is the outer normal of the surface. The vorticity at sharp corners requires special consideration. The vorticity bifurcation at the corners is basically taken into account via the introduction of two different vorticity values. The vorticity values of the sharp corner were calculated as the arithmetical average of the values of the two adjacent wall nodes. These circumstances were applied to calculate the relevant values for all solution section limitations when the steady-state numerical calculations were carried out. The temperature conditions at the sharp corners also require special attention. The discontinuity of the temperature at the rectangular intersection and base walls (the origin of the coordinate system

selected) was determined by taking into consideration the arithmetical average temperature of both walls at the corner and maintaining the connected nodes with the relevant temperatures of the wall.

Nusselt Numbers

The energy transported across the vertical inner wall of the residential building is expressed as local and mean Nusselt numbers. Accordingly, for the outer vertical wall (surface L) of the residential building, the local Nusselt numbers can be derived from the dimensionless temperature gradients in the normal direction of the surface as shown in the following relationship:

$$Nu_{y,L} = \frac{\partial T}{\partial n} \Big|_{x=d} \quad (9)$$

and then the mean Nusselt number along the outer vertical wall (L) is;

$$Nu = \frac{1}{L} \int_H^L \frac{\partial T}{\partial n} \Big|_{x=d} dy. \quad (10)$$

where n denotes the normal direction of the surface. The integration of Eq. (10) was carried out by applying the trapezoidal rule. This equation of the mean Nusselt number is used to stand for all the heat transfer findings in this study.

Numerical Methods

The equations for energy transport, vorticity transport and the stream function together with the boundary conditions represent the problem under consideration. In this study, the equations for vorticity transport and energy transport were calculated using the alternating direction implicit (ADI) method, which is a finite difference technique [22]. After that, the equation of the stream function was calculated using the Gaussian successive over-relaxation (SOR) technique [23]. Convective terms were predicted using the upwind differencing scheme. For diffusive terms, the central difference scheme was used. In the present study, a uniform grid distribution was applied. Many calculation experiments were carried out to achieve grid-independent results for all the field variables. During testing and evaluation of the grid-independence of the present prediction scheme, many numerical calculations were performed for higher Rayleigh numbers. During the testing and evaluation of grid independence of the current prediction, several numerical calculations were conducted for higher Rayleigh numbers. These assessments found out that a uniformly spaced grid of 161x101 for a C-shape cavity can be used to correctly define the fluid flow and heat transfer processes within the open-ended enclosure, especially close to the walls while keeping up with rapid changes of the

dependent variable. Further increments in the grid point numbers acquired the same results. When the following convergence criteria were ensured for each point in the solution zone, the analyses were accepted to converge:

$$\left| \frac{\phi_{new} - \phi_{old}}{\phi_{new}} \right| \leq 10^{-4} \quad (11)$$

where ϕ stands for the dimensionless values of stream function ψ , vorticity ω and temperature T .

Model Validation

Verification of the used model is considered a significant part of this study. To examine the validity of the numerical results, the present numerical model with corresponding wall boundary conditions was verified through comparison with an experimental study conducted by Abu-Mulaweh et al. [24] as shown in Fig. 2. For the laminar boundary layer airflow of buoyancy-induced natural convection along a two-dimensional vertical forward step, some considerations were presented in that work. The upstream and downstream walls and step itself were maintained at a uniform and constant temperature. Fig. 2 illustrates the effect of step height on the local Nusselt number's axial variation downstream of the step (surface L) for the case of $\Delta T=23^\circ\text{C}$ (between the free stream and the heated wall), $Ra=6.134 \times 10^7$ and step height of 16 mm. It is seen in this comparison that the results of this study match on a large scale with the results of Abu-Mulaweh et al. [24]. The results of the present study were also veri-

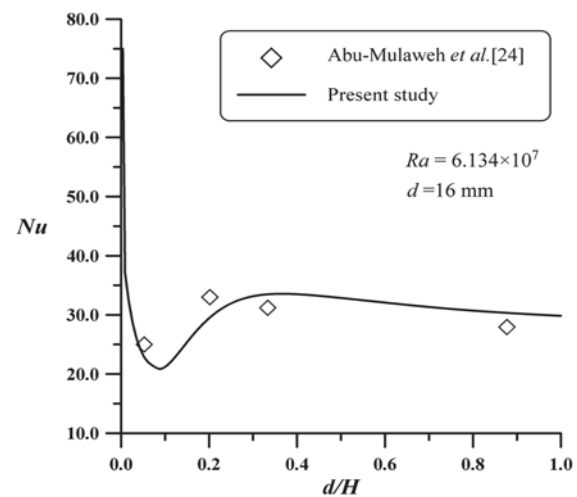


Figure 2. Local Nusselt number vs. y on the outer vertical wall (surface L).

fied by comparison with the numerical results of Asan and Namli [25, 26].

For the values of the velocities and temperatures, the conditions of the open boundary were approximated by denoting the normal gradients at zero at these locations. The

aforementioned recommendations ensured sufficient precision on the condition that the solution zone was enlarged far enough. Penot [27] numerically carried out a natural convection study in a two-dimensional open-ended enclosure in which all vertical and horizontal walls were isothermal. The author also calculated the governing equations in an extended computational zone by taking account of the boundary conditions of the far field. In addition, according to Vafai and Etefagh [11], the properties of fluid flow and heat transfer in an enclosure which is open on one side and in its immediate surroundings will not vary considerably assured that the solution zone is enlarged at last 60 times the cavity height in cases of high Rayleigh numbers. On the contrary, LeQuere et al. [28] applied a maximum extension of only about twice the enclosure height in determining the outer boundary conditions in order to calculate the laminar natural convection in a heated open-ended cavity. In the present study, the extension of the solution zone was four times the cantilever beam height of the residential building (H), and the ratios of d/H were varied from 0.05 to 1.0.

RESULTS AND DISCUSSION

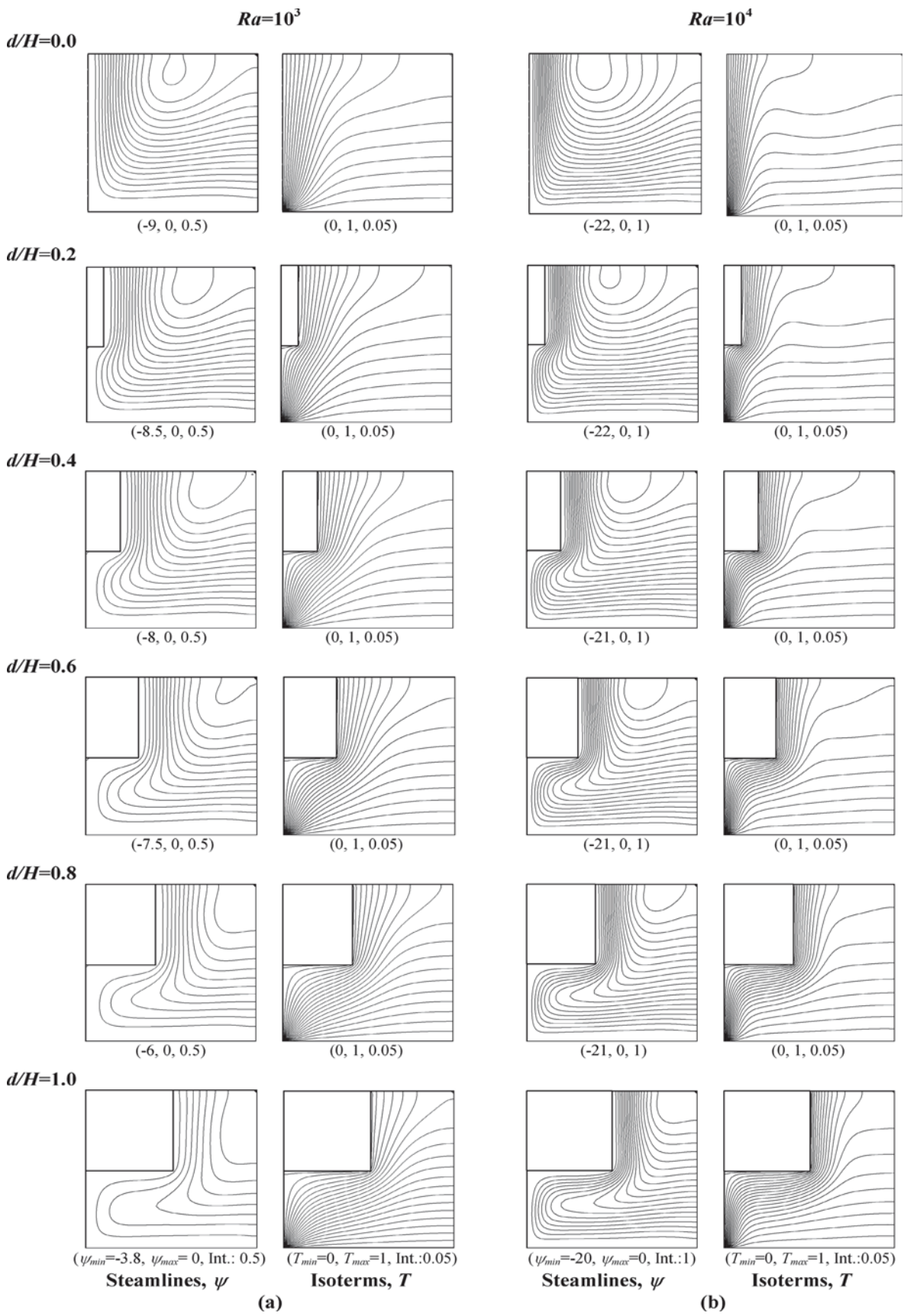
In the present study, various prevalent parameters such as Rayleigh number and the ratio of d/H were analysed. Most of the results were attained for cases in which the building walls had a dimensionless temperature of $T_h = 1$ and the ground had a dimensionless temperature of $T_c = 0$. The working fluid was air, which has a Prandtl number of 0.71. The calculations were carried out for cantilever beam d/H ratios of 0, 0.2, 0.4, 0.6, 0.8, 1.0. Rayleigh numbers ranged from $Ra = 10^3$ to $Ra = 10^6$ so long as they stayed in the laminar flow.

In this study, in order to remove the influences of the far field analysis on the properties of the flow field and heat transfer in an enclosure which was open on one side and in its adjacent area, the open boundaries were properly enlarged four times the height of the enclosure in both directions. Only the portion focused on the open-ended zone and its adjacent area was introduced in the form of contour line graphics (in terms of isotherms and streamlines) to demonstrate the fields of the fluid flow and temperature results in the enclosure. The isotherm values began with 0.0 and increased by 0.05 for all contour line graphics of the dimensionless temperature in this study. For all solid boundaries, the streamline contour values were taken as zero and increased by 0.5 for $Ra = 10^3$, 1.0 for $Ra = 10^4$, 2.0 for $Ra = 10^5$, and 5.0 for $Ra = 10^6$. First, the effects of different d/H ratios, taking account the Rayleigh number, on the flow and temperature field were discussed with the help of comparing streamlines and isotherms as shown in Fig. 3. At the same time, with the graphics given in Fig. 4 and Fig. 5, in both situations and with different Rayleigh numbers, the change in the mean

Nusselt numbers calculated along the outer vertical wall (surface L) was examined with respect to the d/H ratio.

The effect of Rayleigh number on the streamlines and the isotherms for different flow cases was illustrated in Fig. 3. As Fig. 3a shows, for $Ra = 10^3$, the heat transfer in the enclosure and on the vertical and horizontal walls of the residential building takes place predominantly by way of the conduction mechanism. Nevertheless, heat transfer via the convection mechanism is definitely not negligible, as shown in Fig. 3a by the isotherm distortion on the open side. When the hot buoyant fluid escapes from the restraint at the top of the horizontal surface, it climbs like a buoyant plume into the outdoor space. Due to this ejection mechanism [11, 12], the cold fluid from the outdoor space crawls into the open enclosure, and meanwhile, the hot fluid departs in the same way. The intensity of the ejection mechanism at low Ra numbers ($Ra = 10^3$ and $Ra = 10^4$) gradually decreases as the d/H ratio increases, whereas this intensity at higher Ra numbers ($Ra = 10^5$) generally increases as the d/H ratio increases. For $Ra = 10^6$, the intensity of the ejection mechanism remains unstable, and this intensity has the highest value at a d/H ratio of 0.4. Moreover, the ejection mechanism also gives rise to energy transfer from the building walls of the enclosure to the neighbouring fluid. In addition, the fluid flow area in an enclosure which is open on one side is not symmetric around the middle-height plane for low Ra numbers. The reason is that the ejection mechanism, which acts on the hot input fluid, achieves a higher velocity in connection with the dropout flow when compared to the incoming flow. Therefore, the incoming cold fluid replaces a larger part of the gap plane than the hot exiting flow as a direct consequence of mass conservation. Furthermore, it can be seen in Fig. 3c and Fig. 3d that a single clockwise vortex is observed in the enclosure except for higher Rayleigh numbers ($Ra = 10^5$ and $Ra = 10^6$) and the eye of the vortex is located at the top of the cross-section. With an increase in the Rayleigh number, a multi-eyed clockwise vortex appears in the enclosure. When the Rayleigh number increases, the clockwise vortex speed in the open-ended enclosure increases as well.

Accordingly, with an increase in Rayleigh number ($Ra = 10^5$ and $Ra = 10^6$), while the buoyancy force intensity increases, the thermal boundary layer thickness along the L surface decreases. Moreover, the flow penetrates into the cavity especially for higher Rayleigh numbers, filling the entire cavity with an increasing d/H ratio. As the Rayleigh number increases further, the cold fluid penetrates the cavity at much higher velocity. Then, as the temperature gradient increases because of the decrease in the thermal boundary layer thickness, the heat transfer from the L surface (the outer vertical wall within the enclosure) to the fluid increases. This increase in the heat transfer can be seen clearly in Fig. 4 and Fig. 5.



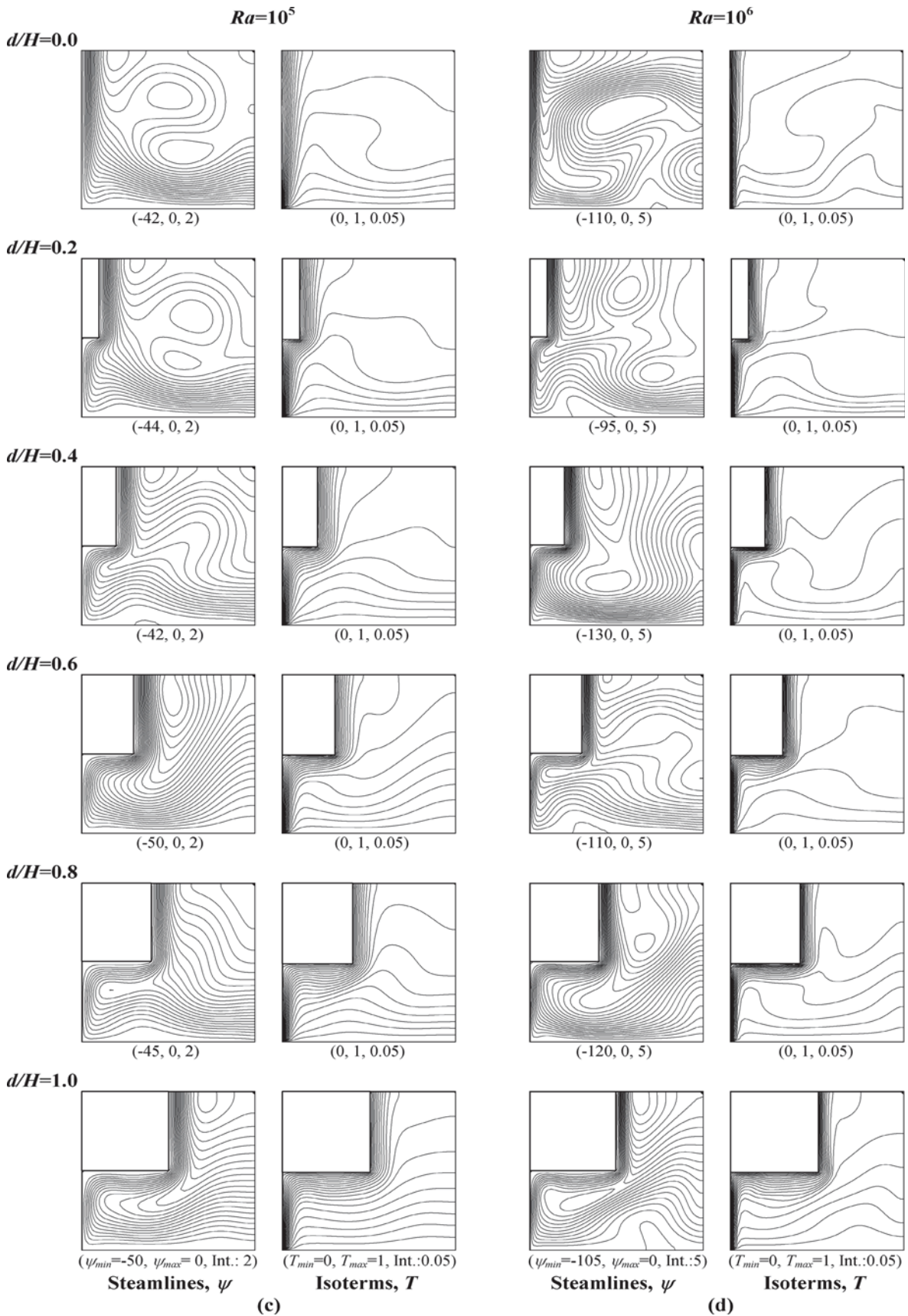


Figure 3. The effect of the ratio of cantilever beam depth/cantilever beam height (d/H) and Rayleigh number upon streamlines and isotherms: (a) $Ra=10^3$, (b) $Ra=10^4$, (c) $Ra=10^5$, (d) $Ra=10^6$

As shown in Fig. 3a and Fig. 3b, for lower Rayleigh numbers ($Ra=10^3$ and $Ra=10^4$), one can observe a tendency for the speed of the clockwise vortex to decrease because of the intensity of the buoyancy force with an increase in the d/H ratio. As a result, the thickness of thermal boundary layer increases along the L surface in this situation. As this happens, the temperature gradient decreases and the heat transfer, which occurs along the L surface from the hot surface to the fluid, shows a tendency to decrease. On the contrary, as shown in Fig. 3c and Fig. 3d, for higher Rayleigh numbers ($Ra=10^5$ and $Ra=10^6$), a multi-eyed clockwise vortex appears in the enclosure, causing the speed of the clockwise vortex to increase for some d/H ratios while it decreases for other d/H ratios. For example, for $Ra=10^5$ and $d/H=0.4$ the speed of the clockwise vortex decreases in comparison with the no-cantilever-beam-application case ($d/H=0.0$). In the same way, for $Ra=10^6$ and $d/H=0.2$ the speed of the clockwise vortex decreases in comparison with the no-cantilever-beam-application case. These decreases in the speed of the clockwise vortex for higher Rayleigh numbers can be explained by the fact that there are reversed flows in the ground (surface B). In the case that there is no reversed flow in the ground, the fluid that starts to move because of the effects of the buoyancy force intensity together with the increase in the d/H ratio can move more easily in the cavity. With this freedom of movement, it can be understood that the ejection mechanism is more effective in these situations. Afterward, the cold air from the surrounding area quickly infiltrates into the lower part of the open cavity to take up the separating fluid. This suction mechanism creates an almost parallel flow over the entire vertical wall in the open-ended cavity. Although there is an irregular flow pattern in the enclosure at higher Rayleigh numbers, the thickness of the thermal boundary layer along the L surface increases with the increasing d/H ratio. As the temperature gradient decreases due to the increasing thickness or thermal boundary layer, the heat transfer from the L surface to the fluid decreases gradually. This decrease in the heat transfer can be seen clearly in Fig. 4 and Fig. 5. In these figures, the distribution of the mean Nu number is given only for L except for $d+H+L$ because d consistently varies with the d/H ratio. Furthermore, in comparison with H in residential buildings, L actually has a much bigger value. As can be seen in Fig. 4, as the d/H ratio increases, the mean Nu number along the L surface does not change significantly at low Ra numbers ($Ra = 10^3$ and $Ra = 10^4$), but the mean Nu number along the L surface at higher Ra numbers ($Ra=10^5$ and $Ra=10^6$) decreases considerably as the d/H ratio increases. It can also be seen from Fig. 4 that the Nu number is not stable for high Ra numbers (especially for $Ra = 10^6$). As can be seen in Fig. 5, there is no significant change in the mean Nu number when the d/H ratio increases, whereas a significant decrease in the mean Nu number as the d/H ratio increases can be observed for values above $Ra=10^4$. Consequently, as can be

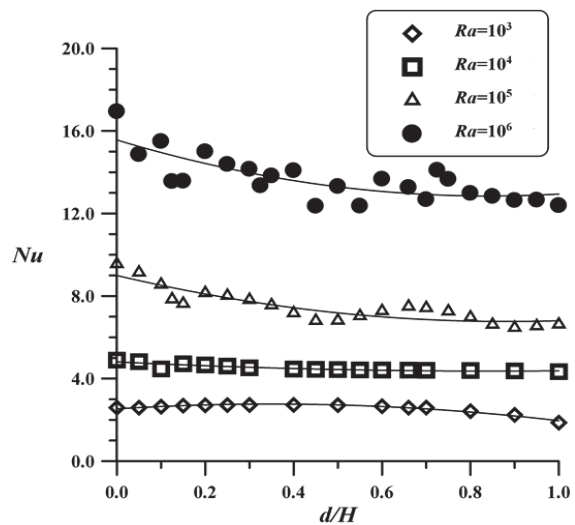


Figure 4. The effect of the ratio of cantilever beam depth/cantilever beam height (d/H) upon the mean Nusselt number along the L surface

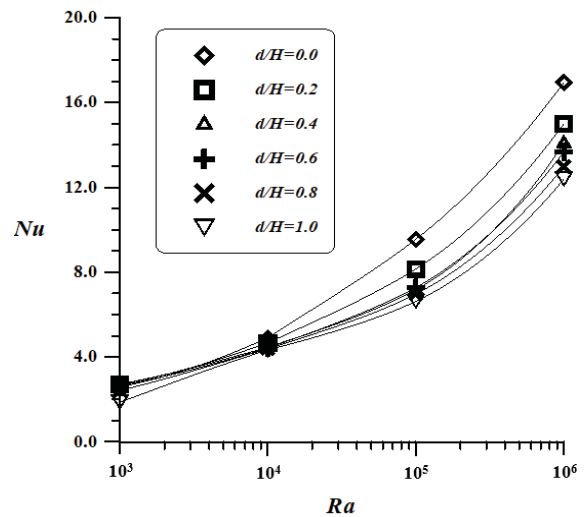


Figure 5. The effect of Rayleigh number upon the mean Nusselt number along the L surface

seen in Fig. 4 and Fig. 5, the decreases in heat transfer along the L surface (the outer vertical wall of the enclosure) with the increasing d/H ratio for the values of $Ra=10^3$, 10^4 , 10^5 and 10^6 are approximately 28%, 11%, 31% and 30% in comparison with the no-cantilever-beam-application case, respectively.

CONCLUSION

In this study, the thermal behaviour of buildings with cantilever beams under winter day boundary conditions was investigated numerically by means of the open-ended structure approach. For this purpose, a parametric study was performed for various ratios of cantilever beam d/H and Rayleigh numbers using a computer program when there was no wind for laminar flow. Analyses were con-

ducted for Rayleigh numbers varying from 10^3 to 10^6 . The analyses were carried out for d/H ratios of 0.0, 0.2, 0.4, 0.6, 0.8 and 1.0. The working fluid was air ($Pr=0.71$).

The most important effect of the heat loss within the residential building cantilever beam (within the cavity) is the ejection mechanism. The intensity of the ejection mechanism at low Ra numbers ($Ra = 10^3$ and $Ra = 10^4$) gradually decreases as the d/H ratio increases, whereas this intensity at higher Ra numbers ($Ra=10^5$) generally increases as the d/H ratio increases. For $Ra = 10^6$, the intensity of the ejection mechanism remains unstable, and this intensity has the highest value at a d/H ratio of 0.4. Moreover, the ejection mechanism also gives rise to energy transfer from the building walls of the enclosure to the neighbouring fluid.

The ejection mechanism also affects the thickness of the thermal boundary layer in the cavity. The thickness of the thermal boundary layer decreases with the increasing intensity of the ejection mechanism. Eventually, as the temperature gradient increases because of the decrease in the thermal boundary layer thickness, the heat transfer from the L surface (the outer vertical wall within the cavity) to the surrounding fluid increases. According to all these, in general, the mean Nu number, which is an indication of heat loss from the cavity, along with the outer vertical wall (surface L) of the residential building decreases with an increase in the d/H ratio for all Rayleigh numbers. This decrease in the mean Nu number is evident for $Ra \leq 10^4$, but after $Ra=10^5$ it appears to be more pronounced. To have minimum heat loss from residential buildings under winter day boundary conditions, it is suggested that the ratio of d/H be between 0.2 and 0.5.

NOMENCLATURE

H	cantilever beam height of building (m)
d	cantilever beam depth of building (m)
L	outer vertical wall of the enclosure (m)
d/H	the ratio of cantilever beam depth/cantilever beam height
Pr	Prandtl number
Ra	Rayleigh number
t_{∞}	ambient temperature ($^{\circ}C$)
t_H	hot wall temperature of the enclosure (K)
t_C	cold wall temperature of the enclosure (K)
Δt	temperature difference
T	dimensionless temperature
Nu_y	local Nusselt number
Nu	the mean Nusselt number
g	acceleration of gravity (m/s^2)
k	the coefficient of thermal conductivity (W/mK)

h the coefficient of convective heat transfer (W/m²K)

n the normal direction of the surface

Int. Interval

Greek symbols

ψ dimensionless stream function

ω dimensionless vorticity

ν kinematic viscosity (m^2/s)

β the coefficient of volume expansion ($1/K$)

α thermal diffusivity (m^2/s)

Subscript

H hot wall

C cold wall

min minimum

max maximum

References

1. Raithby GD, Hollands KGT. Natural convection, in: Rohsenow WM, Harnett JP, Ganic EN, (Eds.), Handbook of Heat Transfer Fundamentals. second ed. McGraw-Hill, New York, 1985 (Chapter 6).
2. Ostrach O. Natural convection in enclosure, Journal of Heat Transfer 110 (1988) 1175-1190.
3. Tavares MCP, Goncalves HJP, Bastos JNTFC. The glazing area in residential buildings in temperate climate: The thermal-energetic performance of housing units in Lisbon. Energy and Buildings 140 (2017) 280-294.
4. Aimee Byrne A, Byrne G, O'Donnell G, Robinson A. Case studies of cavity and external wall insulation retrofitted under the Irish home energy saving scheme: Technical analysis and occupant perspectives. Energy and Buildings 130 (2016) 420-433.
5. Magalhaes SMC, Leal VMS, Horta IM. Modelling the relationship between heating energy use and indoor temperatures in residential buildings through artificial neural networks considering occupant behavior. Energy and Buildings 151 (2017) 332-343.
6. Yousefi F, Gholipour Y, Yan W. A study of the impact of occupant behaviors on energy performance of building envelopes using occupants' data. Energy and Buildings 148 (2017) 182-198.
7. Jin X, Medina MA, Zhang X. On the placement of a phase change material thermal shield within the cavity of buildings walls for heat transfer rate reduction. Energy 73 (2014) 780-786.
8. Sorgato MJ, Melo AP, Lamberts R. The effect of window opening ventilation control on residential building energy consumption. Energy and Buildings 133 (2016) 1-13.
9. Selamat EE, Arpacı VS, Borgnakke C. Simulation of laminar buoyancy-driven flows in an enclosure. Numerical Heat Transfer, Part A 22 (1992) 401-420.
10. Chan YL, Tien CL. A numerical study of two-dimensional natural convection in square open cavities. Numerical Heat

- Transfer 8 (1985) 65-80.
11. Vafai K, Etefagh J. The effect of sharp corners on buoyancy-driven flows with particular emphasis on outer boundaries. *International Journal of Heat and Mass Transfer* 33 (1990) 2311-2328.
 12. Vafai K, Etefagh J. Thermal and fluid flow instabilities in buoyancy-driven flows in open-ended cavities. *International Journal of Heat and Mass Transfer* 33 (1990) 2329-2344.
 13. Khanafer K, Vafai K, Lightston M. Mixed convection heat transfer in two-dimensional open-ended enclosures. *International Journal of Heat and Mass Transfer* 45 (2002) 5171-5190.
 14. Elsayed MM, Chakroun W. Effects of aperture geometry on heat transfer in tilted partially open cavities. *Journal of Heat Transfer* 121 (1990) 819-827.
 15. Khanafer K, Vafai K. Buoyancy-driven flows and heat transfer in open-ended enclosures: Elimination of the extended boundaries. *International Journal of Heat and Mass Transfer* 43 (2000) 4087-4100.
 16. Khanafer K, Vafai K. Effective boundary conditions for buoyancy-driven flows and heat transfer in fully open-ended two-dimensional enclosures. *International Journal of Heat and Mass Transfer* 45 (2002) 2527-2538.
 17. Prianto E, Depecker P. Characteristic of airflow as the effect of balcony, opening design and internal division on indoor velocity: A case study of traditional dwelling in urban living quarter in tropical humid region, *Energy and Building* 34 (2002) 401-409.
 18. Lai CM, Wang YH. Energy-saving potential of buildings envelope designs in residential houses in Taiwan. *Energies* 4 (2011) 2061-2076.
 19. Chan ALS, Chow TT. Investigation on energy performance and energy payback period of application of balcony for residential apartment in Hong Kong. *Energy and Building* 42 (2010) 2400-2405.
 20. Chand I, Bhargava PK, Krishak NLV. Effect of balconies on ventilation inducing aeromotive force on low-rise buildings. *Building and Environment*. 33 (1998) 385-396.
 21. Namli L., Effects of built-in balcony on thermal performance in residential buildings: A case study. *Journal of Building Physics* 40(2) (2016) 125-143.
 22. Roache PJ. *Computational Fluid Dynamics*. Hermosa, Albuquerque, NM, 1982.
 23. Young D. Iterative methods for solving partial differential equations of elliptical type. *Transactions of the AMS - American Mathematical Society* 76 (1954) 92.A
 24. Abu-Mulaweh HI, Armaly BF, Chen TS. Laminar natural convection flow over a vertical forward-facing step. *Journal of Thermophysics and Heat Transfer* 10 (1996) 517-523.
 25. Asan H, Namli L. Laminar natural convection in a pitched roof of triangular cross-section: summer day boundary conditions. *Energy and Building* 33 (2000) 69-73.
 26. Asan H, Namli L. Numerical simulation of buoyant flow in a roof of triangular cross-section under winter day boundary conditions, *Energy and Building* 33 (2001) 753-757.
 27. Penot F. Numerical calculation of two-dimensional natural convection in isothermal open cavities. *Numerical Heat Transfer* 5 (1982) 421-437.
 28. LeQuere O, Humphery JAC, Sherman FS. Numerical calculation of thermally driven two-dimensional unsteady laminar flow in cavities of rectangular cross-section. *Numerical Heat Transfer* 4 (1981) 249-283.

The Array Analyzing of the High Quality Glacial Seismic Events Active in Greenland Using Long-Period Surface (Rayleigh) Wave Detection by the German Regional Seismic Network

Mustafa TOKER 

Yuzuncu Yil University, Department of Geophysical Engineering, Van, Turkey

ABSTRACT

This study reports on four high quality glacial events in Greenland, M 4.9, 2007-07-04; M 4.8, 2007-07-09; M 4.7, 2007-07-09; M 4.7, 2007-07-20 detected using the long-period surface waves (Rayleigh wave) recorded at the stations of the German Regional Seismic Network (GRSN) array (German-GR and Geofon-GE programs). The waveform patterns of the detected slow events for Greenland updated through 2008 were monitored to analyze this new class of low-frequency earthquakes in the context of the array processing technique and array parameters using the software Seismic Handler Motif (SHM). The array geometry of GRSN was defined by seven stations and processed to associate seismic phase arrivals to define glacial events. Two stations of GRSN were assigned the role of reference sites. The long-period surface wave characteristics of the event signals with magnitudes M 4.9, M 4.8, M 4.7, and M 4.7 were detected using filtering, beamforming, and location-relocation steps; then, the results were updated using SHM. The event data were filtered with a Butterworth band pass filter of 35s-70s with a common amplification. Using the array-beamforming technique, the beam traces were computed to calculate the beam-slowness (the apparent velocity) and the beam-azimuth of incoming wavefronts for particular time intervals to further analyze the observed glacial events. Then, the detected event signals were relocated and used to estimate array parameters; beam-slowness and beam-azimuth. Finally, in this study, the array processing technique was used with array parameters computed from the SHM to detect and analyze the slow glacial events using the array installation data from GRSN.

Keywords:

Greenland; Glacial Events; Surface Waves; Waveform Patterns; Beamforming

Article History:

Received: 2017/07/18

Accepted: 2017/12/26

Online: 2017/12/26

Correspondence to: Mustafa Toker,
Yuzuncu Yil University, Department of
Geophysical Engineering, Zeve Campus,
65080, Van, TURKEY
e-mail: tokermu@gmail.com

INTRODUCTION

The worldwide recorded long-period signals from events in Greenland display the high amplitude of the event signals at long ways [1]. These signals from glacial earthquakes observed in Greenland are different from those of tectonic events; thus, standard techniques of seismic monitoring are not used to detect or locate them [1]. The existence of glacial earthquakes was not known until 2003 [2-3]. These largest events in Greenland cause long-period ($T > 30$ s) signals and are similar in magnitude to those caused by tectonic earthquakes with a moment-magnitude of $M_w = 5$.

The Greenland events are not appeared in regular earthquake catalogs which are based on the radiation of the high frequency components [1, 3]. The glacial events are consistent with slow processes and depletion of high-frequencies [2]. The longer source duration periods of glacial events result in the depletion of radiated high frequencies [1]. Long time glacial events can radiate little high frequencies and can elude detection since event signals with low amplitudes-high frequencies are buried in noises. The well-known standard techniques of event detection and relocation depend on the high-frequency (1s) P-waves in seismogram data [1].

Glacial events were initially observed from the development of a new algorithm [1, 3]. The 252 glacial earthquakes in Greenland for the period 1993–2008 were detected and located using a surface-wave detection algorithm [1, 4] (The full list of events for 1993–2008, as well as recent updates, is available at <http://www.globalcmt.org>). This algorithm was designed to identify seismic sources in relation to their generation of long-period seismic waves [1-3, 5] and based on array-processing techniques. These long-period slow events cause surface waves that cannot be described by the moment-tensor for crustal events [1]. The vertical-component data recorded at the seismic stations are filtered (35s-150s) and the phases are correctly adjusted for the propagation delay of surface (Rayleigh) waves from reference location to each station in the German Regional Seismic Network

(GRSN) [2]. When the locations corresponding to an event are identified, all the detected signals are in phase. Then, the corrected surface wave arrivals for the observed events in Greenland are aligned and all the observed signals are in phase [1]. These surface waves were recognized to fit to a single source model [6].

The first application of the signal location algorithm to 3 years of data (1999–2001) from the Global Seismographic Network (GSN) led to the detection of 46 unreported events of $4.6 \leq M \leq 5.0$ in Greenland, Alaska, and Antarctica, with 42 of the events located in and along the eastern and western shores [1]. The source parameters for the fifty-nine events detected during 2006–2008 are listed in Table 1. For the Western Greenland region, 11 or more earthquakes were

Table 1. Source parameters for 59 glacial events in Greenland [1, 4] and high-quality (A/B) glacial events selected for this study contained in the red bold font.

<i>Date</i>	<i>Time</i>	<i>Latitude</i>	<i>Longitude</i>	<i>M</i>	<i>Date</i>	<i>Time</i>	<i>Latitude</i>	<i>Longitude</i>	<i>M</i>
2006/02/13	20:29:52	70.25	-30.75	4.8C	2007/08/03	19:25:12	72.25	-52.25	4.8C
2006/02/28	22:44:32	69.00	-33.00	4.8A	2007/08/13	20:37:52	66.25	-38.75	4.8B
2006/03/04	23:05:20	65.75	-41.25	4.7B	2007/08/25	09:19:04	75.25	-56.75	4.9A
2006/04/29	11:39:12	65.25	-41.25	4.8B	2007/09/11	22:42:00	70.25	-50.75	4.6C
2006/05/01	06:44:32	72.25	-52.75	4.9A	2007/10/13	05:55:12	74.75	-56.75	4.8A
2006/06/24	10:48:32	69.25	-49.75	4.7E	2007/11/21	18:04:56	66.25	-38.75	5.0A
2006/07/10	18:13:36	65.25	-40.75	4.8A	2007/11/24	00:08:56	68.50	-33.50	4.8A
2006/07/16	03:15:28	69.00	-31.00	4.6C	2007/11/24	12:54:32	66.50	-38.50	4.9A
2006/07/16	06:41:52	73.25	-53.25	4.7C	2007/11/24	13:29:52	67.25	-38.25	4.8A
2006/07/25	04:51:44	68.75	-49.75	4.7C	2007/12/14	06:39:36	75.25	-56.75	4.9A
2006/08/10	18:45:20	77.50	-65.50	4.8B	2007/12/31	14:40:56	66.25	-38.75	4.9A
2006/08/23	17:19:28	65.75	-37.75	4.7C	2008/02/14	05:12:24	72.75	-55.75	4.8B
2006/08/28	07:55:04	69.50	-25.50	4.6B	2008/04/05	21:06:08	75.50	-56.50	4.8A
2006/09/10	04:20:16	77.75	-57.25	4.9C	2008/04/07	13:58:00	74.25	-56.75	4.7C
2006/10/09	04:03:12	76.50	-60.50	4.8B	2008/05/04	12:52:40	65.50	-41.50	4.8B
2006/10/14	07:23:20	76.00	-58.00	4.8B	2008/05/28	21:06:40	70.75	-49.25	4.7B
2006/11/05	09:13:04	75.75	-58.25	4.7C	2008/06/12	17:20:08	69.00	-49.00	4.7E
2006/11/28	10:55:44	68.75	-32.75	4.9B	2008/06/13	15:40:40	75.75	-57.75	4.8C
2006/12/19	16:57:44	74.75	-57.75	4.8B	2008/06/19	15:20:00	74.75	-58.25	4.8B
2007/04/22	08:55:04	66.25	-38.25	4.7A	2008/07/13	04:59:44	69.50	-49.50	4.8C
2007/04/23	21:56:56	75.25	-58.25	4.8A	2008/08/01	14:43:20	66.50	-38.50	4.8A
2007/05/30	02:57:12	77.50	-63.50	4.7C	2008/08/01	23:00:40	66.75	-39.25	4.8A
2007/06/09	05:16:56	75.75	-60.75	4.8B	2008/08/14	20:58:24	77.75	-58.75	5.0A
2007/07/04	16:55:20	69.25	-49.75	4.9A	2008/08/19	21:05:28	66.25	-38.25	4.8B
2007/07/09	01:08:16	66.25	-37.25	4.8A	2008/11/03	16:44:48	68.75	-33.75	4.9B
2007/07/09	02:42:08	66.75	-38.25	4.7B	2008/11/07	13:44:24	77.50	-66.50	4.7E
2007/07/09	05:31:12	75.00	-57.00	4.6C	2008/11/21	20:31:52	76.00	-58.00	4.9A
2007/07/20	00:36:16	69.25	-33.25	4.7A	2008/11/25	04:10:40	68.50	-33.50	4.9A
2007/07/24	23:03:12	77.25	-60.75	4.9A	2008/12/13	14:47:52	68.00	-34.00	5.0A
2007/07/26	22:42:48	66.50	-38.50	4.7A					

detected in every five years from 1993 to 2003 (an average of 4.5 events per year during the same period). These long-period ($T > 30$ s) events with magnitudes of $M \sim 5$ require the use of long-period surface waves to explain this new category of seismicity model. In this study, the glacial event-detections for Greenland updated through 2008 and the understanding of the high quality events that resulted from some investigations of rapidly moving outlet glaciers in Greenland were reviewed [1]. The four high quality events in Greenland with their source mechanisms through 2008 (Table 1) were selected to analyze these slow events in the context of the array processing technique and array parameters using the software Seismic Handler Motif (SHM) [7]. The surface wave characteristics of these four glacial events with the magnitudes of $M = 4.9$, 2007-07-04; $M = 4.8$, 2007-07-09; $M = 4.7$, 2007-07-09; and $M = 4.7$, 2007-07-20 (Table 1) were also provided to update the detection results. The main purpose of the array processing technique for the observations available for this study was to calculate the beam-slowness (the apparent velocity) and beam-azimuth for particular time intervals to analyze the observed glacial events. The style of processing used is similar to that undertaken in some styles of signal-processing analysis and time-series applications [1]. Finally, we present the array parameters of the four selected events regarding the nature of the glacial earthquakes with the German Regional Seismic Network (GRSN; GERMAN-GR and GEOFON-GE).

MATERIAL AND METHODS

Throughout our study, we processed data obtained from GRSN consisting of the large regional GERMAN (GR) and GEOFON (GE) arrays (<http://geofon.gfz-potsdam.de/waveform/archive/index.php>). Fig. 1a shows the configuration of the GRSN array and the layout of the seismometer sites for the regional arrays. GRSN (Fig. 1a) [8] comprises 16 STS2 digital broadband stations with a flat, velocity-proportional response characteristic in the frequency range of 8.33 mHz to 40 Hz [9]. GRSN is designed to monitor and collect high-quality data from regional and global seismic events as well as recording and locating all events with $M_l > 2$ in German territory. All stations are continuously recorded and, with one exception, are connected via the Internet with each other and with the network center at the Gräfenberg Observatory (GRFO) in Erlangen [9] (Fig. 1a). GRSN is a combination of a physical and a virtual network (for more details, see <http://www.szgrf.bgr.de/>).

In this study, the GRSN array was defined by a set of stations; RUE, GTTG, CLZ, RGN, IBBN, BSEG, and HLG with two stations, CLZ and GTTG, being assigned the role of reference sites (Fig. 1a). The relative distances from these reference points to all other array sites are used later in all

array specific analysis algorithms. The four glacial events (Table 1) were observed in seven stations; RUE, GTTG, CLZ, RGN, IBBN, BSEG, and HLG (Fig. 1b). The recorded events from Germany were processed with SHM improved by K. Stammler [7], which is used for waveform retrieval and data analysis [9] (available via <http://www.szgrf.bgr.de/sh-doc/index.html>). Seismic arrays generally differ from local seismic networks mainly by the methods used for signal analysis being superior to three-component stations in terms of improving the quality of seismic stations and detecting and characterizing signals from earthquakes [10]. Array processing techniques require high signal coherency across the array, and this places important constraints on the array geometry, spatial extent, and data quality. The appropriate analysis of the array data is dependent on a stable, high-precision relative timing of all the array elements. Small temporal differences in the arrival of seismic signals between the different sensors play an important role in all array-processing techniques [10]. Hence, the signal detection capabilities of arrays are obtained by applying the beamforming technique,

which suppresses noise while preserving the signal, thus enhancing the signal-to-noise ratio (SNR). In addition, array parameters, the station-to-event azimuth (backazimuth)

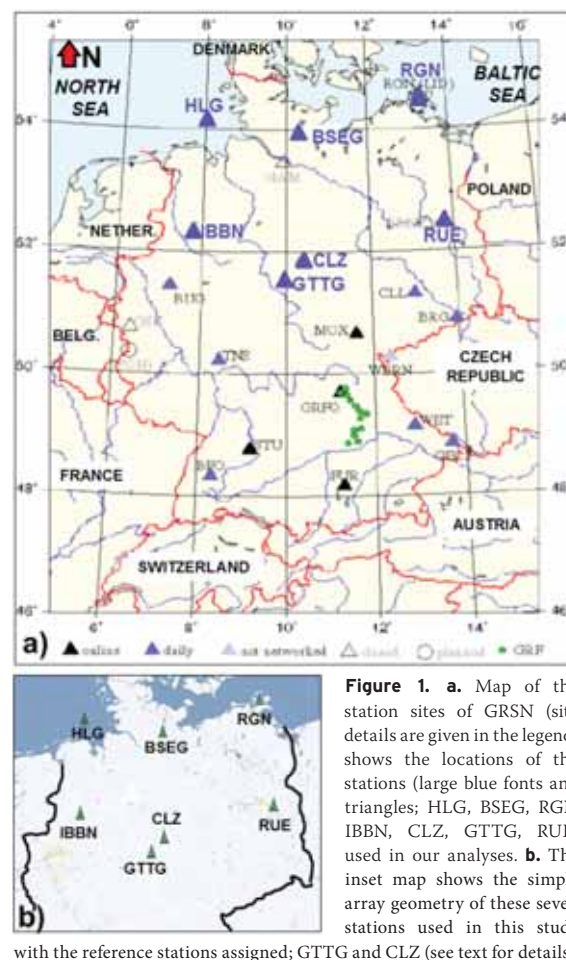


Figure 1. a. Map of the station sites of GRSN (site details are given in the legend) shows the locations of the stations (large blue fonts and triangles; HLG, BSEG, RGN, IBBN, CLZ, GTTG, RUE) used in our analyses. b. The inset map shows the simple array geometry of these seven stations with the reference stations assigned; GTTG and CLZ (see text for details).

and the apparent velocity (slowness) of various styles of event signals, are also estimated from arrays. These parameters are essential for both event relocation and the classification of signals [10].

In this study, the general seismic array processing beamforming technique was applied using SHM to analyze the event signals. SHM used in this study is an interactive analysis program preferably used with continuous waveform data [7]. It was developed at the Seismological Observatory Gräfenberg and in this study was used in the routine analysis of the four detected glacial events [9] (Table 1 and Fig. 1). SHM is well suited to the analysis of glacial seismic data since it has advanced features for trace manipulations and automatic or semiautomatic phase picks [7]. The basic tools and features of SHM are built around reading traces of the detected events from continuous data streams in Stein-compressed MiniSEED files associated with a set of standard filters (simulation filters and Butterworth filters) on broadband input traces of the events (see also [7]). Teleseismic beam traces using array-beamforming are computed using SHM. The slowness and back-azimuth of an incoming wavefront for array processing are also determined. The detected events are located using the LOCSAT program. Moreover, in this paper, the applied procedures for estimating the slowness parameter, the angles of approach (azimuth-backazimuth) of detected event signals and processing algorithms for event detection are briefly described. This study also documents array-processing technique

with concluding remarks from the SHM for detecting and associates event signals from regional seismic events using the array installation data from the regional GERMAN (GR) and GEOFON (GE).

The automatic processing steps in SHM are divided into three separate cases: a) Event array processing to associate phase arrivals to define events, b) event signal detection using beamforming, filtering, and location-relocation, and c) signal attribute to estimate the array parameters; slowness, azimuth and/or back-azimuth.

RESULTS AND DISCUSSION

The source parameters of the four glacial events in Greenland are given in Table 1 and were recorded in GRSN stations; HLG, BSEG, IBBN, RGN, CLZ, GTTG, and RUE (Fig. 1b). The recorded glacial events from the GRSN network were processed and seismic array beamforming and alignment of the events were performed by SHM. The waveform resemblances (vertical component) of the recorded four events from the seven stations are shown in Figs. 2-5.

The waveforms presented in Figs. 2-5 show the surface wave peaks of the detected glacial events observed at the GRSN network and the aligned traces of all single observations. All the signal traces were adjusted and relocated to

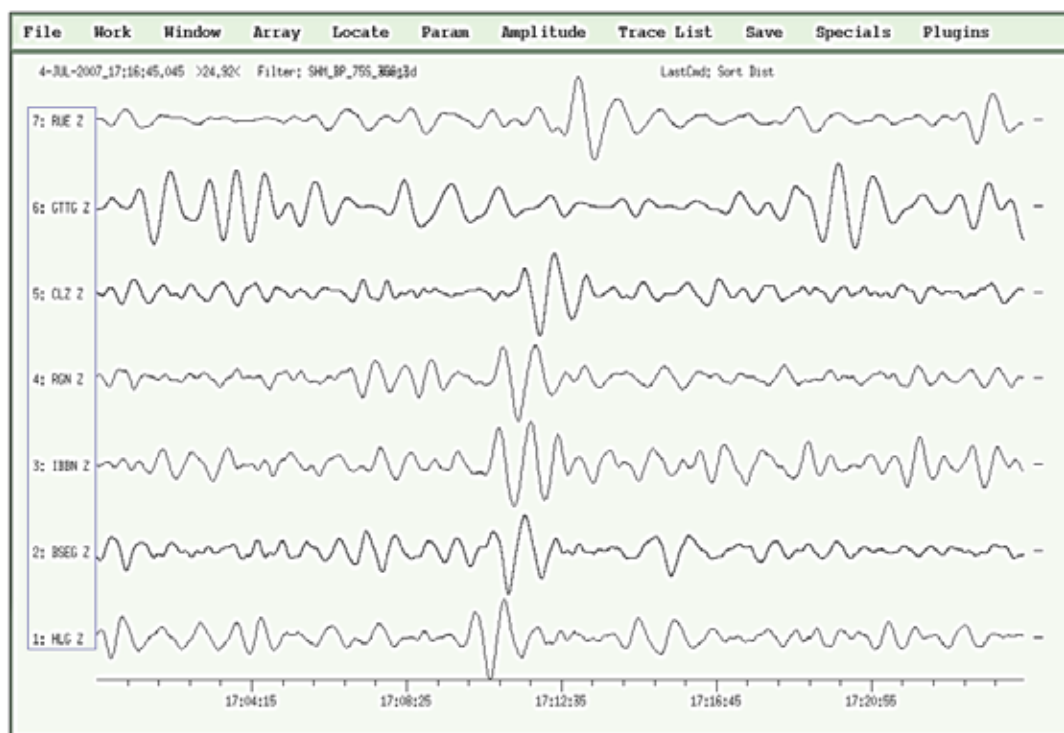


Figure 2. Mean root square residual: 0.51, distance: 32.5, beam-slowness: 29.0 ± 0.4 (x), beam-azimuth: 322.4 ± 0.5 (x), reference: CLZ, origin time: 4-JUL-2007_16:55:20.000, epicenter: 69.25 lat. -49.75 lon. and FE region: Western Greenland (Kalaallit Nunaat).

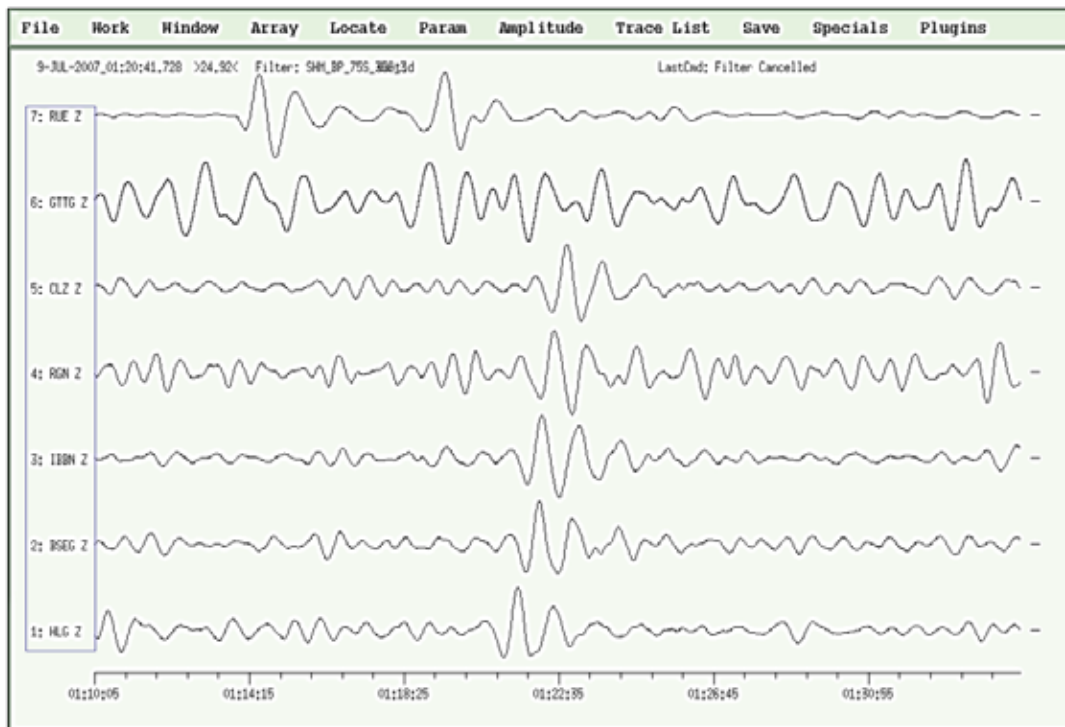


Figure 3. Mean root square residual: 0.70, distance: 27.6, beam-slowness: 28.9 ± 0.7 (x), beam-azimuth: 314.5 ± 1.2 (x), reference: GTTG, origin time: 9-JUL-2007_01:08:16.000, epicenter: 66.25 lat. -37.25 lon. and FE region: Eastern Greenland (Kalaallit Nunaat).

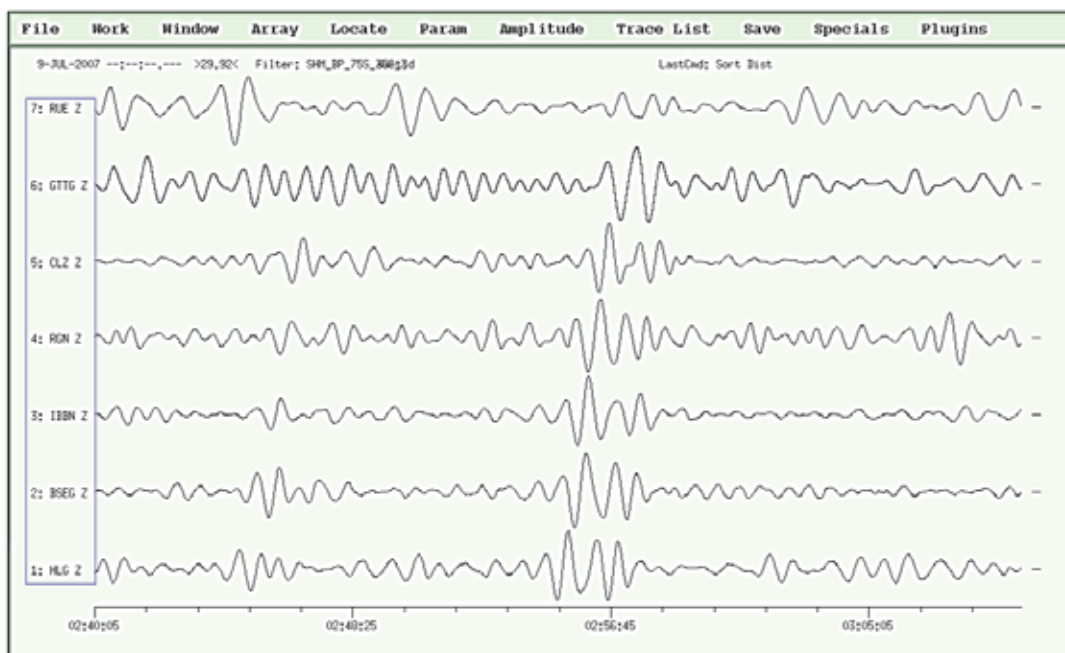


Figure 4. Mean root square residual: 0.83, distance: 28.1, beam-slowness: 29.6 ± 0.9 (x), beam-azimuth: 312.4 ± 1.4 (x), reference: CLZ, origin time: 9-JUL-2007_02:42:08.000, epicenter: 66.75 lat. -38.25 lon. and FE region: Eastern Greenland (Kalaallit Nunaat).

provide the alignment of the event pulses. The SNR of an observed signal calculated by summing the coherent event signals from the array sites was improved with an array. All the seismic data were filtered with Butterworth band-pass filter between 35s and 70s and are displayed with a com-

mon amplification. All the signal traces were aligned and summed without any delay-time application. The important process during the beamforming was to identify the delay times, with which the single signal traces were shifted before summation ('delay and sum') to obtain the highest ampli-

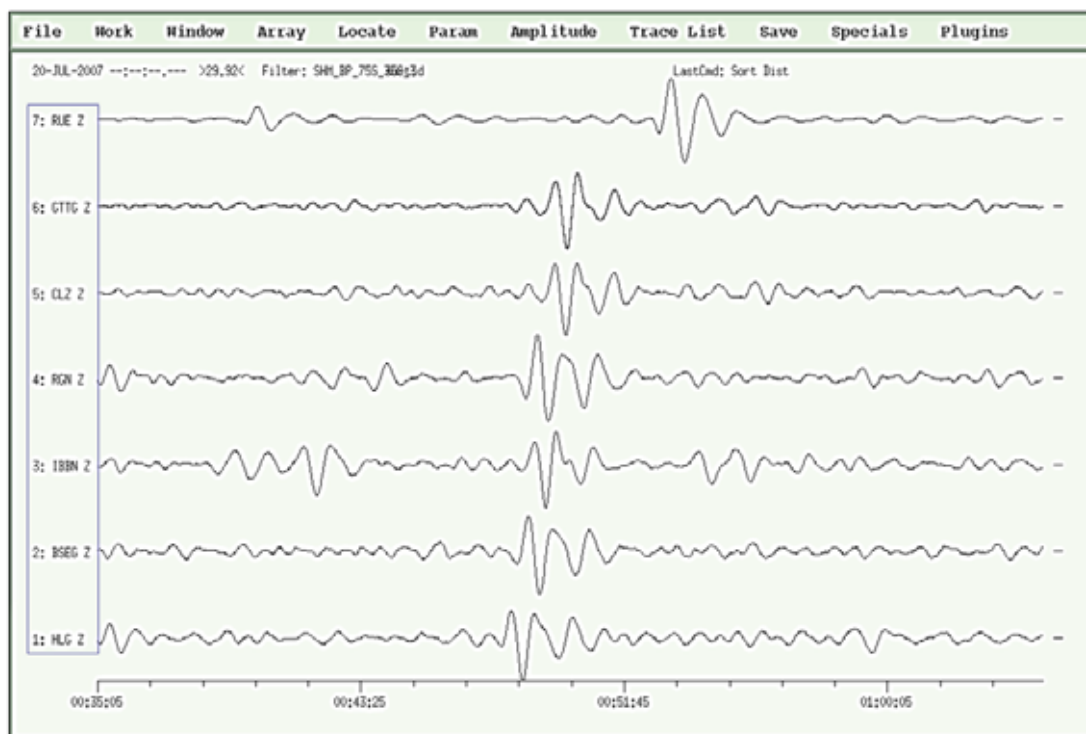


Figure 5. Mean root square residual: 1.38, distance: 26.8, beam-slowness: 30.0 ± 0.8 (x), beam-azimuth: 323.3 ± 1.2 (x), reference: CLZ, origin time: 20-JUL-2007_00:36:16.000, epicenter: 69.25 lat. -33.25 lon. and FE region: Eastern Greenland (Kalaallit Nunaat).

tude due to the coherent interference of the observed event signals. The onset times of the event signal on each trace were simply picked and the traces were shifted with respect to the onset time at the reference site of the array.

Computing event signals

The seismic data from the GRSN network are installed and read in the appropriate data window of SHM for monitoring and analyzing the event signals. The Butterworth bandpass filter is chosen to provide a good SNR. The slowness and azimuth of incoming waves are determined using visible minimum / maximum peaks of automatically picked up signals; then, the Plane Wave option of SHM is called. The resulting slowness and azimuth were checked using the Beam option of SHM to correct some of the essential phase readings and then, Location is called and the event is located. The following subsections present the stages of how the installed seismic data is read, monitored and analyzed using SHM software.

Reading the MiniSEED data format

The MiniSEED data format used in this study is a subformat of the commonly used SEED data format. It is suited to continuous data or for storing long time spans of data [7]. SHM accesses the MiniSEED format by start time and read length and reads only part of the file rather than reading a filename completely. SEED and MiniSEED data

formats are quiet flexible and allow a large variety of subformat types. For reading the MiniSEED data with the read option, the dialog box of SHM should be correctly configured.

MiniSEED files are prepared as the GRSN stations are inserted (Fig. 1a). When all the stations have been configured, the menu entry Read is selected. This opens a dialog box. The appropriate buttons for stations, data channel (e.g., BH, LH, and HH) and component(s) (east-west, north-south, and z-vertical component) are selected. Date and time are chosen using the arrow buttons above and below the time field. The data are entered by specifying the station list, channel code, start time, read length, and components as shown in Figs. 2-5. In order to find the data file(s) to be read, SHM needs to have a directory file which contains the information about the location, filename and content of MiniSEED files called *sdf*file.sfd (*sfd* refers to seed file directory) and resides in the data directory. SHM reads data that are given in such a file. Before processing the data in the MiniSEED format, *sdf*file requires to be updated. The SHM package also contains a program to create *sdf*file.sfd. After *sdf*file.sfd has been generated, SHM reads the data files given. The SHM command for reading the MiniSEED data needs to have the location of the *sdf*file.sfd.

Reading and filtering data

The requested data streams and time window are selec-

Table 2. Summary of the array parameters of the detected events (see Table 1 for the source mechanisms of the selected events and Fig. 1 for reference stations).

Glacial events	RMS	Dist.	beam-slowness	beam-azimuth	epi-slowness epi-azimuth	Depth	Ref.	Origin Time	Epi.	FE region
Event 1	0.70	27.6	28.9±0.7(x)	314.5±1.2 (x)	not specified	0.0	GTTG	9-JUL-2007_01:08:16.000	66.25 Lat. -37.25 Lon.	Eastern Kalaallit Nunaat
Event 2	0.83	28.1	29.6±0.9(x)	312.4±1.4 (x)	not specified	0.0	CLZ	9-JUL-2007_02:42:08.000	66.75 Lat. -38.25 Lon.	Eastern Kalaallit Nunaat
Event 3	1.38	26.8	30.0±0.8(x)	323.3±1.2 (x)	not specified	0.0	CLZ	20-JUL-2007_00:36:16.000	69.25 Lat. -33.25 Lon.	Eastern Kalaallit Nunaat
Event 4	0.51	32.5	29.0±0.4(x)	322.4±0.5 (x)	not specified	0.0	CLZ	4-JUL-2007_16:55:20.000	69.25 Lat. -49.75 Lon.	Western Kalaallit Nunaat

ted by opening a dialog box of the menu entry Read (the interface to the MiniSEED formatted data). The essential parameters; station list, channel, component, start time, length of time window and location of the directory file (sfdfile.sfd.) are chosen. Then, the Filter menu entry is selected and the desired Bandpass filter (35s-70s) is chosen in broadband waveform data. The filter is applied to the traces on the display and the read-in traces are filtered automatically. Then, the filtering is carried out on all the traces of the display if no trace has been previously selected. The resulting traces are displayed on the screen.

Plane wave

The epicentral distances of the recorded glacial events are larger than the aperture of the recording array of GRSN (Fig. 1). The major frequencies of the picked signals are in a range in which signal coherency is possible, indicating waveform similarity on the recording array (Figs. 2-5). Hence, the plane wave algorithm of SHM is applicable. Considering that the wavefront of the phase is a plane wave, the menu entry Plane Wave of SHM computes the array parameters, the slowness and back-azimuth from coherent phases and uses all the phases of the name provided in the phase dialog box (Figs. 2-5). This algorithm detects the best fitting of the wave plane and parameterizes it by back-azimuth and slowness. The concluding values are given in the analysis parameter box and checked with the command Beam. The entry Beam needs to have the location entries (Lat. and Lon.) of the recording stations in the station information file.

Locating and sorting distances

After the locations (Lat. and Lon.) of the events have been manually written in the analysis parameter box and the appropriate settings of the reference stations have been checked, the epicentral distances to the chosen reference stations and the corresponding slowness are computed using the correction for ellipticity of the earth and the results entered into the analysis parameter box are shown. As a result, the epicenter locations are determined and all the traces are sorted according to the epicentral distance.

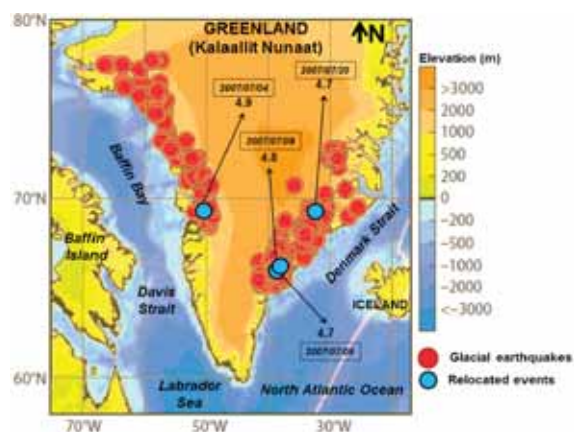


Figure 6. Glacial seismicity map showing 252 glacial earthquakes in Greenland for the period 1993–2008, detected and located using the surface-wave detection algorithm (data from [1]) and analyzed in detail by [4] (map modified and adapted from [1]) and also the locations of the four glacial events (magnitude and time) selected and analyzed in this study (see Tables 1 and 2 for related parameters). The tight clustering of the relocated epicenters is obvious near major outlet glaciers [1].

Array parameters

The GRSN array geometry (Fig. 1b) is defined by seismometers with two seismometers being assigned the roles of the two reference sites (CLZ, GTTG) during the data processing. The relative distances from the reference points to all other array sites are used in all array specific analysis algorithms.

A seismic wave approaches a given array with a plane wave front for much larger distances from the source (more than 10 wavelengths) [7, 10]. The propagation directions of the plane wave front projected onto the horizontal plane are basically identified by the two main angles; ϕ and θ [10]. ϕ is the backazimuth, also called beam-azimuth, which is an angle-of-wavefront approach, measured clockwise between the north and the direction towards the epicenter in $^{\circ}$. θ refers to the direction in which the wavefront propagates is also measured in $^{\circ}$ from the north with $\theta = \phi \pm 180^{\circ}$. The angle observed between the direction of approach and the vertical plane is called the angle of incidence i with $i \leq 90^{\circ}$. The seismic velocity below the array site and the angle of

incidence define the apparent propagation speed of the wavefront crossing the array site.

The crustal velocity with the incidence angle determines the propagation speed of the wavefront at the instruments and is called an apparent velocity v_{app} (not the physical propagation speed). v_{app} is absolute value of the apparent velocity vector in [km/s] of a plane wave crossing an array and a constant for a specific seismic ray traveling through a layered Earth model. Apparent velocity vector v_{app} is given by $v_{app} = 1 / s \cdot v_{app} = (v_{app,x}, v_{app,y}, v_{app,z})$, where $(v_{app,x}, v_{app,y}, v_{app,z})$ are the apparent velocity components in [km/s] of the wavefront crossing an array site. The inverse of the apparent velocity is called slowness s (a constant for a specific ray), which we call beam-slowness here. The slowness unit is [s/km] for local or regional studies and [s/°] for global applications (the slowness is also known as the ray parameter). s slowness vector is given by $s = 1 / v_{app} \cdot s = (s_x, s_y, s_z)$, where (s_x, s_y, s_z) are the inverse apparent velocity (= slowness) components in [s/km].

The computed array parameters of the events are given in Table 2 and their locations are shown in Fig. 6.

Beamforming

The event signals in the glacial data collected from the GRSN network are detected during the data processing by SHM in this study. The signals of plane waves recorded at different sites of the GRSN array are more coherent than random noise. These signals are found to be very distinct from the background noise due to their amplitudes, magnitudes, different shapes, and/or frequency contents (Figs. 2-5 and Table 2). The delay times for each detected event at each station are automatically defined to calculate an array beam as shown in Figs. 2-5 by a specific beam-azimuth and beam-slowness combination. The calculated delay times and array beams depend on the position of the single sites with respect to the reference points (CLZ and GTTG) of the GRSN array (Fig. 1b) and to the backazimuth of the signal. The noises and amplitude differences in the signals influence the beam quality and hence, the improvement of the SNR due to the beamforming is essential. The event signals shown in Figs. 2-5 indicate forming signals with beam-slowness and comparing the amplitudes of the beams and reveal the best slowness-backazimuth combination that provides the maximum energy on the beam. The filtering-beamforming and beamforming-filtering processes are performed to test the traces and beams. Theoretically, both procedures give the same result and the superposition theorem of algebra for both beamforming and filtering is true [10].

CONCLUSION

In this study, we detected four long-period glacial events; M 4.9, 2007-07-04; M 4.8, 2007-07-09; M 4.7, 2007-07-09; and M 4.7, 2007-07-20 recorded at the stations of the GRSN array (GR and GE) and monitored the waveform patterns of these events for Greenland updated through 2008. The array geometry (GRSN) was defined by a set of seven stations; RUE, GTTG, CLZ, RGN, IBBN, BSEG, and HLG. The stations, CLZ and GTTG, were assigned the role of reference sites. We used the long-period surface waves (Rayleigh) to detect and analyze this new class of earthquake model in the context of array processing technique and array parameters using SHM.

The GRSN array geometry was processed to associate phase arrivals to identify glacial events. The surface wave characteristics of the detected events with magnitudes; M 4.9; M 4.8; M 4.7; and M 4.7, were provided to update the detection results. The glacial event signals were detected for use in the beamforming, filtering, and location-relocation steps. All the seismic data were filtered with Butterworth band-pass filter between 35s and 70s and were displayed with a common amplification. The beam traces using array-beamforming were computed using SHM. The beam-slowness (the apparent velocity) and beam-azimuth of the incoming wavefronts for particular time intervals were calculated to analyze the observed glacial events. Then, the detected event signals were relocated and attributed to estimate the array parameters; slowness, azimuth, and back-azimuth.

Finally, this paper summarized the processing steps of the array processing technique used with array parameters computed from the SHM for detecting the events and associated seismic signals of the detected events from regional seismic events using array installation data from the GRSN array. Considering the detected glacial events in this study, the array parameters using the array processing technique can be used to constrain the glacio-mechanical processes active in Greenland. Additional event observations from different regional array geometries for various earth-science purposes (e.g., in Turkey [11-13]) are needed to improve the understanding of glacial and/or non-glacial earthquakes.

ACKNOWLEDGMENTS

This work was supported by Yuzuncu Yil University, Department of Geophysical Engineering (Van, Turkey) and the University of Oulu, Sodankylä Geophysical Observatory (SGO), Laboratory of Applied Seismology (Oulu, Finland) with a post-doctoral research grant and training agreement contract issued to Yuzuncu Yil and Oulu Universities. The author offers his greatest appreciation to

the post-doctoral supervisor, Prof. Dr. Elena Kozlovskaya and the Director of SGO, Prof. Dr. Esa Turunen.

References

1. Nettles M, Ekström G. Glacial earthquakes in Greenland and Antarctica. *Annual Review of Earth and Planetary Sciences* 38 (2010) 467-491. doi:10.1146/annurev-earth-040809-152414.
2. Ekström G, Nettles M, Abers GA. Glacial earthquakes. *Science* 302 (2003) 622–624.
3. Ekström G, Nettles M, Tsai, VC. Seasonality and increasing frequency of Greenland glacial earthquakes. *Science* 311 (2006) 1756–1758.
4. Tsai VC, Ekström G. Analysis of glacial earthquakes. *Journal of Geophysical Research* 112 (2007) F03S22.
5. Ekström G. Global detection and location of seismic sources by using surface waves. *Bulletin of the Seismological Society of America* 96 (2006) 1201–1212.
6. Kawakatsu H. Centroid single force inversion of seismic waves generated by landslides. *Journal of Geophysical Research* 94 (1989) 12363–12374.
7. Stammer K. SeismicHandler - Programmable multichannel data handler for interactive and automatic processing of seismological analysis. *Computers & Geosciences* 19 (1992) 135–140.
8. Korn M. (Ed.). Ten years of German Regional Seismic Network (GRSN): Report 25 of the Senate Commission for Geosciences. Deutsche Forschungsgemeinschaft, Wiley-VCH Verlag, Weinheim, 2002.
9. Trnkoczy A, Havskov J, Ottemöller L. Seismic networks, in: Bormann P. (Ed.). *New Manual of Seismological Observatory Practice (NMSOP)*. Deutsches GeoForschungsZentrum, Potsdam, pp. 1-60, 2009.
10. Schweitzer J, Fyen J, Mykkeltveit S, Kvaerna T. Seismic arrays, in: Bormann P. (Ed.). *New Manual of Seismological Observatory Practice (NMSOP)*. Deutsches GeoForschungsZentrum, Potsdam, pp. 1-52, 2009. doi:10.2312/GFZ.NMSOP_r1_ch9.
11. Tur, H, Hoskan, N., Aktaş, G., 2015. Tectonic evolution of the northeastern shelf of the Marmara Sea (Turkey): interpretation of seismic and bathymetric data. *Mar. Geophys. Res.* v. 36: 1-34. Doi: 10.1007/s11001-014-9230-z.
12. Gökaşan, E., Tur, H., Ecevitoglu, B., Görüm, T., Türker, A., Tok, B., Çağlak, F., Birkan, H., Şimşek, M., 2005. Evidence and implications of massive erosion along the Strait of İstanbul (Bosphorus). *Geo-Mar Lett.* v. 25: 324-342. Doi: 10.1007/s00367-005-0216-3.
13. Gökaşan, E., Algan, O., Tur, H., Meriç, E., Türker, A., Şimşek, M., 2005. Delta formation at the southern entrance of İstanbul Strait (Marmara Sea, Turkey): a new interpretation based on high-resolution seismic stratigraphy. *Geo-Mar Lett.* v. 25: 370-377. Doi: 10.1007/s00367-005-0215-4.

